SANDIA REPORT
SAND2022-13918
Printed October 2022

Sandia National Laboratories

Project Final Report: Computational Imaging for Intelligence in Highly Scattering Aerosols

Brian Z. Bentz, Jeremy B. Wright, John D. van der Laan, Andres L. Sanchez, Christian A. Pattyn, John P. Zenker, Brian J. Redman, Elihu Deneke, Andrew Glen, Karl Westlake, Ryan L. Hastings, Christopher M. Lacny, David W. Alexander, and Kevin J. Webb

Prepared by
Sandia National Laboratories
Albuquerque, New Mexico 87185
Livermore, California 94550

Issued by Sandia National Laboratories, operated for the United States Department of Energy by National Technology & Engineering Solutions of Sandia, LLC.

Available to DOE and DOE contractors from

U.S. Department of Energy
Office of Scientific and Technical Information
P.O. Box 62
Oak Ridge, TN 37831

Telephone: (865) 576-8401
Facsimile: (865) 576-5728
E-Mail: reports@osti.gov
Online ordering: http://www.osti.gov/scitech

Available to the public from

U.S. Department of Commerce
National Technical Information Service
5301 Shawnee Road
Alexandria, VA 22312

Telephone: (800) 553-6847
Facsimile: (703) 605-6900
E-Mail: orders@ntis.gov
Online order: https://classic.ntis.gov/help/order-methods

Project Final Report: Computational Imaging for Intelligence in Highly Scattering Aerosols

Brian Z. Bentz*, Jeremy B. Wright, John D. van der Laan,
Andres L. Sanchez, Christian A. Pattyn, John P. Zenker,
Brian J. Redman, Elihu Deneke, Andrew Glen, and Karl Westlake

Applied Optical and Plasma Science, Weaponization and Signature Research and Development, Proliferation Detection Remote Sensing, Weapons of Mass Destruction Threats and Aerosol Science, Counter-Autonomy and Physical Security Systems Research and Development, Real-time Computing Research
Sandia National Laboratories
P.O. Box 5800
Albuquerque, NM 87185-9999

Ryan L. Hastings, Christopher M. Lacny, David W. Alexander, and Kevin J. Webb

Electrical and Computer Engineering
Purdue University
465 Northwestern Ave
West Lafayette, IN 47907

*Corresponding author: bzbentz@sandia.gov, fog@sandia.gov

SAND2022-13918

ABSTRACT

Natural and man-made degraded visual environments pose major threats to national security. The random scattering and absorption of light by tiny particles suspended in the air reduces situational awareness and causes unacceptable down-time for critical systems and operations. To improve the situation, we have developed several approaches to interpret the information contained within scattered light to enhance sensing and imaging in scattering media. These approaches were tested at the Sandia National Laboratory Fog Chamber facility and with tabletop fog chambers.

- Computationally efficient light transport models were developed and leveraged for computational sensing. The models are based on a weak angular dependence approximation to the Boltzmann or radiative transfer equation that appears to be applicable in both the moderate and highly scattering regimes. After the new model was experimentally validated, statistical approaches for detection, localization, and imaging of objects hidden in fog were developed and demonstrated. A binary hypothesis test and the Neyman-Pearson lemma provided the highest theoretically possible probability of detection for a specified false alarm rate and signal-to-noise ratio. Maximum likelihood estimation allowed estimation of the fog optical properties as well as the position, size, and reflection coefficient of an object in fog. A computational dehazing approach was implemented to reduce the effects of scatter on images, making object features more readily discernible.
- We have developed, characterized, and deployed a new Tabletop Fog Chamber capable of repeatably generating multiple unique fog-analogues for optical testing in degraded visual environments. We characterized this chamber using both optical and microphysical techniques. In doing so we have explored the ability of droplet nucleation theory to describe the aerosols generated within the chamber, as well as Mie scattering theory to describe the attenuation of light by said aerosols, and correlated the aerosol microphysics to optical properties such as transmission and meteorological optical range (MOR). This chamber has proved highly valuable and has supported multiple efforts inclusive to and exclusive of this LDRD project to test optics in degraded visual environments.
- Circularly polarized light has been found to maintain its polarization state better than linearly polarized light when propagating through fog. This was demonstrated experimentally in both the visible and short-wave infrared (SWIR) by imaging targets made of different commercially available retroreflective films. It was found that active circularly polarized imaging can increase contrast and range compared to linearly polarized imaging.
- We have completed an initial investigation of the capability for machine learning methods to reduce the effects of light scattering when imaging through fog. Previously acquired experimental long-wave images were used to train an autoencoder denoising architecture. Overfitting was found to be a problem because of lack of variability in the object type in this data set. The lessons learned were used to collect a well labeled dataset with much more variability using the Tabletop Fog Chamber that will be available for future studies.
- We have developed several new sensing methods using speckle intensity correlations. First, the ability to image moving objects in fog was shown, establishing that our unique speckle imaging method can be implemented in dynamic scattering media. Second, the speckle decorrelation over time was found to be sensitive to fog composition, implying extensions

to fog characterization. Third, the ability to distinguish macroscopically identical objects on a far-subwavelength scale was demonstrated, suggesting numerous applications ranging from nanoscale defect detection to security. Fourth, we have shown the capability to simultaneously image and localize hidden objects, allowing the speckle imaging method to be effective without prior object positional information. Finally, an interferometric effect was presented that illustrates a new approach for analyzing speckle intensity correlations that may lead to more effective ways to localize and image moving objects. All of these results represent significant developments that challenge the limits of the application of speckle imaging and open important application spaces.

- A theory was developed and simulations were performed to assess the potential transverse resolution benefit of relative motion in structured illumination for radar systems. Results for a simplified radar system model indicate that significant resolution benefits are possible using data from scanning a structured beam over the target, with the use of appropriate signal processing.

Acknowledgment

This research was supported by the Laboratory Directed Research and Development (LDRD) Program at Sandia National Laboratories. Sandia National Laboratories is a multimission laboratory managed and operated by National Technology & Engineering Solutions of Sandia, LLC, a wholly owned subsidiary of Honeywell International Inc., for the U.S. Department of Energy's National Nuclear Security Administration under contract DE-NA0003525. This document describes objective technical results and analysis. Any subjective views or opinions that might be expressed in the paper do not necessarily represent the views of the U.S. Department of Energy or the United States Government. We thank Laura J. Lemieux, Steven M. Storch, and Matthew Tezak at Sandia National Laboratories for their assistance operating the SNLFC facility and helping with the initial construction of the Tabletop Fog Chamber. We thank Philip L. Dreike at Sandia National Laboratories for the useful discussions. We thank Lilian K. Casias, Joshua C. Shank, Richard K. Harrison, and Garrett J. Marshall at Sandia National Laboratories for the useful discussions and interesting collaborations. Finally, we thank Jonathan R. Salton at Sandia National Laboratories for acting as project manager.

CONTENTS

LIST OF FIGURES

LIST OF TABLES

1. BACKGROUND

Degraded visual environments (DVEs) pose a major challenge to security in both uncontrolled and contested spaces. The aim of this project was to develop novel computational imaging and sensing methods that utilize scattered light to extract information from DVEs and reduce downtime of critical surveillance systems. A constraint of the development approach was that the methods should utilize conventional and low-cost light sources and detectors, potentially allowing rapid and low-cost integration into existing infrastructure through software modification. The methods that were developed show potential to reduce the uncertainty that limits decision making during high risk situations that threaten our national security. However, more work is required to develop a field-able system.

This is the final report of an LDRD project active from FY20-FY22. Several team members were involved in previous related projects. In the SAIL LDRD project “Utilizing Highly Scattered Light for Intelligence through Aerosols”, active in FY19, an initial investigation of light transport in fog was completed that suggested improvements to sensing and imaging were possible using computational methods [1]. In the LDRD project “Polarimetry for extended persistence and range in fog for infrastructure protection”, active from FY15-FY17, it was demonstrated that polarization can provide increased imaging performance in foggy conditions compared to traditional intensity based techniques [2]. Taken together, these projects represent a significant investment by Sandia into the development of methods for imaging through and characterizing scattering media like aerosols. We believe the results of this body of work support that there is great potential for improving situational awareness in DVEs.

2. APPROXIMATE MODEL FOR LIGHT TRANSPORT FOR COMPUTATIONAL DETECTION, LOCALIZATION, AND IMAGING OF OBJECTS HIDDEN IN SCATTERING MEDIA

2.1. Introduction

Random scattering and absorption of light by tiny particles in aerosols reduce situational awareness. Aerosols that are naturally occurring or man-made can create degraded optical environments (DOEs) that are sufficiently severe to impact security, remote sensing, transportation, aviation, astronomy, and more. For example, fog is particularly concerning because it can occur in most regions and at certain locations with high frequency. Information is scrambled by the random scattering and absorption of light by tiny particles suspended in the air, leading to reductions in signal and image contrast [3, 4].

Methods have been developed to reduce the effects of scatter on imaging [4]. The methods often discriminate between ballistic light that has traveled in a straight line from an object to a detector or lens system and scattered light that has changed propagation direction many times on the way to the detector [5, 6]. The ballistic light can be used to form a high resolution image if the scattered light is rejected using, for example, polarizing filters [7, 8] or temporal or coherence gating methods [9, 5, 10]. However, imaging is possible only in the moderately scattering regime because the ballistic light is exponentially attenuated with distance according to the Beer-Lambert-Bouguer law [11, 12, 13].

Imaging beyond the ballistic limit is possible by interpreting the scattered light instead of rejecting it [14]. For example, coherent speckle patterns and their correlations can be exploited for imaging [15, 16]. These methods are challenging to implement in aerosols because the speckle decorrelation is sensitive to moving scatterers [17]. Alternatively, incoherent methods that do not take advantage of the wave nature of light can be insensitive to particle motion. For example, diffuse optical imaging (DOI) relies on computational imaging to invert a diffusion model that approximates photon transport in tissue. Through optimization techniques [18, 19], it is possible to detect objects [20], estimate the locations of objects [21] and recover the shapes of objects [19, 18, 22, 23, 24].

A requirement of DOI is sufficient scatter for the diffusion approximation to hold, and image formation is limited to the highly scattering regime and distances greater than a few transport lengths or so from sources and boundaries. As the transport length, l_t, can be tens of meters in fog, an alternative transport model is desired for computational imaging that can operate closer to sources and boundaries. Monte Carlo simulations are a possibility, but they require high-performance computing (HPC) and significant computational time [25, 8, 26], limiting their utility for solving optimization problems that must calculate solutions iteratively, especially in low size, weight, and power (SWaP) systems. Approximate solutions offer a faster alternative and do not require HPC. The moderately scattering regime can be simulated using the small-angle approximation (SAA), which assumes that only the light propagating in a direction close the source direction is significant [3, 4]. The SAA has been used to great effect [27, 28, 29, 30, 17, 31], however it is not applicable in the highly scattering regime or when measurements are made at large angles with respect to the source direction. The highly scattering regime can be simulated using the diffusion approximation, as in DOI. Higher order diffusion approximations can better describe collimated light sources, but they are still not valid in the moderately scattering regime [32].

Recently, we developed a model based on a weak angular dependence approximation [33]. The model appears to be valid in both the moderate and highly scattering regimes, covering applicability domain of both the SAA and the diffusion approximation [33], making it suitable for scattering media like fog, dust, smoke, and tissue. Here, we derive a more general heterogeneous time-dependent solution and explore it's application for computational detection, localization, and imaging of spherical objects hidden in the fog generated at the Sandia National Laboratory Fog Chamber Facility (SNLFC) [33, 34, 8].

2.2. Light Transport in Fog

2.2.1. *Radiative Transfer*

Light transport in scattering media can be described by the radiative transfer equation (RTE) [3, 4]

$$\begin{aligned}\frac{1}{c}\frac{\partial}{\partial t}I(\mathbf{r},t,\hat{\mathbf{\Omega}}) + \hat{\mathbf{\Omega}}\cdot\nabla I(\mathbf{r},t,\hat{\mathbf{\Omega}}) + (\mu_a+\mu_s)I(\mathbf{r},t,\hat{\mathbf{\Omega}}) = \\ \mu_s\int_{4\pi} d\hat{\mathbf{\Omega}}' f(\hat{\mathbf{\Omega}}'\to\hat{\mathbf{\Omega}})I(\mathbf{r},t,\hat{\mathbf{\Omega}}') + Q(\mathbf{r},t,\hat{\mathbf{\Omega}}),\end{aligned} \tag{2.1}$$

where $\mathbf{r} = (x,y,z)$ denotes a position, c is the speed of light in the medium, $I(\mathbf{r},t,\hat{\mathbf{\Omega}})$ (W/m^2/sr) is the radiance at time t in direction $\hat{\mathbf{\Omega}}$, μ_a is the absorption coefficient (m^{-1}), μ_s is the scattering coefficient (m^{-1}), $f(\hat{\mathbf{\Omega}}'\to\hat{\mathbf{\Omega}})$ is the scattering phase function from incidence direction $\hat{\mathbf{\Omega}}'$ to scattering direction $\hat{\mathbf{\Omega}}$, and $Q(\mathbf{r},t,\hat{\mathbf{\Omega}})$ (W/m^3/sr) is the radiance source term. The RTE provides an incoherent model that treats light as particles undergoing elastic collisions within a medium where optical interference effects are assumed to average to zero and are neglected. Integrating (2.1) over solid angle results in the continuity equation

$$\frac{1}{c}\frac{\partial}{\partial t}\phi(\mathbf{r},t) + \nabla\cdot\mathbf{J}(\mathbf{r},t) + \mu_a\phi(\mathbf{r},t) = S(\mathbf{r},t), \tag{2.2}$$

where $\phi(\mathbf{r},t) = \int_{4\pi} d\hat{\mathbf{\Omega}} I(\mathbf{r},t,\hat{\mathbf{\Omega}})$ is the fluence rate (W/m^2), $\mathbf{J}(\mathbf{r},t) = \int_{4\pi} d\hat{\mathbf{\Omega}}\hat{\mathbf{\Omega}} I(\mathbf{r},t,\hat{\mathbf{\Omega}})$ is the flux density (W/m^2), and $S(\mathbf{r},t) = \int_{4\pi} d\hat{\mathbf{\Omega}} Q(\mathbf{r},t,\hat{\mathbf{\Omega}})$ is the source (W/m^3).

2.2.2. Diffusion Equation

We can assume the radiance is linearly anisotropic with weak angular dependence and expand to first order in $\hat{\mathbf{\Omega}}$ as [3, 35, 4]

$$I(\mathbf{r},t,\hat{\mathbf{\Omega}}) = \frac{1}{4\pi}\phi(\mathbf{r},t) + \frac{3}{4\pi}\mathbf{J}(\mathbf{r},t)\cdot\hat{\mathbf{\Omega}}. \tag{2.3}$$

Furthermore, assuming an isotropic source and that the rate of time variation in $\mathbf{J}$ is much lower than the collision frequency, it is possible to relate the flux density to the fluence rate, resulting in Fick's law [36]

$$\mathbf{J}(\mathbf{r},t) = -D\nabla\phi(\mathbf{r},t), \tag{2.4}$$

where the diffusion coefficient $D = 1/[3(\mu_s' + \mu_a)]$, $\mu_s' = \mu_s(1-g)$ is the reduced scattering coefficient, g is the average cosine of the scattering angle, or the anisotropy parameter, and $l_t = 1/\mu_s'$ is the transport mean free path length. As g decreases from 1, the light becomes less forward scattered, $g = 0$ implies isotropic scatter, and negative values imply predominantly backwards scattering. Substituting (2.4) into (2.2), the result is the diffusion equation (DE)

$$\frac{1}{c}\frac{\partial}{\partial t}\phi(\mathbf{r},t) - \nabla\cdot[D(\mathbf{r})\nabla\phi(\mathbf{r},t)] + \mu_a(\mathbf{r})\phi(\mathbf{r},t) = S(\mathbf{r},t). \tag{2.5}$$

It has been found that the DE (2.5) can be invalid within a few l_t of boundaries and sources, and when μ_a is large relative to μ_s [35]. The time-dependent homogeneous Green's function solution to the DE in (2.5) is [37, 38]

$$\phi(\mathbf{r},t) = \frac{S_o c}{(4\pi Dct)^{3/2}}\exp\left(-\frac{|\mathbf{r}-\mathbf{r}_s|^2}{4Dct} - \mu_a ct\right), \tag{2.6}$$

where $\mathbf{r}_s$ is the location of a point isotropic source with energy S_o (J). Solving for $\mathbf{J}$ using (2.4) gives

$$\mathbf{J}(\mathbf{r},t) = \frac{\mathbf{r}-\mathbf{r}_s}{16(\pi Dc)^{3/2}t^{5/2}}\exp\left(\frac{-|\mathbf{r}-\mathbf{r}_s|^2}{4Dct} - \mu_a ct\right). \tag{2.7}$$

2.2.3. Approximate Integral Equation Solution

Equation (2.1) can be written as

$$\frac{1}{c}\frac{\partial}{\partial t}I(\mathbf{r},t,\hat{\mathbf{\Omega}}) + \hat{\mathbf{\Omega}}\cdot\nabla I(\mathbf{r},t,\hat{\mathbf{\Omega}}) + (\mu_a + \mu_s)I(\mathbf{r},t,\hat{\mathbf{\Omega}}) = Q_s(\mathbf{r},t,\hat{\mathbf{\Omega}}), \tag{2.8}$$

where the source is now the in-scattered light

$$Q_s(\mathbf{r},t,\hat{\mathbf{\Omega}}) = \mu_s\int_{4\pi} d\hat{\mathbf{\Omega}}' f(\hat{\mathbf{\Omega}}' \to \hat{\mathbf{\Omega}}) I(\mathbf{r},t,\hat{\mathbf{\Omega}}'), \tag{2.9}$$

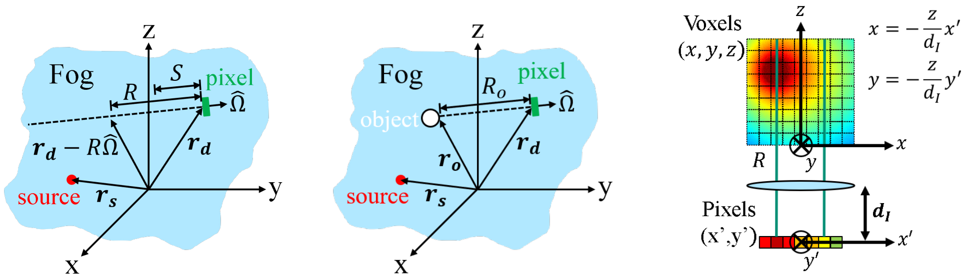

(a) (b) (c)

Figure 2-1. Coordinate systems for calculating the radiance incident on a pixel at $\mathbf{r}_d$ due to a source at $\mathbf{r}_s$. (a) In-scattered light at positions $\mathbf{r}_d - R\hat{\mathbf{\Omega}}$ directed towards the pixel along its line of sight is attenuated and integrated according to (2.15). The optical depth is computed by integrating across positions $\mathbf{r}_d - S\hat{\mathbf{\Omega}}$ according to (2.11). (b) An object at position $\mathbf{r}_o$ blocks the $\hat{\mathbf{\Omega}}$ directed light behind the object, (2.18), and reflects the $-\hat{\mathbf{\Omega}}$ directed light incident on the object, (2.19). (c) Pinhole camera model used to compute the voxel positions $\mathbf{r} = (x, y, z)$ along pixel line of sights using the pixel positions (x', y'), the distance from the camera lens to the pixel array, d_I, and the uniformly discretized z-axis.

or the light that is scattered from incident directions, $\hat{\mathbf{\Omega}}'$, into the direction of interest, $\hat{\mathbf{\Omega}}$. A solution to (2.8) can be found using the line of sight defined by the path length distance R for the pixel or detector in the scattering media (fog) at position $\mathbf{r}_d$ in Fig. 2-1(a). We see then that $\hat{\mathbf{\Omega}} \cdot \nabla = \partial/\partial R$ [35]. Using the method of characteristics, integrating results in [39]

$$I(\mathbf{r}_d, t, \hat{\mathbf{\Omega}}) = \int_0^\infty dR \, \mu_s(\mathbf{r}_d - R\hat{\mathbf{\Omega}}) \exp\left[-\alpha(\mathbf{r}_d, \mathbf{r}_d - R\hat{\mathbf{\Omega}})R\right] \times \int_{4\pi} d\hat{\mathbf{\Omega}}' f(\hat{\mathbf{\Omega}}' \to \hat{\mathbf{\Omega}}) I\left(\mathbf{r} - R\hat{\mathbf{\Omega}}, t - \frac{R}{c}, \hat{\mathbf{\Omega}}'\right), \tag{2.10}$$

where α is the optical thickness accounting for spatial variations in μ_a and μ_s and given by

$$\alpha(\mathbf{r}_d, \mathbf{r}_d - R\hat{\mathbf{\Omega}}) = \int_0^R dS \, \mu_s\left(\mathbf{r}_d - S\hat{\mathbf{\Omega}}\right) + \mu_a\left(\mathbf{r}_d - S\hat{\mathbf{\Omega}}\right), \tag{2.11}$$

where S also represents a distance along the line of sight as shown in Fig. 2-1(a).

We can consider $\hat{\mathbf{\Omega}}$ as being directed towards a detector or pixel in fog, and we can assume a small detector area such that the measured photocurrent is proportional to I. Then, deciphering (2.10), in-scattered light at positions $\mathbf{r} - R\hat{\mathbf{\Omega}}$ and times $t - \frac{R}{c}$ directed towards the detector along the line of sight is attenuated and integrated at the detector. Assuming isotropic scatter ($f(\hat{\mathbf{\Omega}}' \to \hat{\mathbf{\Omega}}) = 1/4\pi$), we arrive at

$$I(\mathbf{r}_d, t, \hat{\mathbf{\Omega}}) = \int_0^\infty dR \, \frac{\mu_s(\mathbf{r}_d - R\hat{\mathbf{\Omega}})}{4\pi} \exp\left[-\alpha(\mathbf{r}_d, \mathbf{r}_d - R\hat{\mathbf{\Omega}})R\right] \phi\left(\mathbf{r} - R\hat{\mathbf{\Omega}}, t - \frac{R}{c}, \hat{\mathbf{\Omega}}'\right), \tag{2.12}$$

Alternatively, we can use the weak angular dependence approximation (2.3). First, with sufficient scatter such that $f(\hat{\mathbf{\Omega}}' \to \hat{\mathbf{\Omega}})$ depends only on the scattering angle, we have that

$$\int_{4\pi} d\hat{\mathbf{\Omega}}' f(\hat{\mathbf{\Omega}}' \to \hat{\mathbf{\Omega}}) = 1, \tag{2.13}$$

$$\int_{4\pi} d\hat{\mathbf{\Omega}}' \hat{\mathbf{\Omega}}' f(\hat{\mathbf{\Omega}}' \to \hat{\mathbf{\Omega}}) = g\hat{\mathbf{\Omega}}. \tag{2.14}$$

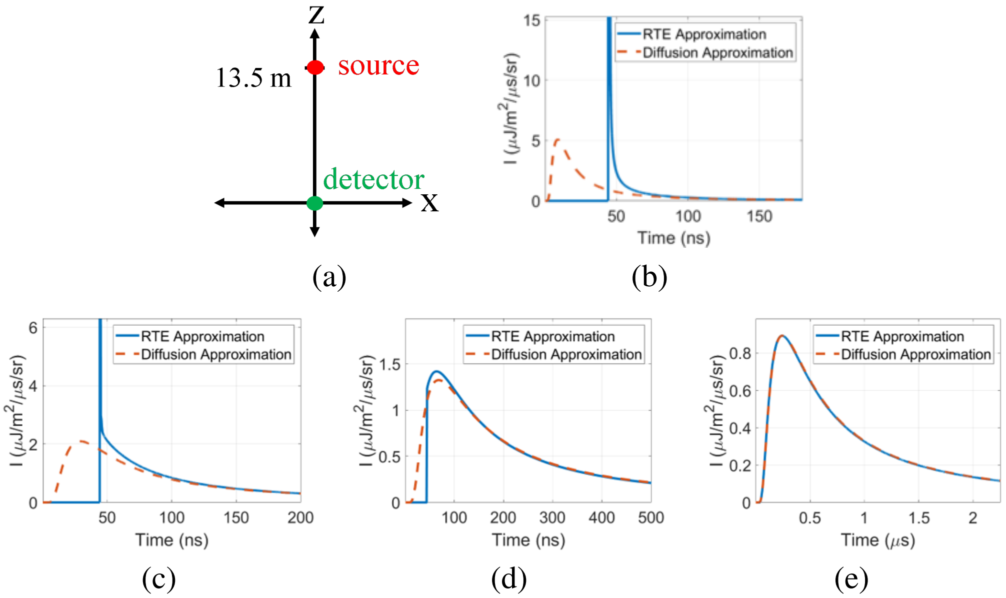

(a) (b)

(c) (d) (e)

Figure 2-2. Computed solutions to (2.15)**, labeled RTE approximation, and the DE, labeled diffusion approximation. (a) Simulation geometry, where** $\mathbf{r}_d = (0,0,0)$, $\mathbf{r}_s = (0,0,13.5)$ **m,** $S_o = 1$ **mJ,** $\mu_a = 0$**, and** $g = 0.8$**, representative of visible light in fog. The scattering coefficient is** $\mu_s = 0.25$ **m**$^{-1}$ **in (b),** $\mu_s = 0.7$ **m**$^{-1}$ **in (c),** $\mu_s = 1.5$ **m**$^{-1}$ **in (d), and** $\mu_s = 5$ **m**$^{-1}$ **in (e). A transition from the moderate to the highly scattering regime [33] occurs at** μ_s **equal to about 0.7, corresponding to** $\tau = 10$**.**

Then, by substituting (2.3) into (2.10) and using (2.13) and (2.14), we find that

$$I(\mathbf{r}_d, t, \hat{\mathbf{\Omega}}) = \int_0^\infty dR\, \frac{\mu_s(\mathbf{r}_d - R\hat{\mathbf{\Omega}})}{4\pi} \exp\left[-\alpha(\mathbf{r}_d, \mathbf{r}_d - R\hat{\mathbf{\Omega}})R\right] \\ \times \left[\phi\left(\mathbf{r}_d - R\hat{\mathbf{\Omega}}, t - \frac{R}{c}\right) + 3g\mathbf{J}\left(\mathbf{r}_d - R\hat{\mathbf{\Omega}}, t - \frac{R}{c}\right) \cdot \hat{\mathbf{\Omega}}\right], \qquad (2.15)$$

Equation (2.15) is an approximate integral equation solution to the RTE that can be solved using the DE. It is the heterogeneous, time-dependent version of the solution presented previously [33]. It contains an additional anisotropic term compared to (2.12), and for the case of isotropic scatter ($g = 0$), reduces to (2.12), as expected. Combining (2.15) with (2.6) and (2.7) provides an analytic time-dependent solution for the light incident on a detector within a homogeneous scattering media.

Equation (2.15) is simulated in Fig. 2-2 with optical properties (μ_s, μ_a, and g) representative of visible light in fog, and compared to the DE solution computed using (2.3), (2.6), and (2.7). The geometry is shown in Fig. 2-2(a), where a detector is located at $\mathbf{r}_d = (0,0,0)$ and an isotropic source is located at $\mathbf{r}_s = (0,0,13.5)$ m. The radiance, $I(\mathbf{r}_d, t, \hat{\mathbf{\Omega}})$, is computed for increasing values of μ_s corresponding to optical depths, $\tau = 13.5 \times \mu_s$, of 3.375, 9.45, 20.25, and 67.5. We see that a transition from the moderate to the highly scattering regime occurs at about $\tau = 10$ [33]. For the highly scattering regime, the approximate integral equation solution, (2.15), matches the DE solution, as expected. Considering the moderate scattering regime, the DE solution is known to be non-causal and not valid.

2.2.4. Forward Model of Light Transport in Fog with Objects

Next we incorporate the effects of objects to develop a forward model that and allows computational sensing of objects. For simplicity, we consider only the homogeneous time-independent solution to (2.15), as was done in [40]. The object can have optical properties that are different than the background, resulting in an interface that reflects, scatters, and transmits light. We consider a spherical object with diameter d, reflection weight Γ, and opacity weight κ located at $\mathbf{r}_o = (x_o, y_o, z_o)$, as shown in Fig. 2-1(b). A forward model can then be written as

$$\mathbf{f}(\mathbf{x}) = \mathbf{y}_b + \kappa\mathbf{S}(\mathbf{r}_o, d) + \Gamma\mathbf{R}(\mathbf{r}_o, d), \tag{2.16}$$

where $\mathbf{x} = [\mathbf{r}_o, d, \Gamma, \kappa]$ are the object parameters, $\mathbf{f}(\mathbf{x})$ is a vector of length P, where P is the number of pixels in the camera array, $\mathbf{y}_b$ is the expected measurement in absence of an object, $\mathbf{S}(\mathbf{r}_o, d)$ is the light blocked by the object, and $\mathbf{R}(\mathbf{r}_o, d)$ is the light reflected by the object. The vector components of $\mathbf{y}_b$, $\mathbf{S}(\mathbf{r}_o, d)$, and $\mathbf{R}(\mathbf{r}_o, d)$ are given, respectively, by

$$\begin{aligned} y_{b_i} &= \frac{\mu_s}{4\pi}\int_0^\infty dR_i \exp\left[-(\mu_s+\mu_a)R_i\right] \\ &\quad \times \left[\phi(\mathbf{r}_d - R_i\hat{\mathbf{\Omega}}_i) + 3g\mathbf{J}(\mathbf{r}_d - R_i\hat{\mathbf{\Omega}}_i)\cdot\hat{\mathbf{\Omega}}_i\right], && (2.17) \\ S_i &= -\frac{\mu_s}{4\pi}\int_{R_o}^\infty dR_i \exp\left[-(\mu_s+\mu_a)R_i\right] \\ &\quad \times \left[\phi(\mathbf{r}_d - R_i\hat{\mathbf{\Omega}}_i) + 3g\mathbf{J}(\mathbf{r}_d - R_i\hat{\mathbf{\Omega}}_i)\cdot\hat{\mathbf{\Omega}}_i\right], && (2.18) \\ \mathbb{R}_i &= I(\mathbf{r}_o, -\hat{\mathbf{\Omega}}_i)\exp[-(\mu_s+\mu_a)R_o], && (2.19) \end{aligned}$$

where i is an index from 1 to P, R_i and $\hat{\mathbf{\Omega}}_i$ define the line of sight for the ith pixel, $I(\mathbf{r}_o, -\hat{\mathbf{\Omega}}_i)$ is computed using (2.15), and R_o is the distance from the pixel or camera to the object. To approximate the effects of specular and diffuse reflection at the object surface, the reflection weight Γ is used to relate the radiance in direction $-\hat{\mathbf{\Omega}}$, towards the object ($I(\mathbf{r}_o, -\hat{\mathbf{\Omega}}_i)$ in (2.19)), to the radiance reflected into direction $\hat{\mathbf{\Omega}}$, towards the detector (see Fig. 2-1(b)). Comparing to our experimental data, we previously found Γ within the range of 0 to 1 [40], so we limit it to this range, however we expect it could be greater than 1 for other geometries and objects we haven't considered, such as when there are multiple sources closer to the object. For the results presented in this manuscript, we consider only opaque objects with $\kappa = 1$. We also assume ϕ and $\mathbf{J}$ are perturbationally affected by the object and that the reflected radiance is attenuated according to the Beer-Lambert law [3, 4].

2.3. Simulated Camera Measurements

For simulated camera measurements, we use the optical parameters of a fog generated at the SNLFC with density 10^5 cm^{-3} and the "SNLFC2" particle size distribution from [33], giving $\mu_s = 0.5$ m^{-1}, $\mu_a = 10^{-8}$ m^{-1}, and $g = 0.8$ for 450 nm light, corresponding to a meteorological optical range (MOR) of 6 m. We also use $S_o = 4$ J and a pixel array at $\mathbf{r}_d$ corresponding to the 2 W 450 nm LED (Thorlabs M450LP1) and the CMOS camera (Basler acA2440) with 2 second integration time used in the experiments described in [33]. The pinhole camera model in Fig. 2-1(c) allows determination of positions $\mathbf{r}$ along each pixel's line of sight using the pixel positions within the 8.4 mm by 7.1 mm camera sensor and $d_I = 5$ cm [33].

Figure 2-3 shows simulated forward model solutions for both a transmission and reflection geometry. More detail can be seen in [40]. The total computation time for each was 4 seconds using MATLAB on a "low-performance computer" (Intel(R) Xeon(R) CPU E5-1630 v4 at 3.7 GHz). To achieve this speed, no loops were used in the MATLAB code implementation. Note the use of both (x, y, z) and (x', y') coordinates corresponding to the pinhole camera model in Fig. 2-1(c). For visualization purposes, the images are rotated 180° such that, effectively, $x = (z/d_I)x'$ and $y = (z/d_I)y'$. The number of voxels equals the number of camera pixels (2464×2056) times the chosen number of discretized points on the z-axis (500), giving about 2.5×10^9 voxels. The voxel positions $\mathbf{r}$ relevant to computing $\mathbf{S}(\mathbf{r}_o, d)$ and $\mathbf{R}(\mathbf{r}_o, d)$ were found using the conditions $\mathbf{r} \cdot \mathbf{r}_o \geq |\mathbf{r}||\mathbf{r}_o| \cos(\theta)$, corresponding to a right circular cone with $\theta = \arctan(d/2/R_o)$, and either $z > z_o + d/2$ or $z < z_o + d/2$, respectively. Therefore, the spherical object is being approximated as a conical frustum.

Comparing $\mathbf{f}(\mathbf{x})$ in Fig. 2-3 for the transmission and reflection cases, the contrast between the object and the background is much greater in the transmission geometry, suggesting the object is easier to detect. Figure 2-4 shows simulated forward model solutions for the reflection geometry and different object positions and diameters. We see that when the object is close to the detector there is high contrast between the object and the background light, and when the object is moved

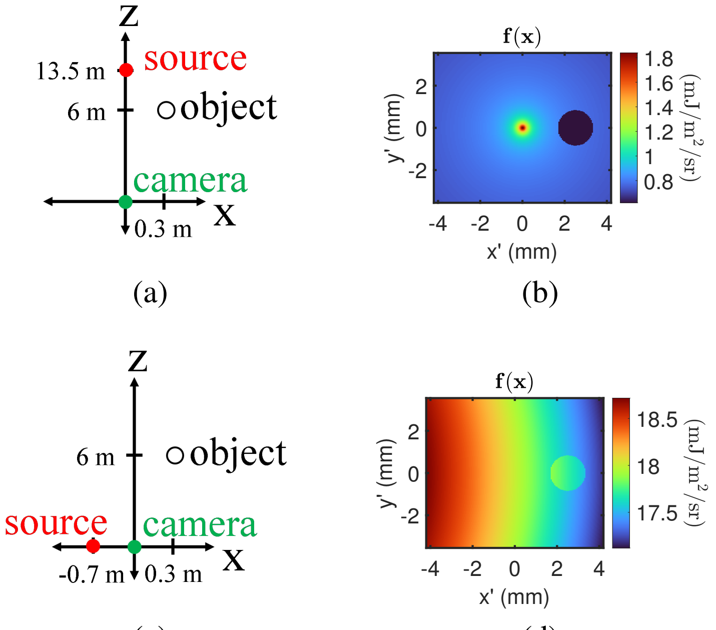

(a) (b)

(c) (d)

Figure 2-3. Simulated forward model solutions, $\mathbf{f}(\mathbf{x})$, computed using (2.16). (a) Transmission geometry with $\mathbf{r}_s = (0, 0, 13.5)$ m, $\mathbf{r}_d = (0, 0, 0)$ m, $\mathbf{r}_o = (0.3, 0, 6)$ m, $\Gamma = 0.9$, and $d = 0.2$ m. (b) The corresponding transmission $\mathbf{f}(\mathbf{x})$. (c) Reflection geometry with $\mathbf{r}_s = (-0.7, 0, 0)$ m, $\mathbf{r}_d = (0, 0, 0)$ m, $\mathbf{r}_o = (0.3, 0, 6)$ m, $\Gamma = 0.9$, and $d = 0.2$ m. (d) The corresponding reflection $\mathbf{f}(\mathbf{x})$. The total computational time for each case was 4 seconds.

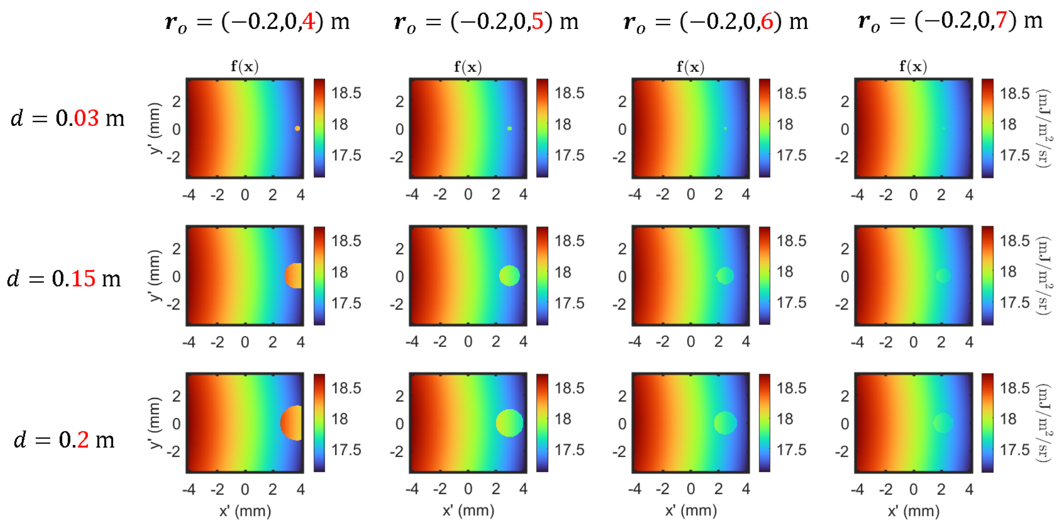

Figure 2-4. Different simulated forward model solutions $\mathbf{f}(\mathbf{x})$ for the reflection geometry in Fig. 2-3(c). The rows correspond to different object diameters d. The columns correspond to different object positions $\mathbf{r}_o$, where the distance to the object is increased. As the object becomes smaller and moves farther away, it's contrast with the background in each image decreases, making it harder to detect.

farther away, the contrast decreases. When the object is 12 m away there is essentially no contrast, implying the object is not detectable (as we will show below). This demonstrates the effect of back-scattered light interfering with a measurement. Comparison with experimental data suggests these model predictions are accurate [40], however further verification is needed, especially for scattering media besides fog and for multiple sources, cameras, and objects.

2.4. Detection

We expand on the work of Milstein *et al.* [41], Cao *et al.* [42], and others [43, 44, 21, 20, 45] to detect and localize opaque objects hidden in fog. Let the hypothesis H_o correspond to the absence of an object and $H_{1,\mathbf{x}}$ to the presence of an object. The probability densities for measurement vector $\mathbf{y}$ under the two hypotheses are then

$$p_o(\mathbf{y}) = \frac{1}{\sqrt{(2\pi)^P|\boldsymbol{\Upsilon}|}} \exp\left(-\frac{1}{2}||\mathbf{y} - w\mathbf{y}_b||^2_{\boldsymbol{\Upsilon}^{-1}}\right), \tag{2.20}$$

$$p_{1,\mathbf{x}}(\mathbf{y}) = \frac{1}{\sqrt{(2\pi)^P|\boldsymbol{\Upsilon}|}} \exp\left(-\frac{1}{2}||\mathbf{y} - w\mathbf{f}(\mathbf{x})||^2_{\boldsymbol{\Upsilon}^{-1}}\right), \tag{2.21}$$

where $\boldsymbol{\Upsilon}$ is the noise covariance matrix with $[\Upsilon]_{ii} = \alpha|y_i|$, α is a scalar parameter of the measurement system that is determined from the signal to noise ratio (SNR) [19], w is a proportionality constant, $||\mathbf{u}||^2_{\boldsymbol{\Upsilon}^{-1}} = \mathbf{u}^T\boldsymbol{\Upsilon}^{-1}\mathbf{u}$, and T is the transpose operation. Letting $\theta = [\mathbf{x}, w]$ be the parameters of interest, the likelihood ratio test (LRT) is

$$L(\mathbf{y}, \theta) = \ln\frac{p_{1,\mathbf{x}}(\mathbf{y})}{p_o(\mathbf{y})} = \mathbf{h}^T(\theta)[\mathbf{y} - w\mathbf{y}_b] - c(\theta), \tag{2.22}$$

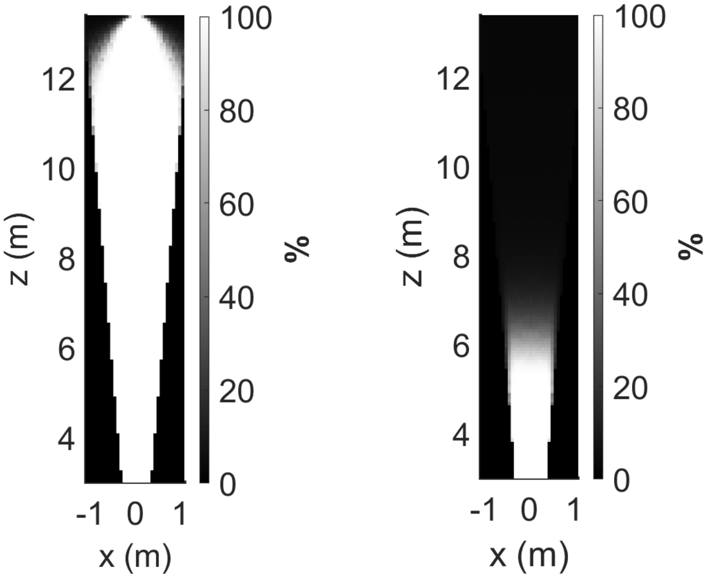

(a) (b)

Figure 2-5. Probability of detecting an object hidden in fog as a function of the object position, $\mathbf{r}_o$, for an assumed $P_F = 3\%$ and $d = 0.2$ m. Slices within the 3-D geometry at $y = 0$ are shown as images. (a) Transmission geometry from Fig. 2-3(a) and assuming a 30 dB SNR. (b) Reflection geometry from Fig. 2-3(c) and assuming a 40 dB SNR. As seen in Fig. 2-4, objects that are further than about 7 m from the camera that is located at the origin are not detectable.

where ln is the natural logarithm, $\mathbf{h}^T(\theta) = [w\mathbf{f}(\mathbf{x}) - w\mathbf{y}_b]^T \boldsymbol{\Upsilon}^{-1}[\mathbf{y} - w\mathbf{y}_b]$, and $c(\theta) = \frac{1}{2}||w\mathbf{f}(\mathbf{x}) - w\mathbf{y}_b||^2_{\boldsymbol{\Upsilon}^{-1}}$, a constant for each θ. According to the Neyman-Pearson lemma, (2.22) provides the highest probability of detection, P_D, for a specified false alarm rate, P_F. The decision statistic $q = \mathbf{h}^T(\theta)[\mathbf{y} - w\mathbf{y}_b]$ then has a normal distribution under the two hypotheses,

$$p_o(q) = \frac{1}{\sqrt{(2\pi)}\sigma_q} \exp\left(-\frac{q^2}{2\sigma_q^2}\right), \tag{2.23}$$

$$p_1(q) = \frac{1}{\sqrt{(2\pi)}\sigma_q} \exp\left(-\frac{(q-\bar{q})^2}{2\sigma_q^2}\right), \tag{2.24}$$

where both the mean $\bar{q}$ and variance σ_q^2 are equal to $||w\mathbf{f}(\mathbf{x}) - w\mathbf{y}_b||^2_{\boldsymbol{\Upsilon}^{-1}}$. For a specified P_F, the detection threshold, $k_{P_F}(\theta)$, can be then determined as $k_{P_F}(\theta) = \sqrt{2}\sigma_q \text{erfinv}(2P_F)$, where erfinv is the inverse error function. Thus, an object is declared present if $q > k_{P_F}(\theta)$, and the probability of detection can be computed as

$$P_D = \frac{1}{2}\text{erfc}\left(\frac{k_{P_F}(\theta) - \bar{q}}{\sqrt{2}\sigma_q}\right), \tag{2.25}$$

where erfc is the error function.

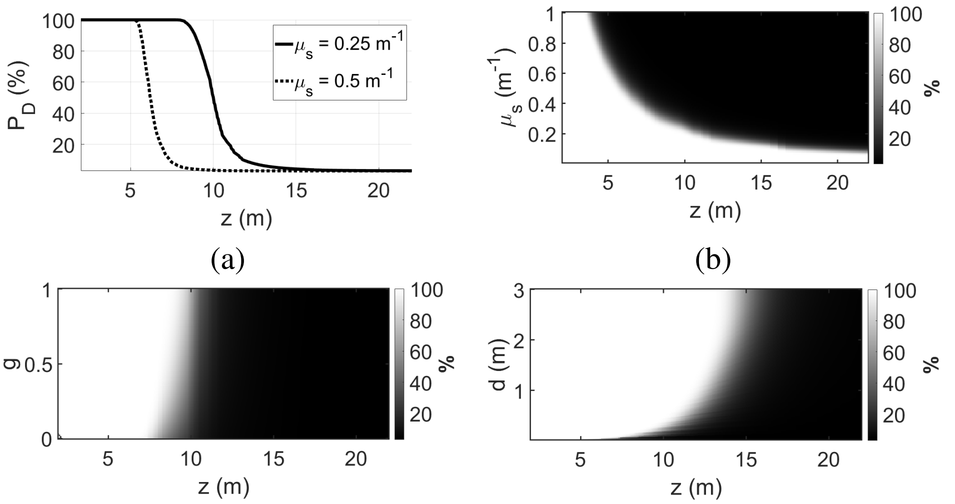

(a) (b)

(c) (d)

Figure 2-6. Influence of depth, μ_s, g, and d on P_D for the reflection geometry of Fig. 2-3(c), with $P_F = 3\%$, $\Gamma = 0.9$, and 30 dB SNR. (a) P_D as a function of object depth, z, where μ_s is designated in the legend, $g = 0.8$, and $d = 0.2$ m. (b) P_D as a function of μ_s, where $g = 0.8$ and $d = 0.2$ m. (c) P_D as a function of g, where $\mu_s = 0.25$ m^{-1} and $d = 0.2$ m. (d) P_D as a function of d, where $\mu_s = 0.25$ m^{-1} and $g = 0.8$.

Simulated calculations of (2.25) are shown in Fig. 2-5 for both the transmission and reflection geometries of Figs. 2-3(a) and (b). The SNR specified in the figure caption was used to determine α using the method described in [41], and w was set equal to 1. Experimentally, α could be estimated for a specific measurement setup and w could represent a linear calibration factor. Figure 2-5 used the optical parameters of the fog described in Section 2.3, which could be determined experimentally be inverting the model using a known calibration object or light source.

Simulated calculations of (2.25) for the reflection geometry of Fig. 2-3(b) are shown in Fig. 2-6 as a function of depth, μ_s, g, and d. Here, the object positions were centered on the z-axis in Fig. 2-3(b) so that the object depth, z, is the distance from the camera to the object. Figure 2-6(a) shows that P_D decreases as the object depth is increased or μ_s is increased. Figure 2-6(b) shows this more comprehensively as a function of both z and μ_s and suggests regions where the object could be classified as either detectable or not detectable. Figure 2-6(c) shows the effect of the average cosine of the scattering angle, g. Surprisingly, whether the light is isotropically scattered ($g = 0$) or forward scattered ($g = 1$) is found to have a limited influence on detection depth limits (less than a factor of 2). This appears to be a multiplescattering effect, as the backscattered light is more important for detection when there is weak scatter. Figure 2-6(d) shows the effect of the object diameter d. As expected, the object can be detected at greater depths as it increases in size. However, once its size is larger than the field of view of the camera there is no longer additional benefit.

From Fig. 2-6(b), we find the following fit for the maximum depth where the object can be detected as a function of μ_s [40]

$$z = 21.98\exp(-12.08\mu_s) + 9.175\exp(-1.063\mu_s). \tag{2.26}$$

This fit is appropriate for predicting detection limits in fog (MOR) for the reflection geometry and a 30 dB SNR measurement with visible light (i.e. $\mu_a \approx 0$). We note that supplemental code is available in [33] to compute μ_s for different fog types. The predictions in Fig. 2-6 and (2.26) are consistent with Fig. 2-4(b), Fig. 2-5(b), and our experimental data (not shown).

2.5. Localization

As in the references [41, 42, 21, 20, 44, 45], we use maximum likelihood (ML) estimation to locate the object. We also characterize the object by estimating its diameter and reflection coefficient. Assuming an object is present or has been detected, using (2.21) and (2.16), the ML can be formulated as

$$c(\mathbf{r}_o, d) = \arg\min_{\Gamma, w} ||\mathbf{y} - w\mathbf{y}_b - w\mathbf{S}(\mathbf{r}_o, d) - w\Gamma\mathbf{R}(\mathbf{r}_o, d)||^2_{\boldsymbol{\Upsilon}^{-1}}, \tag{2.27}$$

where $c(\mathbf{r}_o, d)$ is the negative log likelihood and is treated as a cost function and the goal is to estimate $\mathbf{r}_o$, d, Γ, and w. To accomplish this, for each discretized position $\mathbf{r}_o$ and object diameter d within pre-determined ranges of interest, $c(\mathbf{r}_o, d)$ is first minimized with respect to Γ and w along the search directions given by

$$\tilde{w} = \frac{[\mathbf{y}_b + \mathbf{S}(\mathbf{r}_o, d) + \tilde{\Gamma}\mathbf{R}(\mathbf{r}_o, d)]^T \boldsymbol{\Upsilon}^{-1}\mathbf{y}}{||\mathbf{y}_b + \mathbf{S}(\mathbf{r}_o, d) + \tilde{\Gamma}\mathbf{R}(\mathbf{r}_o, d)||^2_{\boldsymbol{\Upsilon}^{-1}}}, \tag{2.28}$$

$$\tilde{\Gamma} = \frac{[\mathbf{y} - \tilde{w}\mathbf{y}_b - \tilde{w}\mathbf{S}(\mathbf{r}_o, d)]^T \boldsymbol{\Upsilon}^{-1}\mathbf{R}(\mathbf{r}_o, d)}{\tilde{w}||\mathbf{R}(\mathbf{r}_o, d)||^2_{\boldsymbol{\Upsilon}^{-1}}}, \tag{2.29}$$

such that the estimated parameters are given by

$$[\hat{\mathbf{r}}_o, \hat{d}] = \arg\min_{\mathbf{r}_o, d} ||\mathbf{y} - \tilde{w}\mathbf{y}_b - \tilde{w}\mathbf{S}(\mathbf{r}_o, d) - \tilde{w}\tilde{\Gamma}\mathbf{R}(\mathbf{r}_o, d)||^2_{\boldsymbol{\Upsilon}^{-1}}, \tag{2.30}$$

$$\hat{w} = \tilde{w}(\hat{\mathbf{r}}_o, \hat{d}, \hat{\Gamma}), \tag{2.31}$$

$$\hat{\Gamma} = \tilde{\Gamma}(\hat{\mathbf{r}}_o, \hat{d}, \hat{w}). \tag{2.32}$$

In practice, for each interrogated $\mathbf{r}_o$ and d, we first initialized $\tilde{\Gamma}$ to 0.5, computed $\tilde{w}$ using (2.28), computed a new $\tilde{\Gamma}$ using (2.29), then computed a new $\tilde{w}$, and so on for 10 iterations, which we found gave good convergence.

Simulated localization and calculation of (2.27) is shown in Fig. 2-7 for both the transmission and reflection geometries of Figs. 2-3(a) and (b). These results use $[\Upsilon]_{ii} = |y_i|$ rather than $[\Upsilon]_{ii} = \alpha|y_i|$, because α is assumed unknown [41]. This results in an unknown scalar factor for the cost function, which has no effect on the optimization of (2.27). The parameters $\mathbf{r}_o$, d, and Γ were estimated successfully for each case, suggesting that objects in fog can be both localized and characterized using a single camera. We believe $\mathbf{r}_o$ and Γ can be determined uniquely because the fog between the object and the camera affects the measurement differently, depending on the distance to the object and its reflection. We have localized a spherical object, however the same procedure could be adapted to localize objects with more complex shapes.

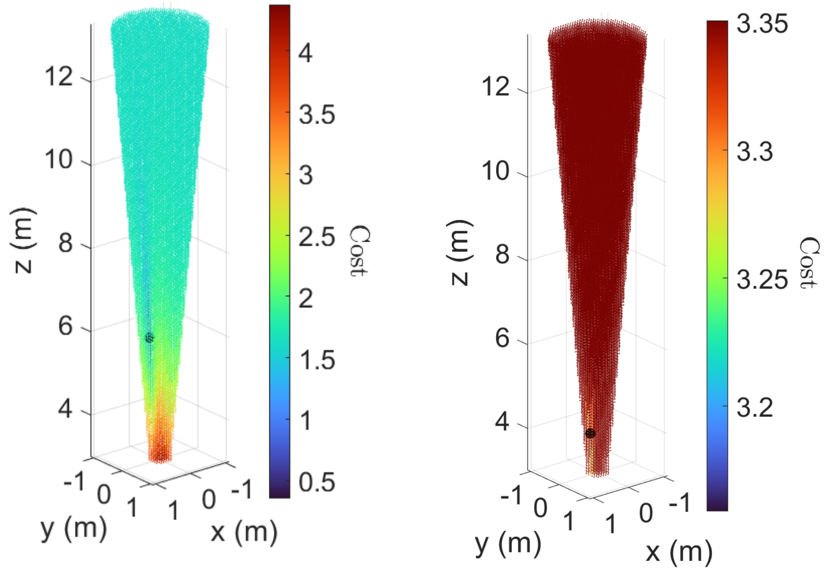

(a) (b)

Figure 2-7. Localization and characterization of objects. (a) Cost in (2.27) calculated for the transmission geometry from Fig. 2-3(a) with $\mathbf{r}_o = (0.3, 0, 6)$ and assuming a 30 dB SNR. (b) Cost in (2.27) calculated for the reflection geometry from Fig. 2-3(c) with $\mathbf{r}_o = (0.3, 0, 4)$ and assuming a 30 dB SNR. The parameters $\mathbf{r}_o$, d, and Γ were estimated successfully for each case. The black dot designates the correct object location, $\mathbf{r}_o = (-0.22, 0, 8)$ m, where the cost reaches a global minimum. The contrast in cost is much less for the reflection geometry because the object is almost undetectable.

2.6. Imaging

Considering (2.16), $\mathbf{y}_b$ could be treated as a background contribution to the measurement. Subtracting $\mathbf{y}_b$ would then isolate the effect of the object, $\kappa\mathbf{S}(\mathbf{r}_o, d) + \Gamma\mathbf{R}(\mathbf{r}_o, d)$, effectively reducing the effect of the scattering media on the image. In a similar approach known as dehazing, $\mathbf{y}_b$ is estimated and removed [46, 47]. However, current dehazing approaches are limited to the weakly scattering regime because they do not account for multiple scattering. Here, using (2.15), it becomes possible solve the “dehazing” problem in the moderate and highly scattering regimes.

In Sections 2.4 and 2.5, we have assumed the optical properties μ_s, μ_a, and g are known, for example, measured by a transmissometer and particle sizer as described in [33, 40]. For computational sensing applications, it would be practical to estimate the optical properties from an image rather than relying on additional equipment. This can be done using the image data in a region removed from the object location and computing

$$[\hat{\mu}_s] = \arg\min_{\mu_s} ||\mathbf{y} - \tilde{w}\mathbf{y}_b(\mu_s)||^2_{\boldsymbol{\Upsilon}^{-1}}, \tag{2.33}$$

where $\tilde{w} = (\mathbf{y}_b^T \boldsymbol{\Upsilon}^{-1}\mathbf{y})/(||\mathbf{y}_b||^2_{\boldsymbol{\Upsilon}^{-1}})$. Next, the dehazed image can be computed as

$$\mathbf{y}_{dehaze} = \mathbf{y} - \tilde{w}\mathbf{y}_b(\hat{\mu}_s), \tag{2.34}$$

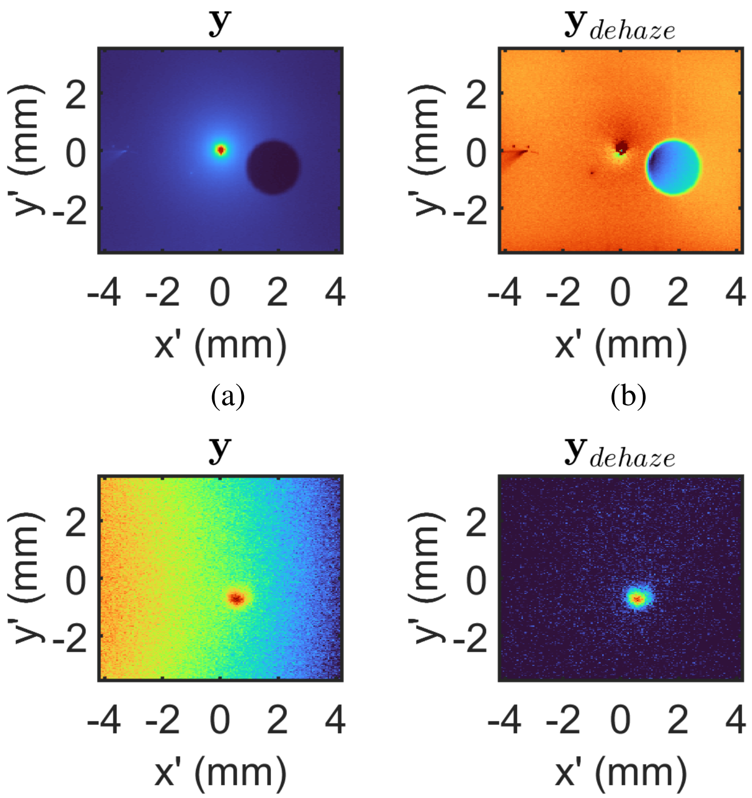

(a) (b) (c) (d)

Figure 2-8. Image dehazing through estimation and subtraction of the effect of scatter, $\mathbf{y}_b$. (a) Experimental data measured in the transmission geometry, where $\mathbf{r}_s = (0,0,13.5)$ m, $\mathbf{r}_d = (0,0,0)$ m, $\mathbf{r}_o = (0.15,-0.05,4)$ m, $\Gamma = 0.1$, and $d = 0.15$ m. The true fog parameters are $\mu_s = 0.24$ m^{-1}, $\mu_a = 10^{-8}$, and $g = 0.8$. The estimated $\hat{\mu}_s = 0.2$ m^{-1}. The object is a Styrofoam sphere painted black. (b) Dehazed image from (a). (c) Experimental data measured in the reflection geometry, where $\mathbf{r}_s = (-0.7,0,0)$ m, $\mathbf{r}_d = (0,0,0)$ m, $\mathbf{r}_o = (0.03,-0.03,2)$ m, $\Gamma = 1$, and $d = 0.03$ m. The true fog parameters are $\mu_s = 1.0$ m^{-1}, $\mu_a = 10^{-7}$, and $g = 0.83$. The estimated $\hat{\mu}_s = 2$ m^{-1}.

where $\hat{w} = \tilde{w}(\hat{\mu}_s)$. This treatment has assumed μ_a and g are known. For the case of visible light in fog, we can assume to good approximation that $\mu_a = 0$ and $g = 0.8$. However, there will be significant error introduced into $\hat{\mu}_s$ compared to the true value. We consider this error to be acceptable since our goal is to calculate $\mathbf{y}_{dehaze}$. A procedure that estimates μ_a and g as well as μ_s could be implemented to better characterize the optical properties of fog.

Representative results of the dehazing procedure using experimental data are presented in Fig. 2-8. Figure 2-8(a) shows experimental data acquired in the transmission geometry [33, 40], and Fig. 2-8(b) shows the corresponding dehazed image, $\mathbf{y}_{dehaze}$. For these images, the $\mu_s = 0.24$, as measured by the transmissometer and particle sizer, and $\hat{\mu}_s = 0.2$ m^{-1}. We consider this error in $\hat{\mu}_s$ to be low. Figure 2-8(c) shows experimental data acquired in the reflection geometry [33, 40], and Fig. 2-8(d) shows the corresponding dehazed image, $\mathbf{y}_{dehaze}$. For these images, the $\mu_s = 1.0$, as measured by the transmissometer and particle sizer, and $\hat{\mu}_s = 2.0$ m^{-1}. This error is much higher than in Figs. 2-8(a) and (b), and could be caused by the transmissometer and particle sizer measurement not accounting for multiple scattering properly. In fact, in general we observed good agreement between $\hat{\mu}_s$ and the value given by the transmissometer and particle sizer when the scatter was low ($\mu_s < 0.5$ m^{-1}), however the error was substantial when the scatter was high ($\mu_s > 0.5$ m^{-1}). Therefore, improving the transmissometer and particle sizer measurements would likely reduce the error when the scatter is high.

The dehazed images in Figs. 2-8(b) and (d) show the effect of the object and could be used to better identify the object. For example, in Fig. 2-8(b), the fishing line holding the object is visible near $(2,2)$ mm and light from the transmissometer is visible near $(-4,0)$ mm. Since the source in the experiment is not isotropic, differences between the model and data can be seen at $(0,0)$ mm. In both Fig. 2-8(b) and (d), the curvature of the spherical objects surface is much more apparent.

2.7. Conclusion

We have presented a time-dependent model that approximates light transport in heterogeneous scattering media. This may be the case because the diffusion approximation is only applied to the in-scattering term in the RTE by leveraging an integral equation solution (2.15). Previously, separate models based on either the small angle approximation or diffusion approximation were required for moderate or highly scattering regimes, respectively [4]. The model can be used to characterize the effects of scattering on imaging and to detect, localize, and image objects in aerosols [48, 49, 50]. Compared to Monte Carlo [8], the computational time is minimal and high-performance computing is not needed, ideal for low size, weight, and power (SWaP) systems and when $\mathbf{f}(\mathbf{x})$ must be computed iteratively. Direct comparison of the computational time with Monte Carlo is difficult because our model has not been parallelized. However, running on a single core, we find that our model (written in MATLAB) is on the order of 10,000 times faster than the MC code used in references [7, 8] (written in C++). We believe our model could be parallelized and achieve similar performance when compared to Monte Carlo on HPC. We examined computational detection, localization, and imaging of a spherical object in an infinite domain, but other shapes could be considered and boundary conditions incorporated. The model could be useful for the tissue imaging problem [51, 52], especially in tissue slices or near the surface where there is moderately scattered light.

Possible future work includes theory, simulations, and experiments to better treat boundaries and light sources [18, 19, 21, 45, 10]. Higher-order diffusion approximations could be leveraged to better model collimated sources in the moderately scattering regime [25, 32]. A spatially modulated structured light source could be incorporated into the model to improve spatial resolution and contrast [53, 54]. Numerical solutions based on the finite element method (FEM) [55] could be employed to model heterogeneous scattering media. It may be possible to seek alternative solutions to the vector radiative transfer equations to treat polarized light [3, 28, 29].

3. DEVELOPMENT AND CHARACTERIZATION OF A TABLETOP FOG CHAMBER

3.1. Introduction

Fog presents a widespread, complex issue for the sensing world. Furthermore, there is significant case-by-case variation between fogs in nature, even within the same region [56, 57, 58, 59]. This creates a complex problem space, where optical systems must be able to function in a wide variety of scattering environments to be able to sense through fog [60, 61, 33, 40, 8]. It is therefore important that we be able to repeatably generate multiple different fogs to test optical systems in a robust manner. To this end we have developed and characterized a tabletop chamber capable of reliably generating a variety of repeatable fog-analogues [62].

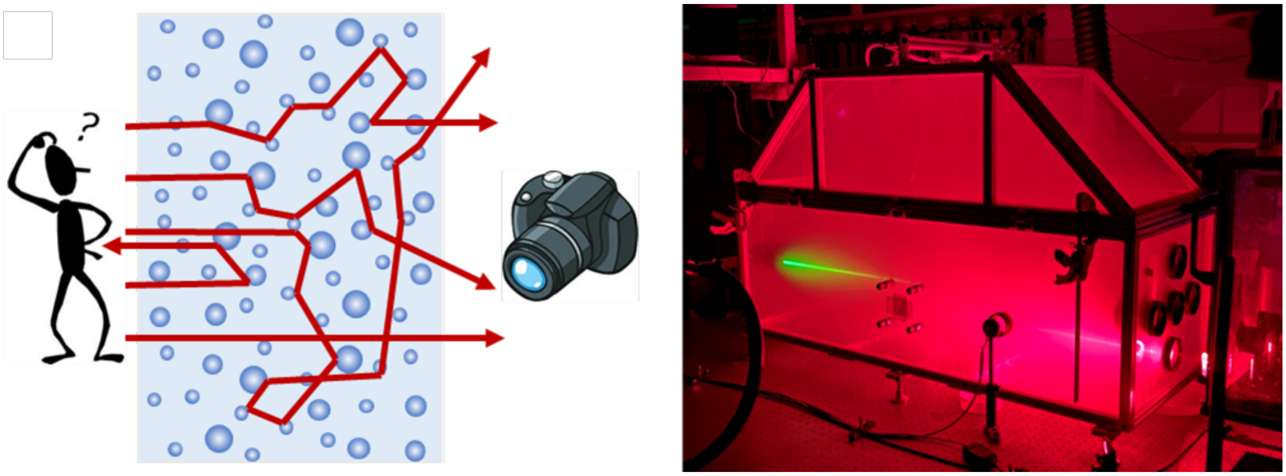

(a) (b)

Figure 3-1. Light scattering in fog, shown by (a) an illustration depicting light randomly scattering off of fog droplets of varying sizes and (b) an image of light from two different collimated sources (a 670 nm red laser and a 532 nm green laser) being scattered in the Tabletop Fog Chamber described herein. Each beam travels roughly 30 cm within the chamber before becoming isotropic.

3.2. Droplet Size Distribution and Light Attenuation in Fog

3.2.1. Köhler Theory of Droplet Nucleation

In real-world environments fog most often occurs through either the rapid cooling of supersaturated air, or an inversion of cooler, dry air and warm, moist air [56, 57, 59]. In either case, the thermodynamic equilibrium of droplet formation within the fog is described by the Köhler equation [56]:

$$S_{v,w} = \exp\left[\frac{2M_w\sigma_{s/r}}{RT\rho_w r} - \frac{v\phi_s m_s M_w/M_s}{(4\pi r^3\rho_s/3) - m_s}\right] \tag{3.1}$$

where $S_{v,w}$ is the saturation ratio at the surface of the droplet, M_w is the molecular weight of water, $\sigma_{s/r}$ is the droplet surface tension, R is the ideal gas law constant, T is the temperature, ρ_w is the density of water, r is the droplet radius, v is the number of dissolved ions present within the droplet, ϕ_s is the osmotic coefficient, m_s is the mass of solute present within the droplet, M_s is the molecular weight of the solute, and ρ_s is the density of the aqueous solution.

Figure 3-2 displays a curve that describes how the size of a droplet with a specific solute concentration will increase or decrease depending on $S_{v,w}$. In essence, 3.1 describes droplet growth as a relationship controlled by two competing factors, the curvature and solute effects. Due to surface tension, water evaporates from a flat surface faster than curved surface, a phenomenon known as the curvature effect. The curvature effect defines a relationship such that a higher relative humidity is required to sustain smaller droplets have greater curvature/surface tension. If the droplet contains a dissolved salt, also known as a cloud condensation nuclei (CCN), the water in that droplet becomes less likely to evaporate due to the solute effect. To nucleate a homogeneous water droplet from water vapor molecules (i.e. one without solute), an ambient relative humidity of greater than 20 million percent would be required. Therefore, homogeneous nucleation is not possible. The competing influences of the curvature and solute effects, however, enable droplets to form at reasonable supersaturation ($SS = RH - 100\%$), known as the critical supersaturation which is located at the peak depicted in Figure 3-2. The critical supersaturation corresponds to a critical droplet diameter; if a droplet is able to achieve its critical diameter, it will continue to grow. Aerosols that have undergone deliquescence, but that have not achieved their critical diameter (haze droplets), will have a pseudo-stable diameter that may increase or decrease with relative humidity, but that will never achieve unbounded growth (labelled as the “Saddle Point” in Figure 3-2) [56, 60, 62].

In real-world environments the amount and type of solutes present in the atmosphere vary, but often include salt (near sources of salt water), lead, sulfur oxides, carbon oxides, and nitrogen oxides [63]. Since many fogs occur near coastlines, we will largely focus on the effects of salt on droplet size for this work.

3.2.2. Mie Theory of Light Attenuation in Fog

Light attenuation by spherical particles can be approximated with Mie Theory [34, 33, 40, 8]. Since fog droplets are roughly spherical, Mie Theory provides a good basis for calculating the attenuation of light through fog [34, 33, 40, 8, 61, 60, 62]. A simplified calculation for the scattering coefficient, (3.2), provides a useful basis for the discussions contained within this chapter:

$$\mu_s = \frac{3V}{4\pi}\sum_i \frac{\sigma_{scatter}(r_i,\lambda)v_i}{r_i^3} \tag{3.2}$$

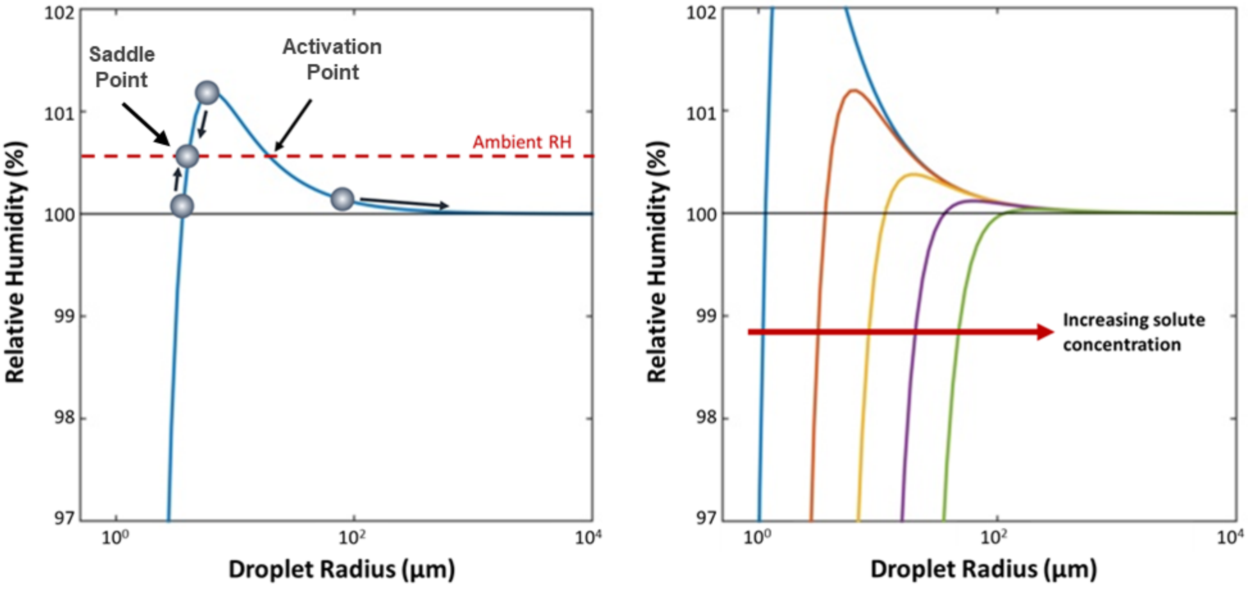

(a) (b)

Figure 3-2. Graphical depictions of Köhler curves, modified with permission from [60]. (a) A depiction of a single Köhler curve, showing droplet growth trends towards either the labelled saddle point, or growth past the labelled activation point. (b) A set of Köhler curves depicting how modifying solute concentration changes the shape and intersections of the curve.

where μ_s is the scattering coefficient of the fog, V is the overall volume fraction of fog droplets in the ambient environment, $\sigma_{scatter}$ is the scattering cross section of a droplet with radius r_i for light with wavelength λ, and v_i is the relative volume fraction of droplets with radius r_i. This formulation is convenient for this chapter because it shows the dependence of the scattering coefficient (the ability of the fog to scattering light) on the droplet diameter and overall volume concentration of droplets in the environment.

It is important we understand the fundamentals of (3.1) and (3.2) so that we can understand the effect that changing the solute concentration has on visibility. To do so we use the scattering Mean Free Path (MFP), l_s, which is the average distance between scattering events within the fog, given by:

$$l_s = \frac{1}{\mu_s} \tag{3.3}$$

This term is useful for understanding visibility as after ten (10) scattering events light from a collimated beam becomes isotropic, and information becomes challenging to decipher with conventional signal recovery approaches [33, 40, 62]. This term is also useful because we can use it to calculate the Meteorological Optical Range (MOR), which is defined as the distance required to reduce the flux of a collimated beam to 5% of its initial value. MOR is often used in transportation and meteorology, and as such is a useful metric for comparing and communicating the impacts of different fogs [64, 8, 61]. We have shown before that in the visible spectrum, where water has low absorption, MOR can be approximated as the same distance as three (3) scattering paths [40], giving:

$$MOR = \frac{-\ln(0.05)}{\mu_s} \approx 3l_s \tag{3.4}$$

This correlation both allows us to predict transmission through fog and provides a useful parameter for comparing our generated fogs to real-world atmospheric conditions, giving relevance to optical tests performed within our tabletop chamber.

It is fundamental that we understand both 3.2.1 and 3.2.2 as together they go to show that atmospheric conditions and composition will dictate aerosol formation, which in turn will dictate light scattering and thus the efficacy of remote sensing, imaging, etc. Thus, to combat this we must develop a test-bed capable of generating a wide variety of fogs-like environments.

3.3. Tabletop Chamber Design

3.3.1. Tabletop Fog Chamber "MiniFog"

Our final chamber design (Figure 3-3) is a 48” x 18” x 15” rectangular chamber with an additional 15” of head space to allow for fog generation and mixing. We designed the head space as a 45° isosceles trapezoid to accommodate the angle of the spray nozzle while minimizing dead space above the rectangular testing chamber. The chamber is constructed from $\frac{1}{4}$” thick acrylic paneling and 1” aluminum t-slots, sealed with silicone epoxy at the connections and clamped along the lid line to ensure no leaks occur during experiments.

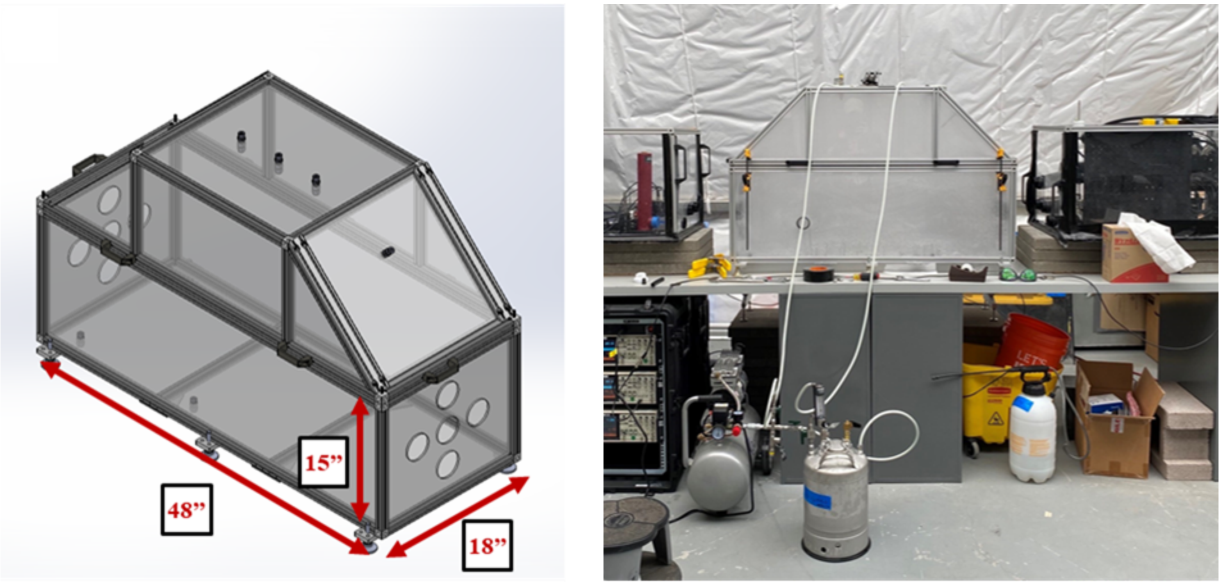

(a) (b)

Figure 3-3. The Sandia National Laboratories Tabletop Fog Chamber (otherwise called the "MiniFog" chamber) shown both (a) as an initial schematic and (b) assembled at a test site.

The fog generation system consists of an air compressor, a water tank, and a 1/4J air atomizing spray nozzle from Spraying Systems Co. We selected this nozzle because it generates aerosolized droplets at atmospherically relevant diameters ($< 100\mu m$) [56]. The nozzle operates by atomizing a water flow from the tank with a shearing air flow, spraying fog droplets into the chamber. Both head pressure for the water tank and the shearing airflow are generated by the compressor.

The chamber is equipped with six optical paths (five across the long axis of the chamber and one across the short axis) each fitted with hydrophobic, optical windows which are transparent in the visible waveband, and multiple ports with Swage connections. These paths and ports allow for many different configurations of equipment to support testing needs. Figure 3-3 shows one such possible configuration of the test chamber, where several of the longer optical paths are utilized for fog characterization tests.

3.3.2. Diffusion Study Tabletop Fog Chamber "MesoFog"

A secondary, larger chamber is currently under construction in support of the Pluminate LDRD (LDRD 226083). This chamber is designed to study diffusion of and within atmospheric aerosols on a tabletop scale. The new system is made from the same materials as the current system, is double the overall length of the current system, and will include a retractable panel in the center to allow for two stable aerosols to be generated in separate halves of the chamber and then be allowed to mix. The design of this system can be seen in Figure 3-4.

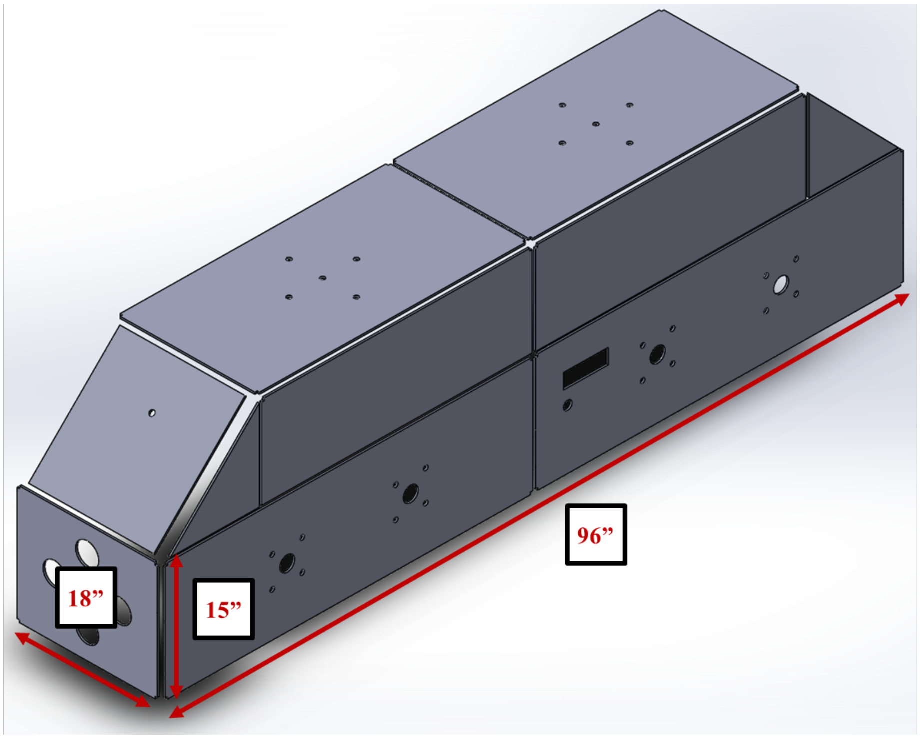

Figure 3-4. Initial schematic of the Sandia National Laboratories Diffusion Study Tabletop Fog Chamber (otherwise called the "MesoFog" chamber). System is currently under construction.

3.4. Fog Characterization

3.4.1. Characterization Equipment

Droplet size distribution measurements were performed by a Malvern Spraytec, a diffraction-based particle sizer that was connected to the chamber via an inhalation cell. Optical transmission through the chamber was measured by an in-house transmissometer. The transmissometer measures transmission at multiple wavelengths ($532nm$, $1550nm$, and $9.68\mu m$), and was aligned through the central full-length optical paths of the tabletop fog chamber, as shown in Figure 3-3. All these pieces of equipment are also utilized at the SNLFC.

3.4.2. Spray Regime

We generate fog in the tabletop fog chamber by spraying through the nozzles until a maximum optical density is achieved, indicated by the stabilization of transmission through the chamber. We then turn off the fog generation system and allow the fog to evolve and dissipate. In the current configuration it takes the system three minutes to reach a maximum density point and about ten minutes to fully dissipate, depending on the type of fog generated.

3.4.3. Fog Parameter Sets

As we have discussed several times in this chapter, for this system to be a useful optical test-bed it must be able to generate several fog-like environments with varied droplet size distributions and overall droplet number densities. To this end we designed six different sets of input parameters. Five of these parameter sets focus on the effects of adding solute to the feed water (Tabletop Fogs 1-5), while the sixth tested the effect of changing the volume of water sprayed during a spray (Tabletop Fog 6).

Tabletop Fog 1. This fog-analogue was generated by spraying feed water with no solute present (only distilled water) through the fog generation system at 72 psi.

Tabletop Fogs 2-4. These fog-analogues were generated by spraying feed water with an increasing concentration of salt (sodium chloride, NaCl) in the feed water at 72 psi. The concentrations were 10, 20, and $30\frac{g}{L}$ respectively.

Tabletop Fog 5. This fog-analogue was generated by spraying feed water with a salt concentration of $35\frac{g}{L}$ at 72 psi. This concentration was selected in addition to the concentrations in Tabletop Fogs 2-4 because it is roughly the average salinity of sea water. [65]

Tabletop Fog 6. This fog-analogue was generated with the same salinity as Tabletop Fog 2 ($10\frac{g}{L}$) but at a lower system pressure (40 psi).

3.5. Results

Over the duration of this project each of these parameter sets was run a minimum of 15 times for characterization purposes, often this number was much higher due to collaborations and other tests. Please see 3.9 for details regarding these collaborations. All fog-analogues generated by this system proved to be optically and microphysically different from one another and highly repeatable. Additionally, the chamber proved to be simple to operate, requiring less than an hour of set up and tear down and able to be run with only a single operator.

Table 3-1. Microphysical and optical properties of the generated Tabletop Fogs.

Comparison of Tabletop Fogs					
Fog Parameter Set	Mean Diameter (μm)	Average Density (cm^{-3})	Maximum Density (cm^{-3})	Mie Scattering (m^{-1})	Average MOR (m)
Tabletop 1	1.58	$9.8x10^4$	$1.6x10^5$	2.8	1.10
Tabletop 2	1.70; 12.1	$2.0x10^5$	$4.2x10^6$	6.1	0.49
Tabletop 3	1.71; 9.26	$3.2x10^5$	$6.5x10^5$	5.6	0.54
Tabletop 4	3.16; 19.1	$3.4x10^5$	$5.7x10^5$	5.4	0.53
Tabletop 5	3.19; 23.3	$3.7x10^5$	$5.6x10^5$	5.7	0.55
Tabletop 6	1.87	$1.0x10^4$	$2.0x10^4$	4.1	0.70

3.5.1. Tabletop Fog 1

The fog-analogue generated with no solute present in the feed water had the lowest mean droplet diameter and density, showed only a single mode, and did not fully obscure the chamber across the 1 meter path length. A representative droplet size distribution can be seen in Figure 3-5 (a).

3.5.2. Tabletop Fogs 2-5

The fog-analogues generated with 10 to $35\frac{g}{L}$ salt concentration gradually increased in mean particle diameter and decreased in average and maximum droplet densities. Commensurately, the average meteorological optical range for visible light was changed as the droplet size distribution was altered. The full table of measured and calculated parameters can be seen in Table 3-1. Representative droplet size distributions can be seen in Figure 3-5 (b)-(e).

3.5.3. Tabletop Fog 6

The fog-analogue generated by this parameter set had a similar particle diameter distribution as the **Tabletop Fog 2**, which had the same solute concentration ($10\frac{g}{L}$), however with significantly lower average and maximum densities. See Table 3-1 and Figure 3-6 (b).

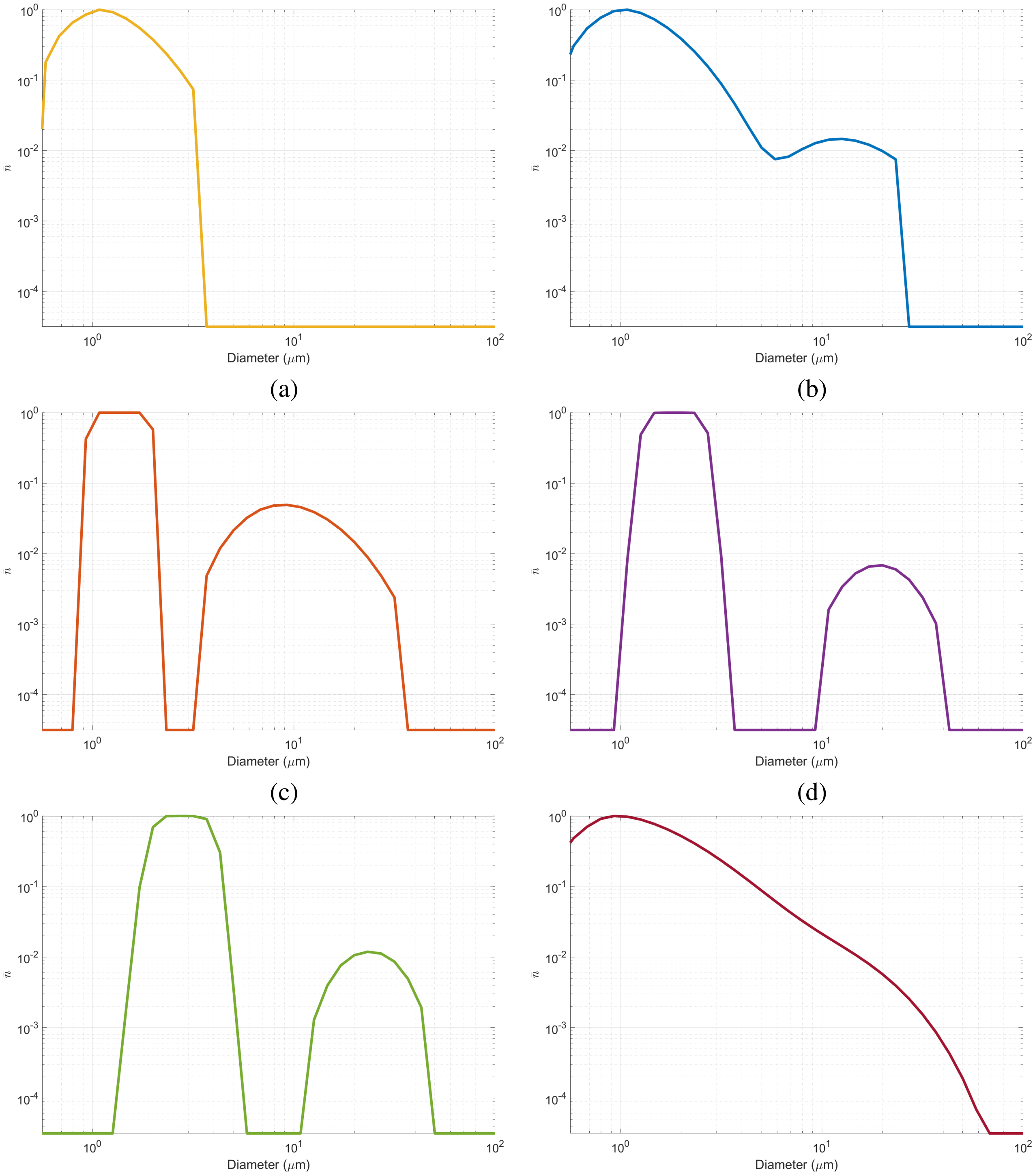

(a) (b) (c) (d) (e) (f)

Figure 3-5. Droplet distribution plots of the generated aerosols. (a) Tabletop Fog 1, no solute. (b) Tabletop Fog 2, $10\frac{g}{L}$ salt. (c) Tabletop Fog 3, $20\frac{g}{L}$ salt. (d) Tabletop Fog 4, $30\frac{g}{L}$ salt. (e) Tabletop Fog 5, $35\frac{g}{L}$ salt. (f) Tabletop Fog 6, $10\frac{g}{L}$ salt, low pressure injection.

3.6. Discussion & Applications

3.6.1. Fog Generation Microphysics

The observed results are in good agreement with Köhler theory (Section 3.2.1). Changing the solute concentration in the feed water has a clear and significant impact on the microphysical properties of the fog. As solute concentration increases, we can see that the mean droplet diameter size of the dominant mode gradually increases (see Figure 3-6 and Table 3-1).

The average number density increases similar to the mean droplet diameter, however the maximum number density gradually decreases (Table 3-1). This phenomenon is likely due to the fact that **Tabletop Fogs 1-5** were each generated under the same operating pressure. As such they each contained approximately the same overall liquid water content (LWC). As droplet diameter increased the number of droplets naturally decreased as larger droplets consumed more of the overall available water. The increase in average number density is due to the increased longevity of the aerosols. As the solute concentration increases within the droplets so too does the hygroscopicity of each droplet, defined as the chemical potential of the droplet with respect to water [56]. As the hygroscopicity increases there is an overall increase in the longevity of the droplet in the environment, leading to the seen increase in average number density seen in Table 3-1.

Comparing **Tabletop Fog 2** and **Tabletop Fog 6** (Figure 3-6 (b), Table 3-1), which were generated with the same solute concentration but at two different pressures, we can see that the two fog-analogues appear similar in regards to average number density and apparent mean droplet diameter of the dominant size mode. Though the mean diameters appear significantly different in Table 3-1, by plotting the diameter distributions (Figure 3-6 (b)) we can see that the dominant diameter is nearly identical between the fog-analogues, and the main difference comes from the

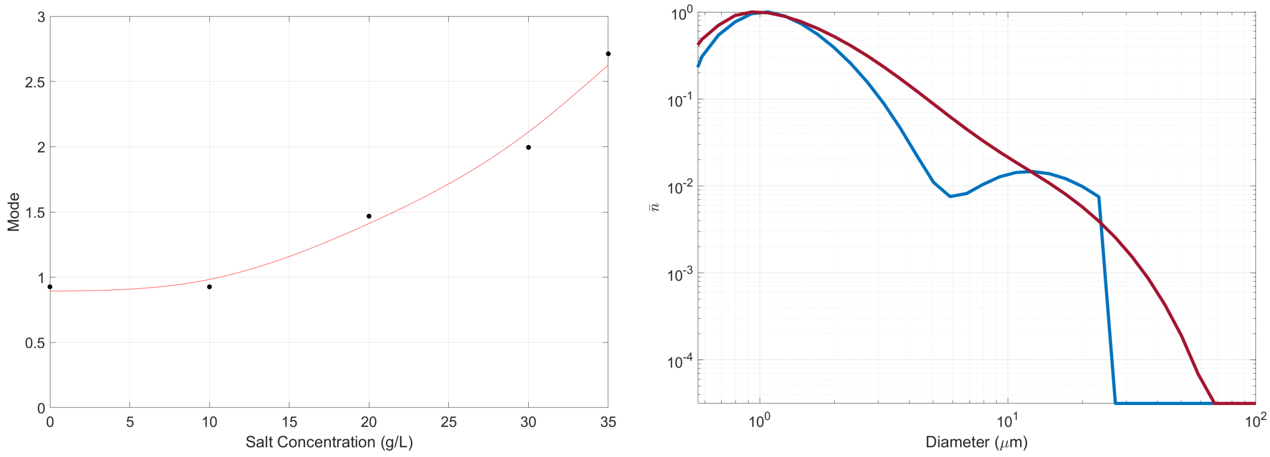

(a) (b)

Figure 3-6. (a) Comparison of salt concentration and resultant first mode droplet diameter of generated fogs. Red trendline indicates parabolic increase in modal diameter as a result of increased salt concentration. (b) Comparison of Tabletop Fogs 1 and 6. Both generated with 10 $10\frac{g}{L}$ salt in the feed water. Both fogs show similar ranges.

lack of a distinct secondary mode in **Tabletop Fog 6**. When truncating the size distribution data to below 5 μm (the inflection point of between size modes in **Tabletop Fog 2**) the resultant mean diameter of **Tabletop Fog 6** shifts to 1.62 μm, becoming statistically indistinguishable from **Tabletop Fog 2**. Since the two fogs were generated with the same solute concentration we anticipated that the mean droplet diameters would be nearly identical. Indeed, the fogs appear to be nearly identical in distribution, and are different only in overall number density of droplets. This tells us that we are able to generate the same fog-analogue at different densities by holding solute concentration constant and instead altering the system pressure of the chamber.

Furthermore, a bimodal droplet size distribution can be seen in sprays with a solute present, as is also predicted by Köhler theory (Section 3.2.1). By analyzing the gradual development and separation of the secondary mode in Figures 3-5 (b)-(e) we can see that the mean diameter of this mode also increases with respect to solute concentration. This adherence to theory suggests that the generated fog-analogues are representative of real-world fogs and aerosols [56, 57, 59].

3.6.2. Fog Optical Properties

As discussed in Section 3.2, as the microphysical properties of the fog change, so too do the optical properties. We can see this to be true in Table 3-1, where each generated fog has a unique Mie scattering coefficient and MOR value. This variety allows us to generate multiple different conditions relevant to real-world environments that might affect industries such as security, remote sensing, and transportation. A quarter (25%) of all transportation accidents are caused by inclement weather, including fog [58]. By being able to better simulate naturally occurring fogs, we can begin to test next-generation optical equipment for transportation instrumentation.

The International Civil Aviation Organization (ICAO) defines several categories of inclement visibility as standards for aviation. Category IIIb is the most severely visually impaired of these categories, defined by ICAO as less than 200 meters of visibility along a runway [66]. In Category IIIb conditions pilots are required, and often times only able, to navigate using instrumentation only. As such, it is clearly advantageous to be able to test aviation equipment in these conditions prior to deployment. Using the Tabletop Fog Chamber we are able to simulate out to 200 meters of ICAO Category IIIb conditions with the various fogs generated in this section.

By being able to reliably replicate a variety of aviation-relevant fogs this chamber can test optical equipment in relevant environments prior to real-world deployment.

Section 3.9 details current optical research that this chamber is supporting and has supported throughout this LDRD.

3.6.3. Scale Up

We can compare our tabletop chamber to the SNLFC, our large-scale research facility. Figure 3-7 shows droplet size distributions of the fogs generated in the tabletop chamber plotted with fog measured in previous experiments at the SNLFC [60, 33, 40, 8]. The SNLFC fog was generated in a manner like **Tabletop Fog 2** in this experiment, with $10\frac{g}{L}$ salt added to the feed water [60, 8]. As

Table 3-2. Comparison of experimentally generated Tabletop Fogs to equivalent aeronautical distances.

Average Aerospace Relevant Values			
Fog Parameter Set	Droplet Density (cm^{-3})	MOR for Visible Light (m)	Equivalent Distance in ICAO Cat. IIIb Conditions (m)
Tabletop 1	$9.8x10^4$	1.10	90
Tabletop 2	$2.0x10^5$	0.49	200
Tabletop 3	$3.2x10^5$	0.54	185
Tabletop 4	$3.4x10^5$	0.53	190
Tabletop 5	$3.7x10^5$	0.55	180
Tabletop 6	$1.0x10^5$	0.70	140

is clear in Figure 3-7, both the SNLFC fog and Tabletop Fog 5 show a similar bimodal behavior due to the effect of the salt on droplet formation in a stable environment. This type of bimodal fog is referred to as an advection fog and is most often seen in coastal regions [57, 59]. Replicating this type of fog has immediate application to testing optical systems intended for deployment in coastal regions, at sea, and in other areas where the dominant fog is advective in nature.

Figure 3-7 also includes the droplet size distribution of a historical real-world fog from Garland, et al. [57], labelled as "Garland". This fog has a tight unimodal distribution very similar to that seen in **Tabletop Fog 1** from this experiment. This type of diameter distribution classifies these

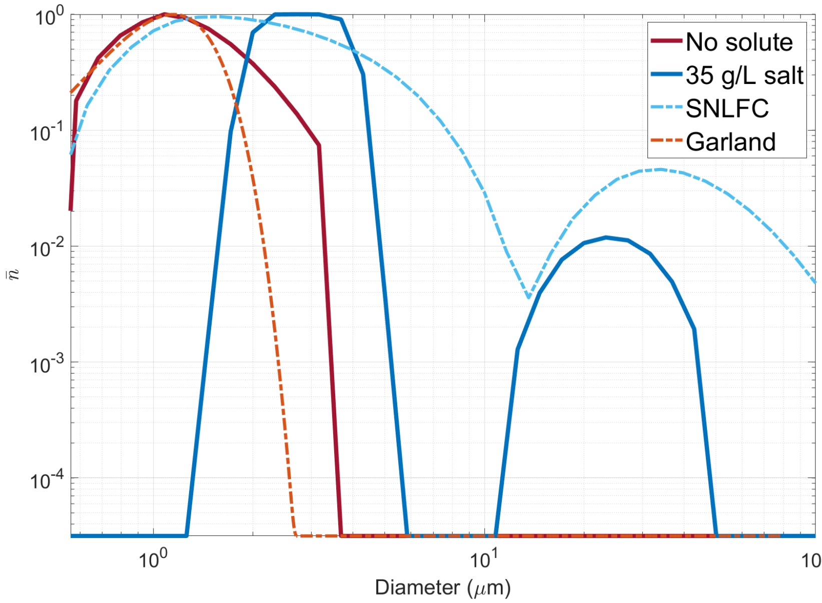

Figure 3-7. Comparison of two experimentally generated fogs (Tabletop Fogs 1 and 5 from this chapter) with a naturally occurring fog (Garland, from [57]) and a previously generated fog-analogue (SNLFC, from [60, 8, 40, 33]) from our large-scale chamber. Similar fog and fog-aerosols share a similar color-scheme for easy comparison. With reds indicating the similarity of the Garland fog and Tabletop Fog 1, and blues indicating the similarity of the SNLFC fog-analogue and Tabletop Fog 5.

fogs as radiation fogs, which are more common inland, where there is less available humidity [57, 59]. Radiation fogs are often less dense than advection fogs, which we can also see if the case when we compare **Tabletop Fogs 1** and **5** in 3-1. There is also immediate relevance to being able to replicate radiative fogs for optical testing of systems that are intended to be deployed at inland facilities. Furthermore, the ability to replicate not just one, but multiple categories of fog is relevant to optical systems that might experience both radiation and advection fogs, such as those present on airplanes and in autonomous vehicles.

Furthermore, we can use the information present in Figure 3-7 to compare the two chambers. This information is useful for informing experiments that wish to scale up or down between the two chambers, where being able to replicate conditions in each chamber will be essential to continuity of testing. By comparing the SNLFC fog to the **Tabletop Fog 5** we can discern that the SNLFC facility maintains a higher RH than the tabletop chamber was able to during these experiments. This can be concluded by observing the larger mean droplet sizes of both modes in the SNLFC fog versus **Tabletop Fog 5** even though **Tabletop Fog 5** had a significantly higher solute concentration. This implies that there is simply more overall water available for nucleation and fog formation in the SNLFC than the Tabletop Fog Chamber. However, the overall similarity between the SNLFC fog and **Tabletop Fog 5** implies that we can expect our experiments in the Tabletop Chamber to scale well to the SNLFC, allowing for support of small and large-scale experimentation.

3.6.4. Generating Fog From Injected Dry Solute Aerosols

While the fog generation technique presented in the preceding sections is able mimic stable real-world fogs, there are some limitations. Because many of the fog droplets exceed their activation diameter when they are initially injected, the methodology lacks control to modulate those droplets to smaller sizes. Even as humidity decreases in the chamber, the supersaturation at the surface of the activated droplets is maintained at a level that promotes stability or even growth. This is in contrast with “haze droplets” decrease in size (“Saddle Point” in Figure 3-2). This provides motivation to generate fog from an initial dry aerosol particle. Enhancements made to the chamber and the microphysical properties of the “seeded” fog are presented in Section 3.6.4.1 and 3.6.4.2.

3.6.4.1. Experimental and Design Enhancements

A TSI 3076 atomizer and diffusional dryer were used in tandem to generate and inject dry aerosol into the MiniFog chamber. The concentration of NaCl in the atomizer solution can also be increased or decreased to achieve a higher or lower aerosol concentration and a larger or smaller aerosol size distribution. A heated bubbler system was implemented by pushing filtered compressed air through a water-filled heated metal canister and was used to humidify the chamber to supersaturation conditions required to achieve droplet activation. The humidified flow introduced into the chamber also enabled the generation of mixing/turbulence. A Julabo recirculating chiller pushed cooled ethylene glycol through a copper cooling coil fashioned to the base to the chamber to provide a minimal about of temperature regulation.

Additional aerosol instrumentation was installed in the chamber to provide diagnostics that are important for characterizing parameters that dictate fog microphysical properties. Temperature, relative humidity, and flow sensors were installed in the humidification line from the bubbler system. To characterize the MiniFog's thermodynamic state, temperature and relative humidity probes were also installed at the top and base of the chamber. Aerosol size distribution and concentration was measured with a TSI NanoScan SMPS, which can size and count aerosols ranging from 10*nm* to 500*nm*.

3.6.4.2. Seeded Fog Microphysical Properties

Figure 3-8 shows and exemplar case during which NaCl aerosols were injected in the chamber at a relative humidity of 89% at 15:05. The humidity was subsequently increased to approximately 93.5% at 15:09 and increased again to 95% at 15:14. Although these modulations in relative humidity are seemingly subtle, they have noticeable implications on the droplet size distributions. During the initial time period (15:05 to 15:09), a low concentration of droplets that are less than 5*μm* in size are detected by the Malvern indicating haze droplet formation or, perhaps, the activation of only the largest NaCl particles injected into the chamber. After the first increase in relative humidity at 15:09, there is a noticeable increase in both the quantity and size of droplets detected. Further, a clear signature of droplet growth from a mean size of approximately 5*μm* (at 15:09) to 7*μm* (at 15 :13) is detected. Following the third increase in relative humidity, a dramatic increase in the concentration and size of droplets indicates that nearly all of the NaCl aerosols present in the chamber have nucleated.

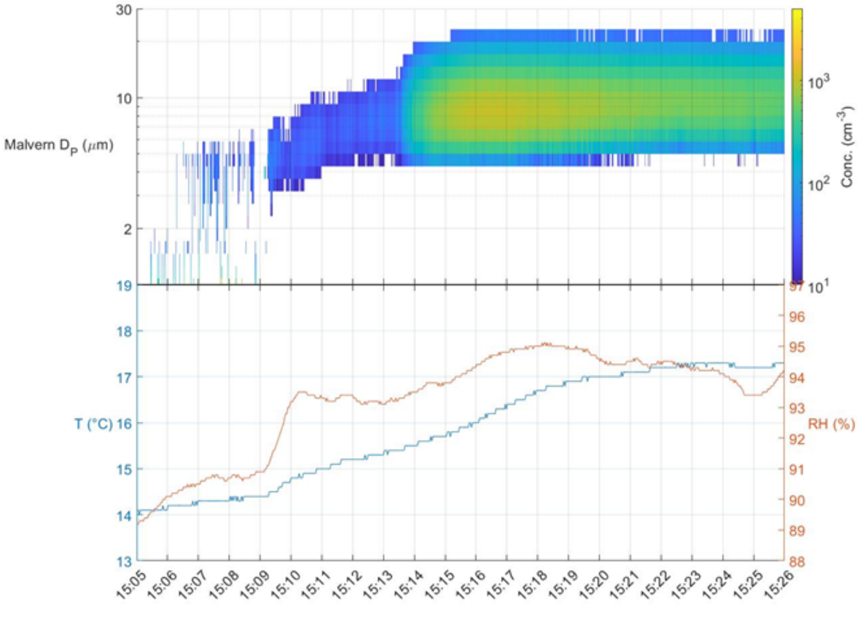

Figure 3-8. Time series of droplet size distribution (top), temperature, and relative humidity (bottom) during a period of incremental relative humidity increases in the MiniFog Chamber after a dry NaCl aerosol injection.

These results demonstrate the advantages of the enhanced fog generation technique, which offers modest control over the relative humidity conditions and droplet growth rate as well as the ability to constrain the maximum droplet diameter.

Results from a separate measurement period are provided in Figure 3-9 during which the relative humidity remained constant at approximately 95% and salt was injected for 50 s (15:27), 40 s (15:40), 30 s (15:50), 20 s (15:58), and 10 s (15:59). Although the peak concentration following the injection of dry aerosols in the chamber decreased accordingly with the duration of the injection, the droplet size distribution does not change much and only subtle decreases in droplet concentration are detected. It's important to note that a secondary period of droplet growth that initiated approximately five minutes after each of the NaCl injections. Further investigation of this phenomena is needed, but we hypothesize that this signature is a result of either relatively slow growth of smaller NaCl aerosols compared to larger ones that produce the initial droplet signature, or delayed nucleation that's facilitated by an excess water vapor imposed by the depletion of larger droplets in the chamber that would otherwise grow at the expense of smaller droplets.

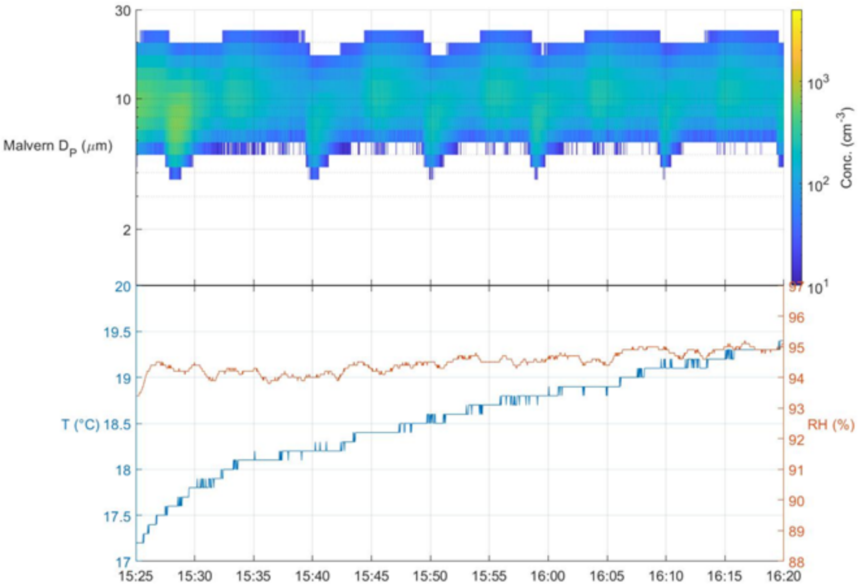

Figure 3-9. Time series of droplet size distribution (top), temperature, and relative humidity (bottom) during a series of NaCl injections with approximately constant relative humidity.

3.7. Summary

In this chapter we have discussed the design, characterization, and applicability of a tabletop fog chamber. We have shown that this tabletop system has significant potential for use as an optics test-bed for fog. We attribute this to the chamber's ability to generate several different fogs with a high level of repeatability, as well as the ease of operation of this chamber, which can be run entirely by a single operator.

3.8. Ongoing & Future Work

Both the "MiniFog" (Section 3.3.1) and "MesoFog" (Section 3.3.2) Tabletop Fog Chambers will be used in support of several ongoing and upcoming projects, as well as available in support of ongoing external customer work.

Under the Pluminate LDRD (LDRD 226083) both the "MiniFog" and "MesoFog" Tabletop Fog Chambers will be used to investigate the effects of various anthropogenic aerosols on the microphysical and optical properties of atmospheric aerosols (fog and clouds). The data from these experiments will be used to inform atmosphere-scale diffusion models, give greater context to albedo-based measurements, and develop a greater understanding of the role atmospheric aerosols play in the environment, all in support of Sandia National Laboratories Climate and Global Security Objectives.

Under a variety of other projects this group intends to utilize these chambers to investigate the scattering regimes of light in degraded visual environments. Much of the current literature is inconsistent on when light is considered to be "weakly", "moderately", and "highly" scattering. By measuring the angle space of scattered light within these chambers we hope to better understand light scattering within degraded visual environments. We further intend to use these chambers to collect data to advance the understanding and utilization of machine learning in degraded visual environments (see Chapter 5 for more detail).

Finally, work performed in these chambers will be presented at the upcoming American Association for Aerosol Research (AAAR) annual conference and the Institute of Electrical and Electronics Engineers (IEEE) Aerospace Conference. Abstracts have also been submitted to present work performed in these chambers at the upcoming International Society for Optics and Photonics (SPIE) Defense and Commercial Sensing (DCS) conference.

3.9. Collaborations

Following initial proving and publication of data regarding the MiniFog chamber [62] this chamber has been utilized on several data collects to support internal and external collaborations.

3.9.1. *Purdue University*

As part of this LDRD an identical chamber to the one described in this chapter was constructed at Purdue University. These twin chambers were initially designed for tandem experimentation and for remote leveraging of Sandia equipment and capabilities. This Purdue-based chamber was utilized for much of the experimental design and initial testing of the work described in Chapter 6 with the Sandia-based chamber and personnel providing anticipated fog optical and microphysical properties for experimentation.

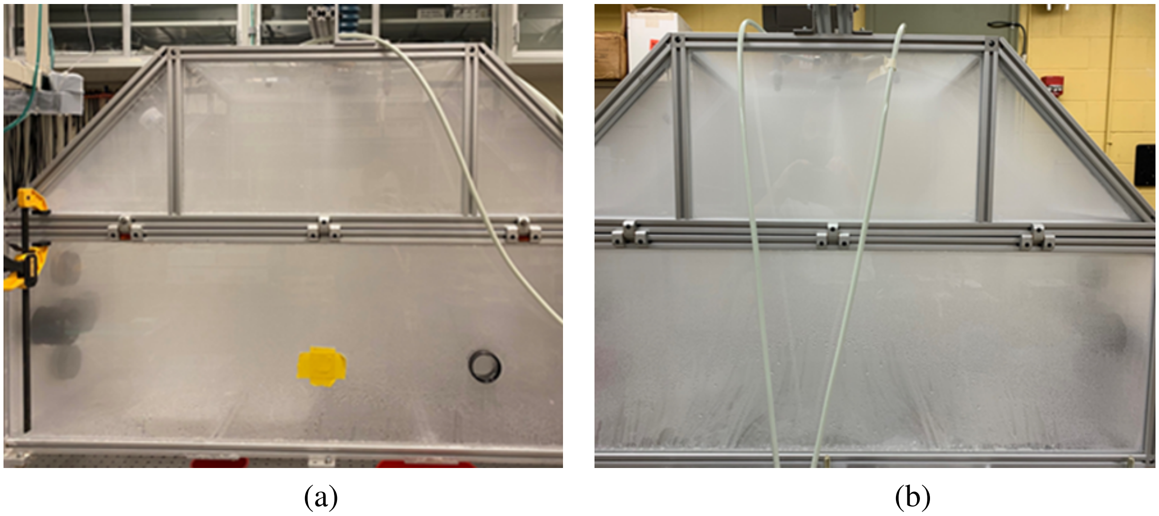
(a) (b)

Figure 3-10. Photographs of the twin Tabletop Fog Chambers generating the same fog, Tabletop Fog 2 from this chapter. (a) The Sandia National Laboratories Tabletop Fog Chamber in Albuquerque, NM. (b) The Purdue University Tabletop Fog Chamber in West Lafayette, IN. On visual inspection, the chambers generate similar fog-analogues when using the same parameter set.

3.9.2. *Internal Collaborations*

3.9.2.1. Event Based Sensing

This chamber was utilized in support of the evaluation of a variety of commercially available event-based sensors (EBS) against degraded visual environments in support of Center 6700 objectives, providing datasets in support of two upcoming LDRDs and one direct customer funded project.

3.9.2.2. FarField Project

This chamber was utilized in collaboration with the FarField customer funded project in Center 6700 to test the propagation of shaped beams through different atmospheric environments. This set of experiments provided data in support of an ongoing direct customer funded project, as well as supporting Center 6700 objectives.

4. INCREASED RANGE AND CONTRAST IN FOG WITH CIRCULARLY POLARIZED IMAGING

4.1. Introduction

Autonomous systems, whether military or commercial, require a suite of optical sensors for guidance and remote sensing that can be rendered inoperable in dense fog conditions. Degraded visual environments pose a serious problem for optical systems as image contrast can be reduced to zero in dense situations. Tens of thousands of people are killed each year in vehicle crashes [67], hundreds of which are attributed to degraded visuals from fog events [68]. The future of human transport is autonomous vehicles, but before they can become a reality the issues of sensing/imaging in highly scattering environments like fog must be addressed. There are several methods currently being investigated to solve the problem of sensing in fog/scattering environments. In this paper, we describe one method which utilizes the polarization characteristics of light to increase imaging range.

Polarized light imaging/sensing in scattering environments has been of interest for many decades. Previous research has encompassed a wide range of scattering environments including: underwater scenes [69, 70, 71, 72, 73, 74, 75, 76, 77], biological tissue or phantoms [78, 79, 80, 81, 82, 83, 84, 85, 86], smoke [74, 87], and fog [88, 89, 90, 91]. We previously presented several polarimetric simulation results that predict increased performance from circularly polarized light in highly scattering environments [92, 93, 94, 95]. Other researchers recently experimentally verified some of these predictions in fog environments at visible wavelengths [90]. In this work, we present contrast and range enhancements with circularly polarized imaging. We describe the design, testing, and analysis of visible and short-wave infrared (SWIR) polarimetric imagers in real fog conditions generated at the Sandia National Laboratories (SNL) Fog Chamber (SNLFC) [60]. The goal of this work is to reveal the imaging performance of active polarimetric systems in highly scattering fog conditions for relevant autonomous vehicle targets, showing circularly polarized imaging increases range and contrast. Here we compare the performance of visible and SWIR systems, as well as linearly and circularly polarized illumination and collection. Our targets of interest throughout this work are commercially available retroreflective road sign and personnel safety materials. This work includes the first experimental analysis of both visible and SWIR polarimetric imaging systems in realistic fog conditions with these materials. The ability to detect and analyze road signs or reflective clothing at enhanced distances through dense fog is crucial for safe operation of autonomous vehicles/systems. The results presented here can also be utilized to design new materials which perform better with autonomous sensing systems [96].

This paper presents the following: background information on polarized light and the SNLFC's scattering environment (Section 4.2), the experimental setup for the visible and SWIR systems and the methods used during fog generation (Section 4.3), results from testing and analysis of imaging in the fog environment, showing circularly polarized imaging increases range in dense fog (Section 4.4), and conclusions and potential future work (Section 4.5).

4.2. Background

4.2.1. *Polarized Light*

The polarization state of light is defined by the Stokes parameters within a 4x1 Stokes vector.

$$\vec{\mathbf{S}} = \begin{bmatrix} S_0 \\ S_1 \\ S_2 \\ S_3 \end{bmatrix} = \begin{bmatrix} \langle E_\parallel E_\parallel^* + E_\perp E_\perp^* \rangle \\ \langle E_\parallel E_\parallel^* - E_\perp E_\perp^* \rangle \\ \langle E_\parallel E_\perp^* + E_\perp E_\parallel^* \rangle \\ i\langle E_\parallel E_\parallel^* - E_\perp E_\parallel^* \rangle \end{bmatrix} \propto \begin{bmatrix} I_H + I_V \\ I_H - I_V \\ I_{45^\circ} - I_{135^\circ} \\ I_{RHC} - I_{LHC} \end{bmatrix} \tag{4.1}$$

The Stokes parameters describe the total light intensity (S_0), what portion of the light is horizontally or vertically linearly polarized (S_1), what portion of the light is linearly polarized at plus or minus 45 degrees (S_2), and what portion of the light is right or left circularly polarized (S_3) [97]. To compare circular and linearly polarized imaging, we measure S_1 and S_3 images with linear and circular polarized active illumination, respectively. This imaging process is also called polarization difference imaging since multiple analyzer state images are subtracted from each other.

In previously published work we have shown the potential for circularly polarized light to maintain its intensity through fog better than linearly polarized light [92, 93, 95]. The performance of circularly polarized light is dependent on the particle size distribution and density of the fog, and the wavelength of interest. Circularly polarized light's increased persistence may increase the signal-to-noise when imaging in highly scattering environments. Circularly polarized light has an increased number of highly polarized photons that transmit through the fog in the intended state, thus getting more light to the target and returned to the sensor in the anticipated states. Additionally, the target characteristics affect the returned intensity of polarized light. For retroreflective films, such as road signs or safety materials, circular polarization can be of increased benefit due to circular polarization's handedness change upon reflection. These targets exhibit higher contrast when performing polarization difference imaging with circular polarization.

4.2.2. *Sandia National Laboratories Fog Chamber*

SNL has a unique fog facility where repeatable fog can be generated on demand [60, 98]. The facility is 55 meters long and roughly 3 meters high and 3 meters wide. Along the length of the facility are 60 spray nozzles that produce fog. The facility is entirely indoors, and Class IV lasers can be safely operated inside. For all fog generation tests a suite of measurement tools are used to characterize the fog. These include a laser diffraction Spraytec particle sizer from Malvern

Instruments, a SNL-built three-band laser transmissometer at wavelengths of 0.543 (in more recent work the wavelength was changed to 0.532), 1.55, and 9.68 μm, and temperature and RH probes placed throughout the facility. With this instrumentation the fog characteristics are logged on a per second sampling rate. Other relevant fog parameters, such as liquid water content, number density, and meteorological range, can be calculated from the data we collect from the measurement suite [99]. The SNLFC is a perfect place to test optical systems in fog since the fog is always characterized. If small changes in the properties of the fog occur from test to test there are robust measurements to determine those variations. This allows for data combination and averaging over many tests to remove outlier test results, which we employ in this work.

4.3. Experimental Setup and Methods

4.3.1. Experimental Setup

Two nearly identical illumination and imaging setups were built for both visible and SWIR polarimetric imaging in fog. The main difference between the two systems are the lasers, optical glass, and detectors used. Whenever possible similar components are used in the setups with only anti-reflection coating differences. A general schematic of the experimental setup for imaging in fog is shown in Figure 4-1. Both experimental setups are built on optical breadboards that are then enclosed in Lexan boxes to protect the optical elements from the harsh fog environments.

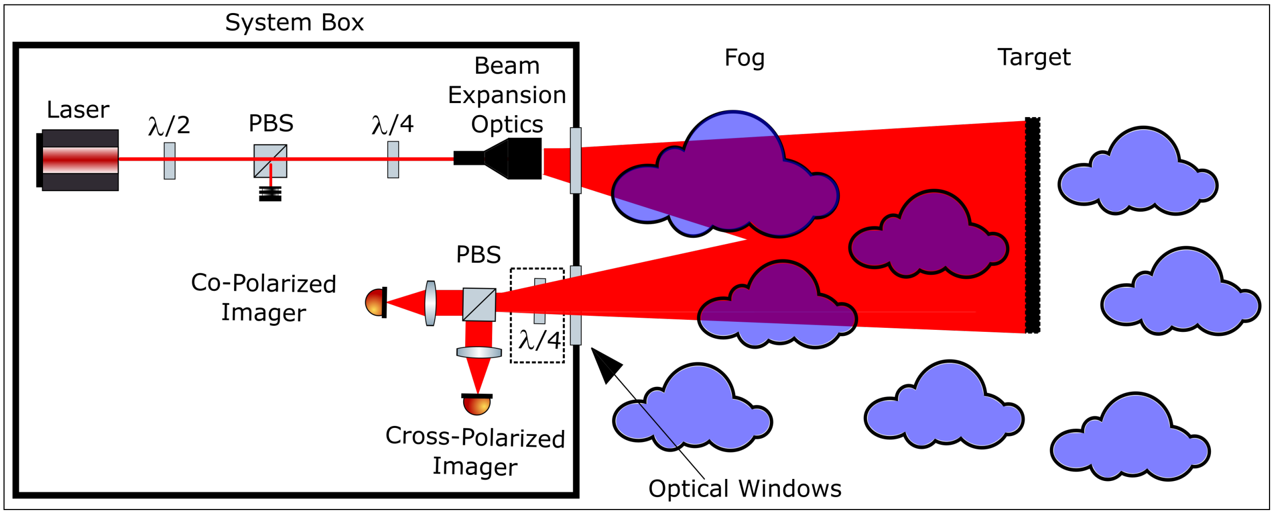

Figure 4-1. Active polarimetric imaging experimental setup for both visible and SWIR fog experiments. Each system has a laser for polarized light illumination of the target in fog (visible - 532 nm, SWIR - 1550 nm). Laser output power is controlled using a half-waveplate ($\lambda/2$) and a fixed polarizer resulting in vertically polarized light output. A quarter-waveplate ($\lambda/4$) is rotated to output vertical linearly polarized light or right circularly polarized light. Illumination optics diverge the beam to illuminate the full target. A multi-camera system collects returned light. Polarized light is collected by the camera system and analyzed by a quarter-waveplate (during circular operations) and a polarizing beam splitter (PBS). The beam splitter sends horizontally polarized light into one channel and vertically polarized light into the other channel (or right circular in one channel and left circular if the quarter-waveplate is present).

Each system has a laser for polarized light illumination of the target in fog. The visible system's laser has a wavelength of 532 nm (Newport EXLSRONE-532-200) and the SWIR system's laser has a wavelength of 1550 nm (Thorlabs FPL1009P). The output power of the laser is controlled using a half-waveplate and a fixed polarizer. Power output is controlled by rotating the highly polarized laser beam's linear polarization output perpendicular to the polarizer axis. The output of the polarizer is vertically polarized light. The laser beam is then sent through a quarter-waveplate to output vertical linearly polarized light or right circularly polarized light. Lastly, a lens or set of lenses diverge the beam to illuminate the full target. During experiments the lenses are optimized to uniformly illuminate each target as best as possible.

The light that transmits to and reflects from the target, and light that scatters from the fog are collected by the multi-camera system. The target is located 7.62 m (25 ft) from the imaging systems. The polarized light collected by the camera system is analyzed by a quarter-waveplate (during circular operations) and a polarizing beam splitter. The beam splitter sends horizontally polarized light into one channel and vertically polarized light into the other channel (or right circular in one channel and left circular if the quarter-waveplate is present). The polarized light is collected by 50 mm focal length f/1.8 lenses (Navitar VIS and SWIR versions). The lenses have the exact same prescription for the visible and SWIR systems except the SWIR optics were coated appropriately for those wavelengths. An image is then captured by either visible or SWIR cameras. The visible camera is a Basler acA2440-75um with 2448x2048 pixels and the SWIR camera is a FLIR TauSWIR with 640x512 pixels. The SWIR imager can collect data at a faster rate than the higher resolution visible imager due to data link limitations. This led to a slightly different frame rate between the imagers. The average frame rate for the visible system is 1 Hz and for the SWIR system is 0.5 Hz.

The goal of the imaging system is to capture S_1 and S_3 polarized Stokes component images. Thus, the horizontal and vertical channel, or right and left circular channel, images are subtracted from each other. Since the images are subtracted, care is taken to properly align the cameras with respect to each other. A perfect alignment was not feasible mechanically. Thus, the camera systems were calibrated with the resolution targets shown in Fig. 4-2. A post-process image registration algorithm is performed to produce image shift error less than 0.5 pixel in magnitude [100]. This resulted in nearly zero image alignment and subtraction artifacts.

4.3.2. Target

Multiple targets are used throughout our experiments. These targets are adhered to a large piece of aluminum. In total five different reflective material targets are investigated. Each individual material target has a precision USAF 1951 resolution target printed on it. The targets are shown and labeled in Figure 4-2. Target 1 is a prismatic retroreflective material with linear patterning, Targets 2 and 3 are prismatic retroreflective material with diamond patterning, Targets 4 and 5 are glass microsphere retroreflective materials. The USAF 1951 bar charts were laser printed onto the films with fine spatial frequencies beyond the limits of the two imaging system's resolution capabilities. These targets encompass a range of reflective film types and compositions relevant for street/road signs and safety/emergency retroreflective materials.

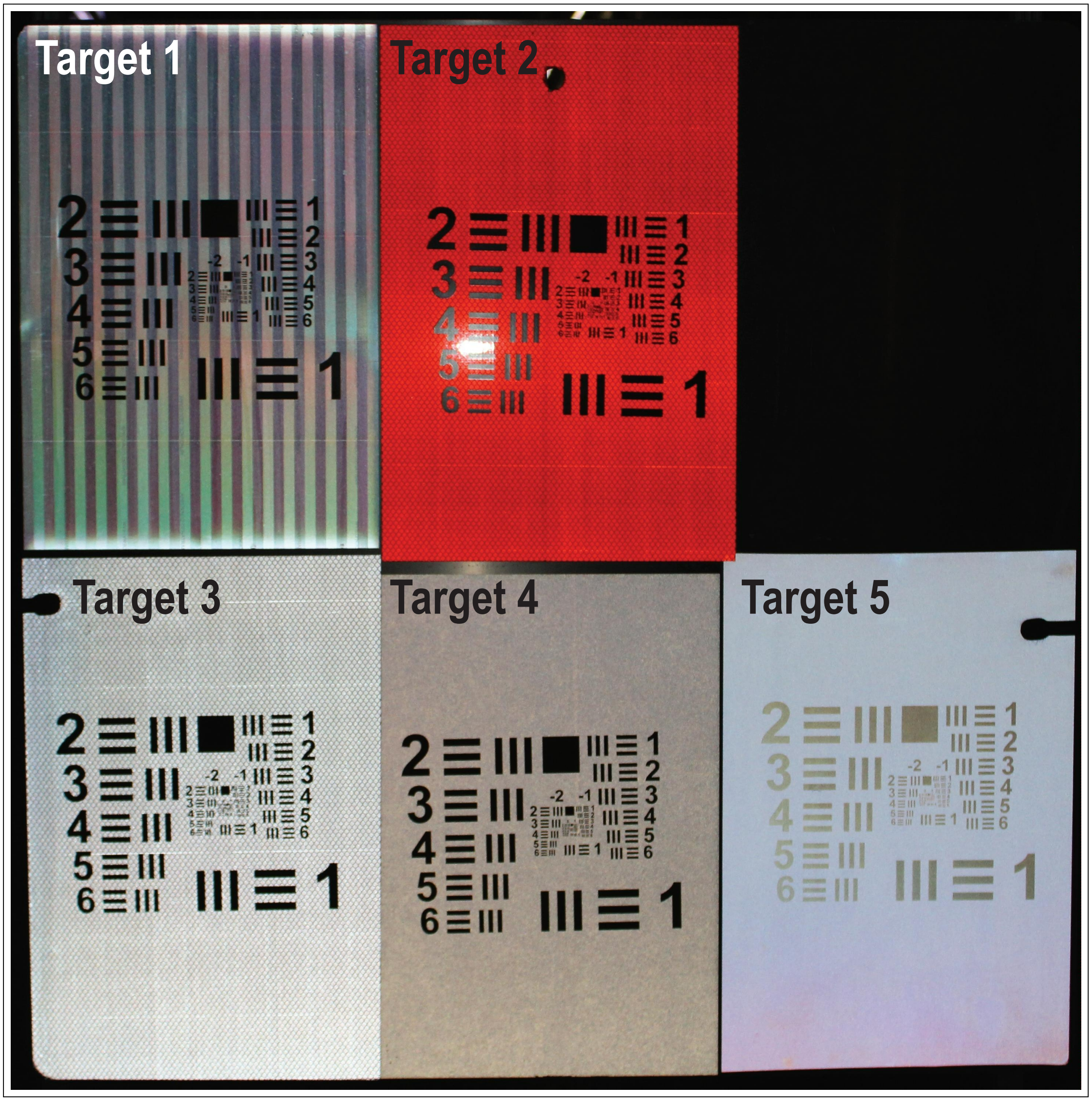

Figure 4-2. Visible color digital camera image of multiple USAF 1951 targets made up of different commercially available retroreflective films. Target 1 is a prismatic retroreflective material with linear patterning, Targets 2 and 3 are prismatic retroreflective material with diamond patterning, Targets 4 and 5 are glass microsphere retroreflective materials.

4.3.3. Experimental Methods

Throughout all experiments the visible and SWIR imaging systems are tested side-by-side in varied fog environments. Each polarization configuration is tested separately, i.e., the visible and SWIR systems were set to linear polarized illumination and linear polarized image capture for a single test then the experiment is repeated with circular polarized illumination and image capture. Several fog generations were performed over multiple days. At the SNLFC we utilize salt as a way to help coarsen/enlarge the fog particle sizes [60]. In general, we use a mixture of 10 g/L of salt in the water that is mechanically sprayed into the facility. Other salt mixtures have been tested and characterized in prior fog testing. All the fog generated during the experiments presented here is formed from a 10 g/L saltwater mixture. Representative fog particle size and transmission data can be found in previous publications [98]. Each fog generation consists of spraying fog into the facility until max density is achieved, typically taking 10 to 20 minutes of spray time. After the spray is stopped the transmission through the fog is tracked until it reaches 15 percent transmission over a 20 ft path. We then repeat this process of fog pulse generation many times in a day. We do this because each fog run may have slightly different characteristics as the conditions in the facility change. This is also why we exhaustively characterize the fog throughout the experiments on a per second time interval. Between each fog pulse the reflective targets are cleaned and dried to remove any water or salt that has condensed onto the targets. After three fog pulses the polarization configurations are changed to the other polarization states and the fog procedure is repeated. In total, 6 fog pulse experiments are performed for each polarization state per day. Imagery data collected during the turbulent spray periods and cleaning periods is removed from the data.

Contrast is calculated from each collected polarization difference image. For the visible system, 18 total spatial frequencies were examined for each target in 4-2, corresponding to the largest 3 sets of 6 horizontal and vertical bars. For the SWIR system, 12 total spatial frequencies were examined due to the decreased overall resolution of that system. The contrast for both horizontal and vertical bars is calculated for each frequency for both systems using the Michelson contrast equation [101],

$$\frac{I_{max} - I_{min}}{I_{max} + I_{min}} \tag{4.2}$$

where I_{max} and I_{min} are the max and min intensity values of the averaged pixel columns or rows over the vertical or horizontal resolution bars and the spaces between the bars. These contrast values associated with the corresponding target spatial frequencies defines a contrast transfer function (CTF), contrast versus spatial frequency [102]. Ultimately, each temporal frame is processed for the CTF curves for both vertical and horizontal resolution bars. To compare spectral and polarization performance differences on a level playing field, the CTF curves are integrated across spatial frequencies to give an overall CTF area under the curve (AUC). By taking the CTF AUC we can use one value for each time stamp/fog characteristic and imaging configuration. The AUC values are all normalized by the maximum AUC value calculated for each individual target. This typically normalizes the AUC curves by the contrast when no fog is present during calibration image collection.

To quantitatively compare the performance of linear and circular polarized imagers a standard distance/range metric must be used. Here, we will follow a similar analysis as that in Redman, et al. [99]. Many other researchers use visibility as a metric, but the colloquial visibility leads to ambiguity. Visibility can be a qualitative human-specific measure and/or a quantitative value that is a measure of extinction when using the Koschmieder equation. Even the use of the Koschmieder equation can lead to challenges/confusion [103]. In this paper we will compare imaging contrast results against equivalent distance/range for the International Civil Aviation Organization (ICAO) Category IIIc "thick fog" landing specifications. The ICAO specification for visual range in Cat. IIIc conditions is 92 m [104].

Using the experimentally collected transmissometer data, the meteorological optical range (MOR) can be calculated from the Beer-Lambert Law and MOR's 5% flux reduction definition [105],

$$\Phi = \Phi_0 e^{-\beta L} \tag{4.3}$$

$$MOR = \frac{-ln(0.05)}{\beta} \tag{4.4}$$

where β and L are the extinction coefficient of the fog and the path length in the fog, respectively. The target distance is fixed throughout the experiments (25 ft or 7.62 m) so β is calculated as,

$$\beta = -ln(\frac{\Phi}{\Phi_0})\frac{1}{L}. \tag{4.5}$$

Using this, MOR can be modified for the specific wavelength of the transmissometer (543 nm),

$$MOR_{543} = L_{trans}\frac{ln(0.05)}{ln(\frac{\Phi}{\Phi_0})} \tag{4.6}$$

where MOR_{543} is the meteorological optical range equivalent in meters, L_{trans} is the distance between the source and the detector of the transmissometer, Φ is the flux on the detector, and Φ_0 is the initial flux with no scattering environment present.

The SNLFC can generate fog densities that are not typically measured in natural fogs. These fog densities can approximate longer ranges than the facility allows. To scale the overall distance the combination of optical thickness and MOR is needed. The optical thickness, OT, of a scattering environment is defined as a unitless quantity [106],

$$OT = \rho\sigma L, \tag{4.7}$$

where ρ is the density of the scattering particles, σ is the extinction cross-section of the scattering particle mixture, and L is the optical path length. The optical thickness can be defined as follows for a target and imager configuration,

$$OT = -ln(\frac{\Phi}{\Phi_0})\frac{L_{target}}{L_{trans}}, \tag{4.8}$$

where L_{target} is the distance from the imager to the target and L_{trans} is the distance between the send and receive ends of a transmissometer. Combining this equation, (4.8), with the modified MOR equation, (4.6), an optical thickness-based MOR can be defined as,

$$MOR = \frac{-ln(0.05)}{OT}L_{target}. \tag{4.9}$$

From this equation, (4.9), and the modified MOR equation, (4.6), an equivalent range/distance at a defined MOR value can be calculated,

$$L_{equivalent} = \frac{MOR_{equivalent}}{MOR_{measurement}} L_{measurement}. \tag{4.10}$$

For all results presented in this paper, we use an equivalent MOR of 92 meters to calculate equivalent ranges. The ICAO's densest fog category, Cat. IIIc, is defined for when MOR is equal to or less than 92 m. Thus, our imaging contrast results are compared to equivalent distance/range in an ICAO Cat. IIIc fog with the same attenuation. Using the equations above it is trivial to convert from equivalent range to optical thickness if that is desired.

Before describing the experimental results, further details on the range scaling should be discussed. The following presented results compare imaging contrast between active circular and linear polarized imaging systems. Scaling the range to those equivalently found in nature/a Cat. IIIc fog is useful for the broader community when thinking about polarized system utility in an autonomous vehicle or other remote sensing systems. When the range is scaled, the size of the resolution targets and field of view (FOV) of the optical systems would also need to be scaled appropriately. We normalize the CTF AUC curves to remove the specifics of the resolution bars and focus on the differences between the two polarization states. In a deployed imaging system care would be needed when designing the FOV and target resolution requirements. We do not consider those specific requirements here but merely present and discuss the advantage of circularly polarized imagers to penetrate deeper into dense fog conditions compared to linearly polarized imagers.

4.4. Experimental Results

To date there has been limited quantitative examination of circular polarized imaging's range and contrast enhancement in fully characterized fog environments; and no results showing contrast variations in both the SWIR and visible spectrums for the same materials. Figure 4-3 and Figure 4-4 show CTF AUC results for the five targets with circular and linear polarized imaging at visible and SWIR wavelengths, respectively. Circular polarized imaging contrast is shown in red and linear polarized imaging contrast is shown in black. Horizontal bar target CTF AUC values are shown with solid lines and vertical bar target CTF values are shown with dotted lines. Each target's plot includes a zoomed inset showing results for the largest distances/densest fogs.

4.4.1. Visible Imaging Results

Each target in Figure 4-2 has unique reflection properties which create different contrast variation. Figure 4-3 shows the CTF AUC results for each of the five targets across the entire range of fog densities/distances with the visible illumination and imaging system. Figure 4-3 compares both circular and linear polarized imaging's performance for both resolution orientations, horizontal and vertical bars. In general, circular polarized imaging has larger contrast whether with fog or without when imaging the retroreflective target materials. Circular polarization's handedness change upon reflection from these target materials causes this increased contrast when imaging the black resolution bars, while linear polarization remains in the same vertically polarized state upon reflection. Thus, for most of the targets the circular CTF AUC values for each target are larger than that of linear polarization even at lower fog densities, in some cases 2-3x higher contrast. This is less the case in Targets 2 and 3. Similarly, horizontal and vertical resolution bars exhibit the same contrast for all targets except Targets 2 and 3. For those targets, vertical resolution bars have higher contrast when imaging with circular polarization. These two target materials are prismatic retroreflectors with diamond patterning which may cause this increase in vertical bar contrast at lower fog densities. Target 2's visible results are unique due to the color of the material. Since our visible illumination is at a green wavelength (532 nm), the orange target has orders of magnitude less reflected light compared to the other targets. With such low reflected/collected light from that target the normalized AUC values look abnormal; the values don't go to zero with very dense fog. These results have very low signal-to-noise. We include the results for Target 2 because they show polarized imaging performance is dependent on a number of factors which includes the target characteristics. Care should be taken when viewing these results due to the low reflectivity of Target 2's material at the active illumination's visible wavelength. Circularly polarized imaging has a lower contrast difference than linearly polarized imaging for Target 3, compared to the other targets. Although it has the lowest contrast difference for any of the targets, its contrast is still comparable to the contrast when imaging with linearly polarized light for the same target. Where circularly polarized imaging really excels is at large equivalent ranges/the densest fog situations. Beyond an equivalent Cat. IIIc distance of 175 m linearly polarized imaging loses all contrast. Meanwhile, circularly polarized imaging maintains contrast until an equivalent range of roughly 190 m. These equivalent distances correspond to optical thicknesses of roughly 5.7 and 6.2, respectfully. As we have shown in previous simulation results, circularly polarized light maintains its intended polarization state longer in highly scattering environments compared to linearly polarized light. These experimental results show the polarization memory effect of circular polarization can increase sensing range in realistic fog environments compared to linearly polarized light. In each of the target plots in Figure 4-3 there are inset figures with zoomed in results for ranges from 165 to 200 m. These inset plots show the same data as the larger plots but better illustrate circular polarized imaging's increased contrast at the largest ranges/densest fogs. For these reflective road sign and safety material targets, and 532 nm active polarimetric imaging, circular polarized imaging increases range and contrast in dense realistic fog conditions.

4.4.2. Short-Wave Infrared Imaging Results

SWIR polarimetric imaging exhibits both differences and similarities to the visible case. Figure 4-4 shows the CTF AUC results for each of the five targets across the entire range of fog densities/distances with the SWIR illumination and imaging system. Like the visible experimental results, Figure 4-4 also compares both circular and linear polarized imaging's performance for both resolution orientations, horizontal and vertical bars, but for the SWIR wavelength. Targets 1, 4, and 5 show circular polarized imaging has higher contrast for shorter ranges/lower densities in fog which is similar to the visible experiments. Linear polarized imaging has higher contrast at similar ranges for Targets 2 and 3 which differs from the visible

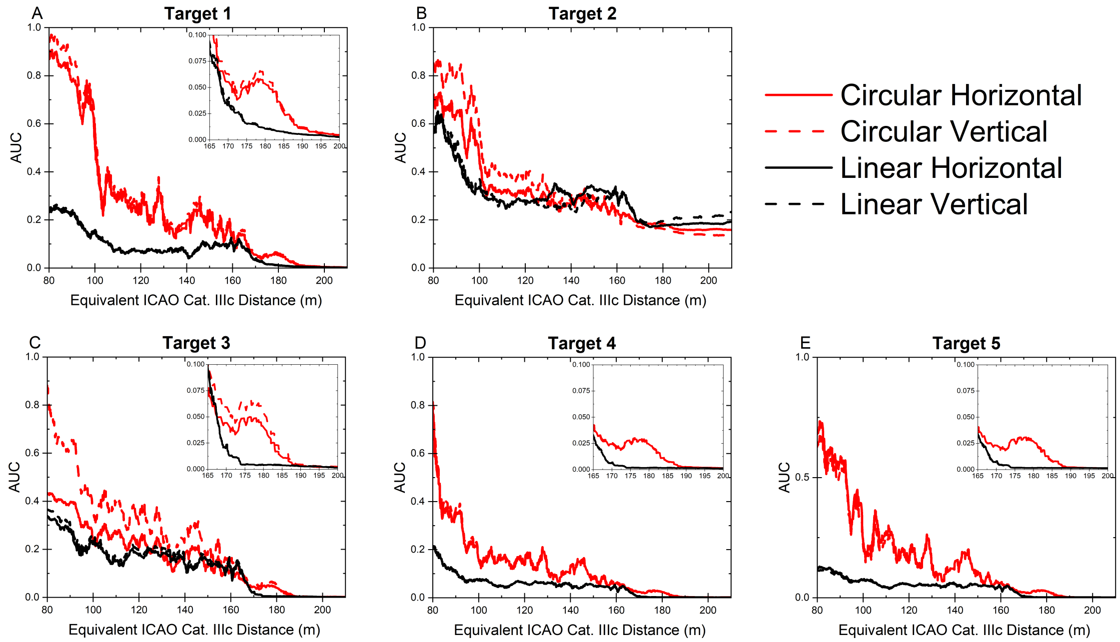

Figure 4-3. Visible CTF AUC results for each target and polarization vs ICAO Cat. IIIc heavy fog equivalent distance/range: A) Target 1, B) Target 2, C) Target 3, D) Target 4, E) Target 5. Circular polarized imaging contrast is shown in red and linear polarized imaging contrast is shown in black. Horizontal bar target CTF AUC values are shown with solid lines and vertical bar target CTF values are shown with dotted lines. Each target's plot includes a zoomed inset showing results for the largest distances/densest fogs.

experiments. Target 2 has similar reflected intensity levels as the other targets in the SWIR. The orange film color is not an issue at SWIR wavelengths compared to the visible illumination wavelength. As in the visible, circular polarization outperforms linear polarization at the largest ranges/densest fog for most targets. For all targets except Target 2, circular polarized imaging maintains contrast at the longest ranges better than linear polarized imaging. Generally, linear polarized imaging loses all contrast by an equivalent range of 170-180 m, optical thicknesses of 5.5 and 5.8, depending on the target. Circular polarized imaging maintains contrast until an equivalent range of 185 or 190 m, optical thicknesses of 6.0 or 6.2. This is not the case for Target 2 where linear polarized imaging modestly outperforms circular polarized imaging at the largest ranges/densities. For these reflective road sign and safety material targets, and 1550 nm active polarimetric imaging, circular polarized light increases range and contrast in dense realistic fog conditions for Targets 1, 4, and 5 but not for Targets 2 and 3. Targets 2 and 3 are made of the same materials but a different visible color. At the SWIR wavelength, linearly polarized imaging is ideal for these materials. Linear polarized imaging also performed better in lighter fog conditions for the two diamond pattern materials. Figure 4-4, like the Figure 4-3, shows inset figures for each Target with zoomed in results for ranges from 165 to 200 m, or for Target 2 ranges from 180 to 210 m. These inset plots show the same data as the larger plots but better illustrate circular or linear polarized imaging's increased contrast at the largest ranges/densest fogs.

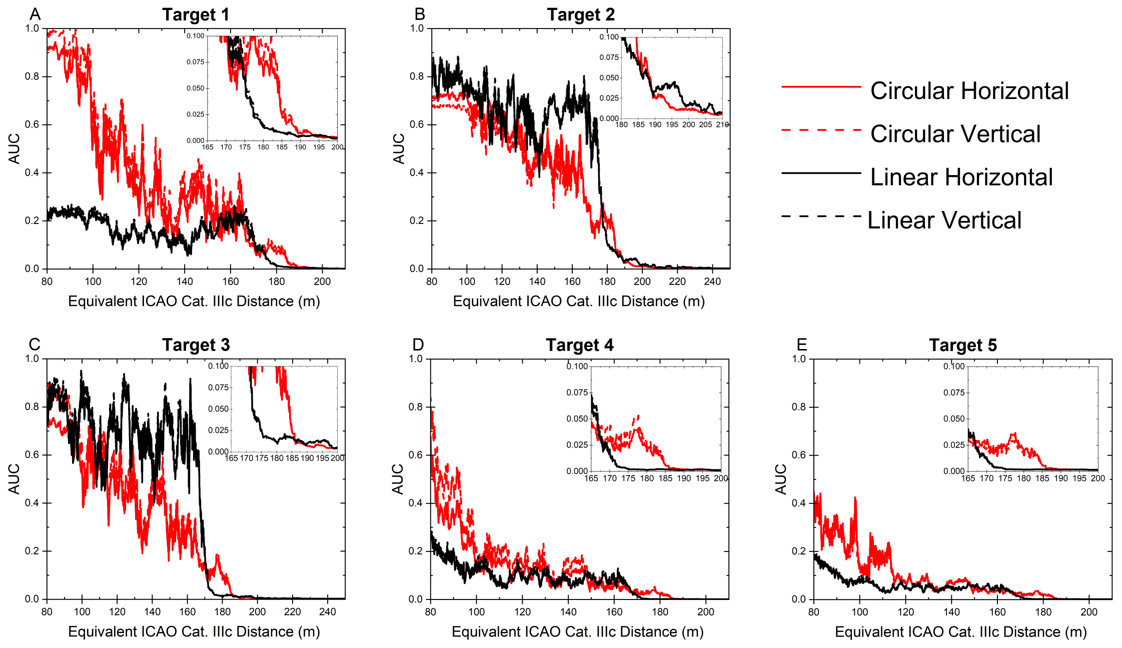

Figure 4-4. SWIR CTF AUC results for each target and polarization vs ICAO Cat. IIIc heavy fog equivalent distance/range: A) Target 1, B) Target 2, C) Target 3, D) Target 4, E) Target 5. Circular polarized imaging contrast is shown in red and linear polarized imaging contrast is shown in black. Horizontal bar target CTF AUC values are shown with solid lines and vertical bar target CTF values are shown with dotted lines. Each target's plot includes a zoomed inset showing results for the largest distances/densest fogs.

4.5. Conclusions

Fogs, low lying clouds, and other highly scattering environments pose a challenge for many commercial and national security sensing systems. Current autonomous systems rely on optical sensors for navigation whose performance is degraded by highly scattering environments. Our previously published work has shown circular polarization maintains its polarization state through higher numbers of scattering events compared to linear polarization. The ability to maintain the intended polarization state can allow circular polarization to perform better in imaging and sensing scenarios within highly scattering environments like fog. In this work, we experimentally show that active circularly polarized imaging can increase contrast and range in highly scattering realistic fog conditions compared to linearly polarized imaging. We present imaging contrast results for retroreflective road sign and safety materials with polarimetric imaging systems working at both visible and SWIR wavelengths. Contrast from the following five target materials with USAF 1951 resolution patterns printed on them is described: 1) grey colored prismatic retroreflective material with linear patterning (road sign material), 2) orange colored prismatic retroreflective material with diamond patterning (road sign material), 3) grey colored prismatic retroreflective material with diamond patterning (road sign material), 4) grey glass microsphere retroreflective material (road sign or safety material), 5) grey glass microsphere retroreflective material (safety material). For the experimental visible wavelength (532 nm), circular polarized imaging has enhanced contrast, in some cases 2-3x compared to linear polarized imaging, at nearly all ranges for all the reflective materials; other than the orange material (Target 2) that is not reflective at the illumination wavelength. The circular polarized imaging system images deeper into fog compared to linearly polarized light, in most cases 15-20 meters deeper. SWIR circularly polarized imaging shows similar results as those observed in the visible for some target materials (Targets 1, 4, and 5) but worse performance compared to linear polarized imaging for two of the target materials (Targets 2 and 3). Upwards of 15 meters deeper imaging with circular polarization in the SWIR is also observed, even for one of the materials where linearly polarized light has higher contrast at lower fog densities (Target 3). Linearly polarized imaging penetrates deeper than circularly polarized imaging only for Target 2 with SWIR illumination. This target has a unique visible color compared to all the other reflective targets which makes it somewhat of an outlier. The results for Target 2 are valuable as they show polarized imaging performance is dependent on a number of factors which includes the target characteristics, such as color and reflectivity at the imaging system wavelengths. Overall, circularly polarized active imaging has higher contrast and can image deeper into fog when imaging reflective targets, both at visible and SWIR wavelengths. These results show that active polarimetric imaging can be a useful tool for autonomous vehicles and remote sensing in highly scattering environments such as fog. Many areas of future work in this area are needed. This includes more exhaustive examination of different material types and target types; non-retroreflective targets, structured targets, human model targets, etc. This work focuses on retroreflective targets but other target types could show benefits for either circular or linear polarized imaging. Additionally, we have presented results for two specific wavelengths in the visible and SWIR. Future work comparing circular and linear polarized imaging across a broad sweep of wavelengths is needed. Lastly, we present active polarimetric imaging results but we have not examined the ever growing area of active laser detection and ranging (LADAR). Work needs to be explored to compare our results with a large illumination beam vs. the small laser profiles used for LADAR applications.

5. MACHINE LEARNING DENOISING MODEL

5.1. Introduction

We have demonstrated that computational imaging is able to image deeper into aerosols by accounting for scattered information in a weak angular light transport approximation. However, challenges persist, primarily that deployment is limited to controlled settings and the high computational cost limits practical utility for real time assessments. In this chapter we describe efforts to overcome these limitations by adapting our computational approach with machine learning (ML). We sought to leverage data-driven methods in the form of ML to gain computational efficiency since the computational cost of ML comes primarily in training the model and relatively no cost arises in forward predictions. The data-driven method is also not limited by physical assumptions rather, it finds representation in information rich data. The ML approach is readily adapted to varying settings by gathering sufficiently diverse setting representations within the training dataset that generalizes the model to desired conditions. However, careful consideration and formulation must be undertaken to achieve the same performance as our computational imaging approach.

The remaining sections of this chapter present our initial attempt to develop an ML model using a previously gathered dataset via a denoising autoencoder approach. Our findings suggested the ML model developed a bias to our expected output which stems from a lack of diversity in the training examples. This lack of diversity leads to memorization by the ML model. This finding led to efforts to gather a dataset with the intention of using it for supervised ML. Details regarding the gathered dataset is presented in the second section of this chapter. The final section presents future steps that can be taken to further the state-of-the-art of our computational imagining capabilities.

5.2. Denoising Autoencoder

Preliminary work sought to leverage previously gathered experimental longwave images in the fog tunnel facility to explore the capabilities of ML for imaging in fog. The general approach treated fog's scattering effect as noise in images and the task of the ML models was to denoise the images. Two approaches were investigated, a direct and indirect approach. The first approach aimed to estimate the denoised images directly. The second approach aimed to estimate the residual portion of the image (the degrading portion) to then subtract from the noisy image resulting in a denoised image. Both approaches utilized the same autoencoder denoising ML architecture which has been used in literature to process noisy images. Autoencoders are comprised of two main components, an encoder and a decoder. The encoder component takes a given input and reduces it to its key features in a dimensionality reduction process. The decoder component then reconstructs the key features to form the expected output which is the original image in approach 1 and the residual portion of the image in approach 2. Depending on the learning objective, the encoding section of the neural network can be thought of as learning how to keep the important features of the image while discarding the rest. The decoding section learns how to reconstruct the expected output from the key features.

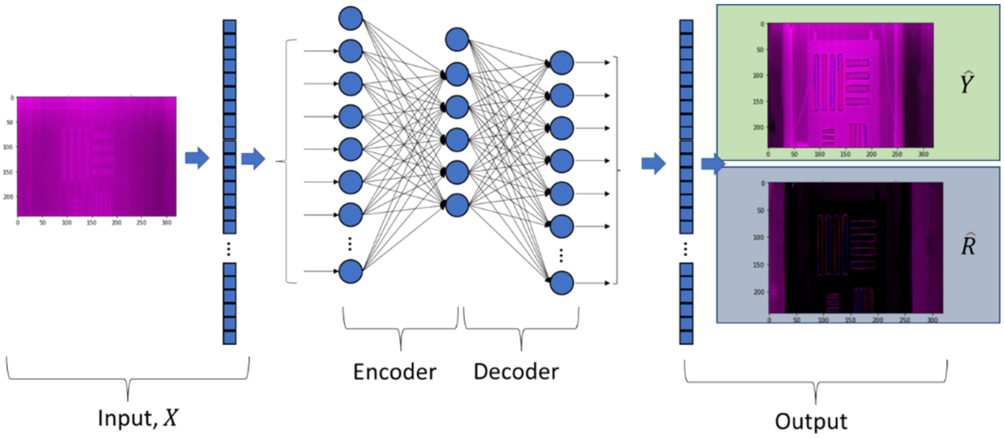

Figure 5-1. Autoencoder schematic.

The available dataset consists of longwave images that were taken in series in the fog tunnel. A total of 682 images constituted the entire dataset, with each image gradually increasing in degradation as the density of the fog present in the image increases. The first image is used as the true image, Y. It is assumed that all other images are degraded and should resemble the first image after denoising. The residual portion of an image, R, is obtained by subtracting the expected image, Y, from the foggy image, X

$$R = X - Y. \tag{5.1}$$

Thus, the objective of the first approach is to directly estimate the true image. The learning objective is as follows.

Approach #1

$Optimize[f_1(X)] = \hat{Y}$
-minimizing $MSE(Y, \hat{Y})$
$f_1(X) = \hat{Y}$

The goal is $[Optimize f_1(X)] = \hat{Y}$, by tuning function parameters to minimizing mean square error $MSE(Y, \hat{Y})$. The objective of the second approach is to estimate the residual portion of the image, R, to then subtract from the foggy image, X, to finally obtain a denoised image estimate, $\hat{Y}$.

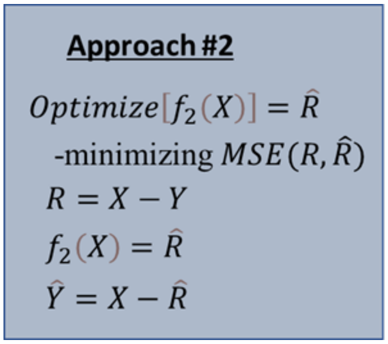

Approach #2

$Optimize[f_2(X)] = \hat{R}$

-minimizing $MSE(R, \hat{R})$

$R = X - Y$

$f_2(X) = \hat{R}$

$\hat{Y} = X - \hat{R}$

The goal is $Optimize[f_R(X)] = \hat{R}$, by tuning function parameters to minimizing error $MSE(R, \hat{R})$. The estimated denoised image is then

$$\hat{Y} = X - \hat{R}. \tag{5.2}$$

Approach 1 of estimating the clear image directly resulted in the ML model memorizing the expected output as shown in Figure 5-2, Approach 1 section. Regardless of the input, an exact replica of the expected output is produced as seen by the memorization check. A memorization check was performed by providing a randomly generated noise image, $X_{garbage}$, as the input to see if there lies a bias in the output of the model. Approach 1 reproduces the exact expected output even though there is no useful information from the provided input, suggesting that regardless of what is being analyzed the same output will be provided. This memorization is undesirable since the ML model is not learning the intended functionality of denoising but is rather overfitting to the training conditions. Approach 2 attempts to limit the memorization of the ML model by adding increased variability in the training dataset. The residual portion of the fog images varies from example to example, which helps mitigate memorization to an extent but a bias to the constant scenery is still overserved by the memorization check in Figure 5-2 Approach 2 section. Even though there is no helpful information provided by the input, $X_{garbage}$, the estimated residual output of approach 2 has some resemblance to the setting of the expected output. This resemblance suggests overfitting, or bias is still prevalent in approach 2, though it is not as severe as approach 1.

The overfitting of approaches 1 and 2 largely stem from the lack of variability in the dataset. A large portion of the dataset has little presence of fog. As a result, there is little representation within the collective examples of conditions that would help the ML models learn the desired computation. Differences between the true image (0th image) and the remaining images are not significant until after around the 500th image. This is reflected in the error plot of Figure 5-3 comparing the 0th image to the nth image.

It became clear to us that a well labeled dataset with diverse settings for supervised ML was required to truly gauge the capabilities of ML in imaging in fog conditions. Thoughts were also placed in gathering data that would allow us to leverage gains in computational imaging approaches in the learning process of ML to better generalize its estimates and avoid overfitting as seen in approaches 1 and 2. This is discussed further in the next section of this chapter.

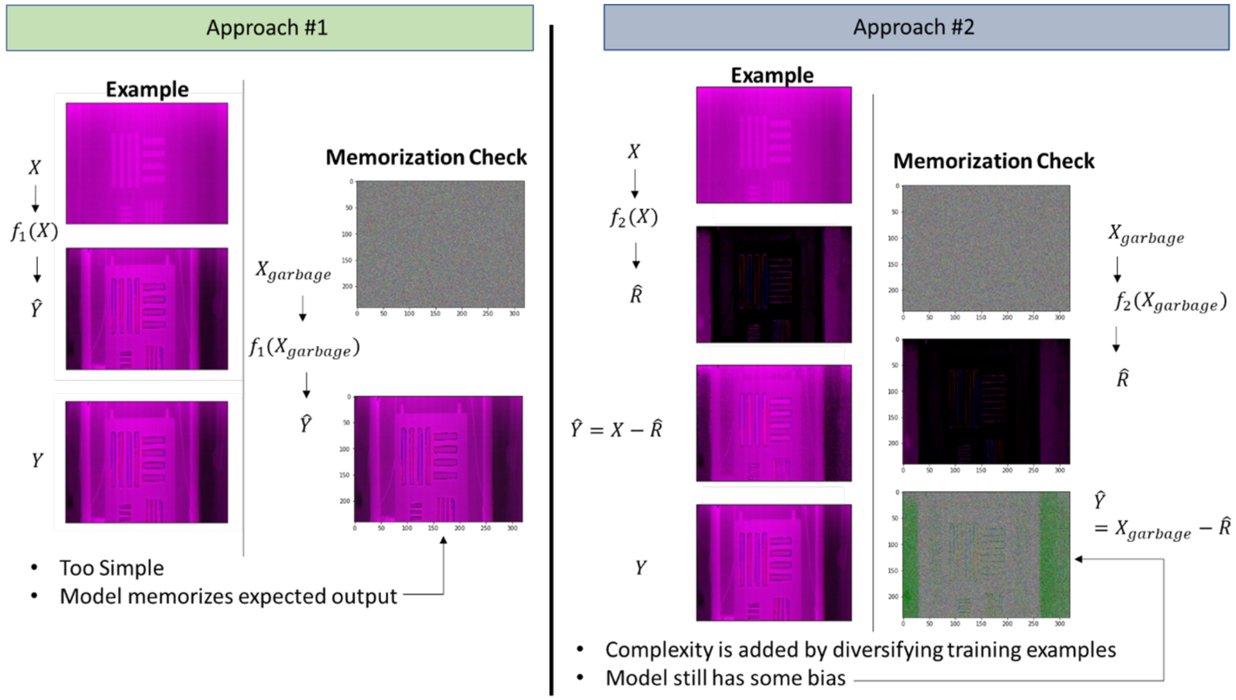

Figure 5-2. Results of denoising autoencoder by approach.

5.3. Well Labeled Dataset for ML

The ML intended dataset was collected using the mini fog chamber and a visual PixeLink camera. Targets were displayed on a monitor at the other end of the chamber from the visual camera's location. The targets displayed on the monitor are also the light source. A schematic of the experimental setup is provided in Figure 5-4.

During runs, the fog density was varied from a stable 2 percent transmission (SWIR) to the lowest transmission levels possible as reflected in Figure 5-5. The range in transmission was decided upon based on observation where apparent signals were received at around 2 percent transmission. It is important to reach the conditions where signal cannot be distinguished from noise. This way we can really test the capabilities of the ML approach to failure. Thus, we assure nontrivial examples were collected by setting the visibly identifiable transmission percentage as our upper bound. In addition to the transmission percentage data, we deployed a particle sizer to provide fog particle size distribution as a function of time via the Malvern system. Having well characterized fog conditions that vary over time will also allow us to relate the ML model's denoising capabilities to fog conditions.

The experimental runs consisted of two phases, pre-treating the chamber and test sprays. The pre-treatment of the chamber raised the relative humidity of the chamber to 80 percent or greater. An initial mechanical humidification spray then follows to reach supersaturation conditions. After completing the chamber pre-treatment test sprays were conducted. The test sprays began by repeating mechanical sprays that bottomed out SWIR transmission (about 0.2 percent transmission) and stabilized at around 2 percent transmission. Once the 2 percent transmission

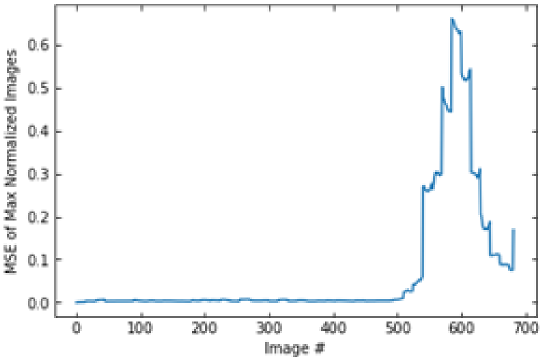

Figure 5-3. Mean squared error quantified variability of training examples.

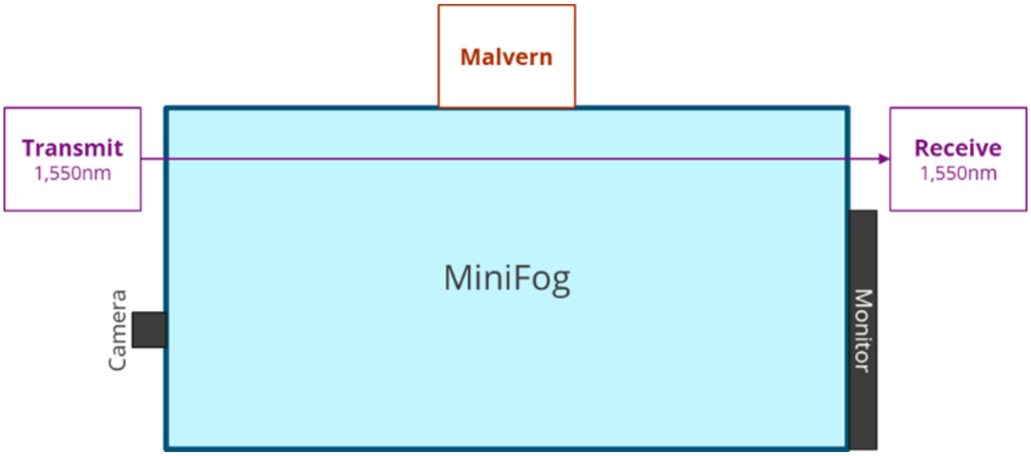

Figure 5-4. Schematic of experimental setup for ML data gathering.

stabilized as the upper bound of SWIR transmission, we began to collect data for the ML test with corresponding characterized fog conditions. The ML tests consist of three main testing conditions, a baseline condition where no fog is present, a fog only condition where fog is present in the chamber, and a fog + solar pedestal condition where a lamp is turned on overhead of the chamber to simulate atmospheric light in addition to the generation of fog. For each test condition two types of tests were conducted. The first type of test was runs that aimed to measure point spread function (PSF). The PSF runs aim to empirically measure the degrading effect of fog as a point spread function. Point source lights are emitted on the monitor by lighting up a single monitor pixel at varying monitor spatial locations. We can empirically measure how fog effects the points source at the camera as a function of location along the monitor's plane. The second type of test consist of MNIST handwritten digits comprising the target dataset. The MNIST handwritten digits dataset is an opensource dataset that has been widely used form ML purposes. The dataset has 70,000 unique examples of handwritten numbers that range from 0-9. The large number of unique examples will help prevent overfitting due to the added complexity that discourages shortcuts such as memorizing the expected output. We completed experiments and gathered data that are better suited for supervised ML compared to previous available datasets. The new dataset can also be used to model fog as a PSF and empirically measure point spread functions to denoise fog images. The approach seeks to model the effects of fog as a point spread

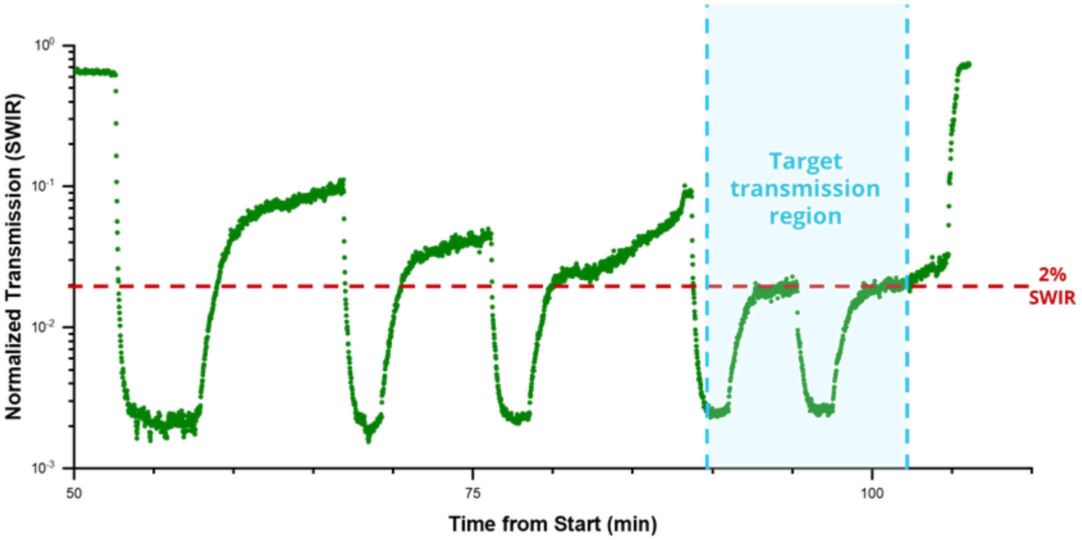

Figure 5-5. Transmission range in which data was gathered.

function that can then be used to back calculate an estimated clear image. The ML task is to estimate the degrading PSF function. Empirically measured PSFs can then be used to constrain the learning process of the ML model with the potential to lead to better generalization. This idea is further expanded on in the last section of this chapter.

5.4. Future Work

Future work will utilize the collected data to demonstrate ML's ability to improve our imaging capability in fog. With the new dataset three distinct models can be developed, the first being a purely physics-based approach by empirically measuring PSF from the PSF dataset, the second being a purely data-driven ML approach, and the third being a physics-informed ML approach that utilizes the empirically measured PSF to constrain or regularize the learning process of the ML component. The three approaches can be compared to see which method provides the best opportunity to detect a target masked by fog all as a function of fog condition.

More precisely, considering a clear image $f(x,y)$ and a foggy image $g(x,y)$, there exists a degradation function $h(x,y)$ or a PSF which when convolved with the clear image produces the foggy image

$$f(x,y) * h(x,y) = g(x,y). \tag{5.3}$$

In practice, we receive $g(x,y)$ and would like to estimate the clear image $f(x,y)$ which requires us to model the degradation function $h(x,y)$. Assuming we know $h(x,y)$ we can use the Fourier Transform (FT) to estimate $f(x,y)$, $f'(x,y)$

$$f(x,y) * h(x,y) = g(x,y) \rightarrow FT \rightarrow F(u,v) \times H(u,v) = G(u,v), \tag{5.4}$$

$$F(u,v) = \frac{G(u,v)}{H(u,v)} \rightarrow InverseFT \rightarrow f(x,y). \tag{5.5}$$

The issue is that it will be difficult to perfectly model $h(x,y)$ and we can almost assure there will be inaccuracies or noise that can be modeled by $\eta(x,y)$. Depending on how well we can model the degradation function, by minimizing $\eta(x,y)$, will determine how well we can recover the original clear image

$$h(x,y) + \eta(x,y) = h^{'}(x,y), \tag{5.6}$$

$$f^{'}(x,y) * h^{'}(x,y) = g(x,y) \rightarrow FT \rightarrow F^{'}(u,v) \times H^{'}(u,v) = G(u,v), \tag{5.7}$$

$$F^{'}(u,v) = \frac{G(u,v)}{H'(u,v)} \rightarrow InverseFT \rightarrow f^{'}(x,y). \tag{5.8}$$

Using this newly collected dataset one can develop the three distinct degradation models and note their ability to image as a function fog condition. Follow-on efforts of this project will seek to complete this study.

6. IMAGING AND SENSING WITH LASER SPECKLE

6.1. Introduction

We have developed a complete theory to describe speckle correlations over object position [107], providing a method for imaging through heavy amounts of scatter. Earlier experimental work investigated the key parameters of this theory for example objects [16, 108] and suggested subwavelength-sensitivity [109]. The concept relates to a computational imaging method we proposed involving motion in structured illumination, including a variant where the incident field is varied.

Speckle intensity correlations over object position are obtained by capturing speckle patterns as a function of translated object position. The resulting speckle intensity spatial decorrelation can be attributed to physical changes in the structure of the scattering medium [110], and changes in the excitation, such as laser frequency [110, 111, 112] or beam shape [113, 114]. Fixing all of these parameters allows the decorrelation to be attributed solely to the movement of the object of interest, given sufficient interaction of the detected light and the object. Taking advantage of all available pixels on a camera, we can form a statistical average at each object position, in lieu of the mathematical picture of forming an average over the random background scatterer configuration. This process of forming an average intensity correlation over object position provides enough information to be able to reconstruct an image of the object.

Recently, we have extended this work to facilitate new capabilities and application spaces. The ability to image objects hidden in fog has been demonstrated, as has sensitivity to fog composition. Additionally, definitive evidence has been shown of far-subwavelength-scale features of scattering objects becoming available. Also, the ability to simultaneously image and localize objects has been demonstrated. Finally, an interferometric effect in speckle intensity correlations has been found.

6.2. Characterization of Fog and Sensing of Hidden Objects

We have extended our technique of sensing hidden objects with speckle correlations to the situation of imaging in fog. This is a significant development, because fog is a dynamic scattering medium. Fog also occurs naturally, meaning the ability to characterize fog and achieve remote sensing through it is extremely valuable. We have completed a series of experiments in which we have shown the ability to characterize fog based on its density and composition. We have also demonstrated sensitivity to the geometry of hidden moving objects.

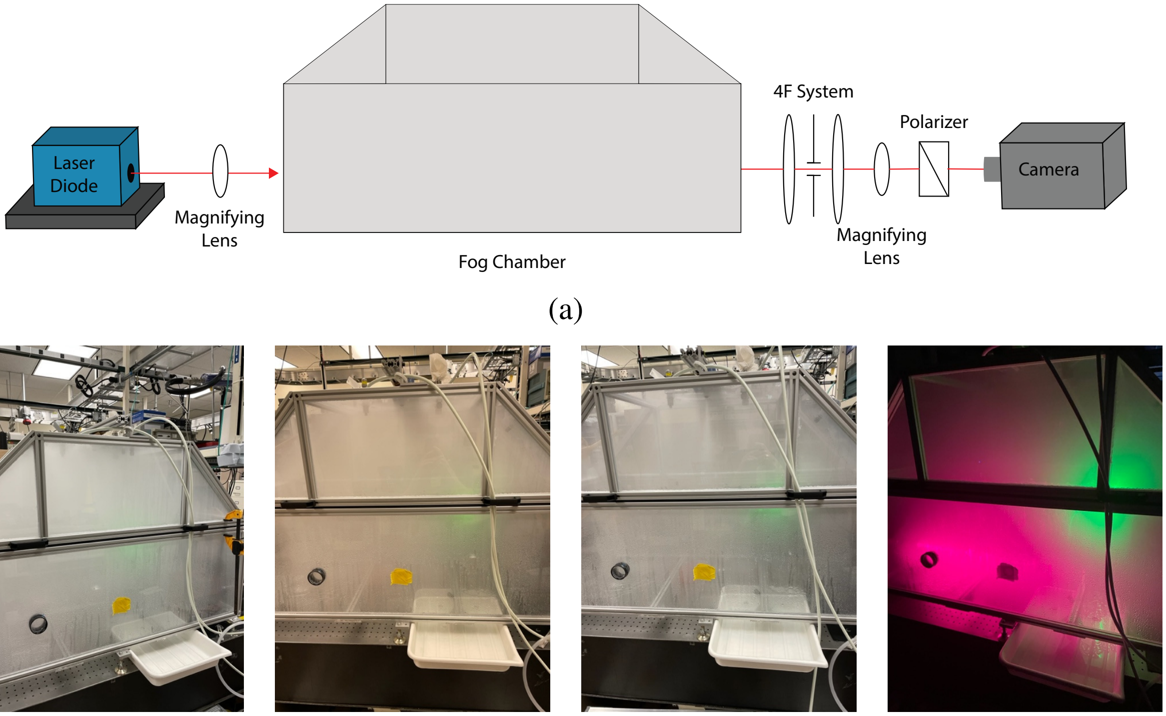

(a)

(b) (c) (d) (e)

Figure 6-1. (a) Experimental setup. (b) “Default” fog. (c) “Low pressure” fog. (d) “No salt” fog. (e) The “Default” fog with experiment running; the red laser (DL Pro) was used for imaging using generated speckle, while the green laser (Artium) was used to sense particle size and velocity.

The experiments described used the “MiniFog” Tabletop Fog Chamber, described in Chapter 3. Coherent 670-nm laser light (500 mW, Toptica DL Pro) was used for illumination and a Phantom V1210 camera was focused a few centimeters inside the fog chamber (prior to fog generation) through the imaging optics shown in Fig. 6-1(a). Three distinct types of fog were used in experiments, which were created by combining pressurized air and water with a spray nozzle. The first, referred to as “default” fog, was a thick advection fog, primarily seen out at sea and on shorelines, which was made from salt water with a 10 g/L salt density. This parameter set is the same as **Tabletop Fog 2** from Chapter 3. This fog completely obscured objects inside the chamber, as seen in Fig. 6-1(b). The other fog recipes used were “low pressure” fog, which was identical to the default fog, except that the pressure in the air tank was reduced, resulting in a thinner fog, equivalent to the default fog following dissipation. This parameter set is the same as **Tabletop Fog 6** from Chapter 3. The final fog was “no salt” fog, which was equivalent to the default fog, but without salt. This parameter set is the same as **Tabletop Fog 1** from Chapter 3. This fog was significantly thinner than both of the other fog types.

Speckle correlations over time were measured through all three types of fog and sensitivity to the fog composition and density was observed. Fig. 6-2(e) shows a comparison of speckle correlations of all three fog recipes measured exactly two minutes after a 2-minute fog spray. Thinner fog recipes resulted in speckle correlations with a higher minimum correlation value, which can be explained by more ballistic light reaching the camera through the fog, creating

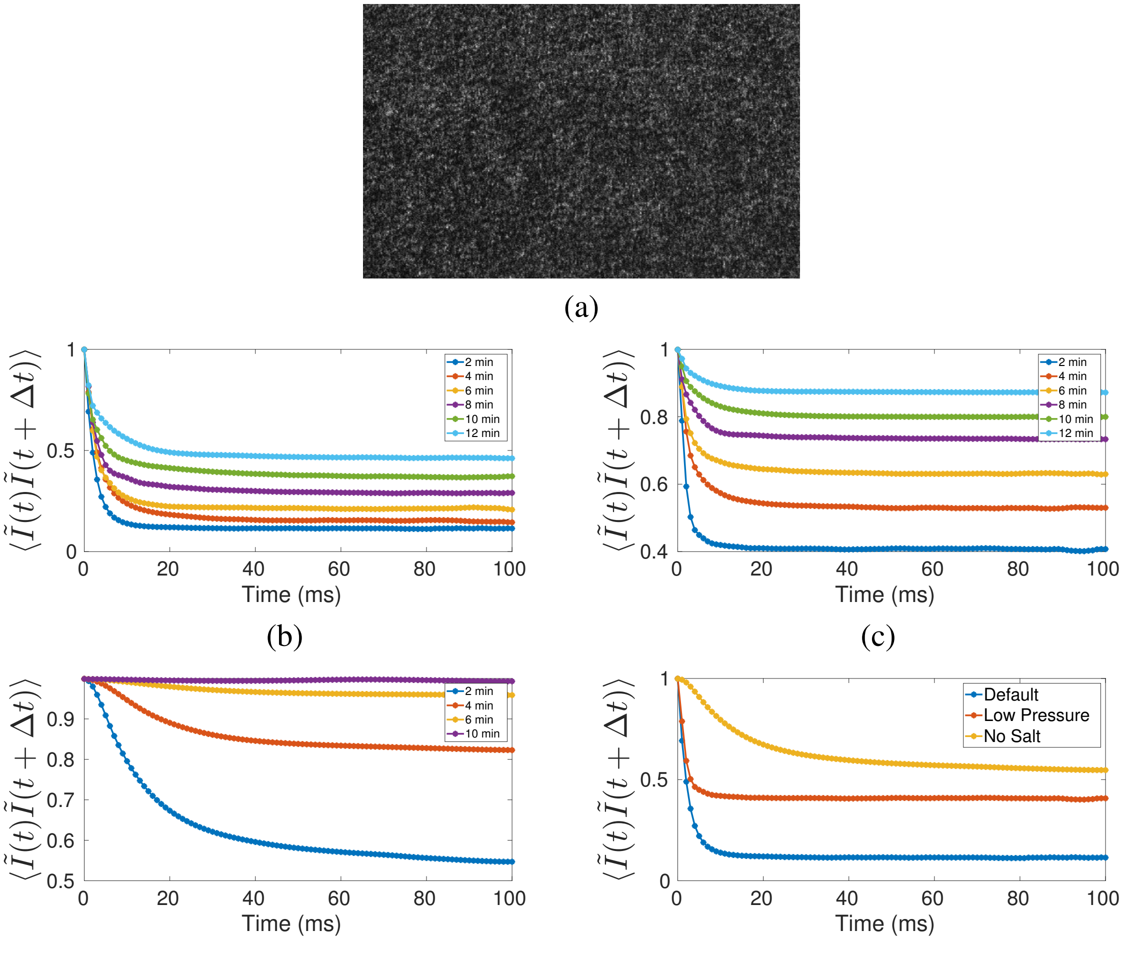

(a)

(b)

(c)

(d)

(e)

Figure 6-2. (a) Speckle image in fog. (b) Temporal speckle correlation in default fog, with sets of speckle images taken in two minute intervals after the fog spray. (c) Temporal speckle correlation in low pressure fog. (d) Temporal speckle correlation in fog without salt. (e) Temporal speckle correlation over sets of speckle images taken two minutes after the fog spray for the three fog recipes.

similarities in the speckle images. The speckle images from the “no salt” fog also decorrelated more slowly than the other two, likely the result of both differences in fog composition and decreased sensitivity to the field motion as a result of a less heavily scattering medium [115]. This is also seen as the fog dissipates, as demonstrated in Figs. 6-2(b)–(d).

The challenge of applying speckle intensity correlations to imaging and sensing of moving objects in fog is that the method is also sensitive to the motion of the fog particles. As seen in Fig. 6-3(b), speckle measured through the advection fog decorrelates rapidly and reaches an approximate minimum in just a few milliseconds. This non-zero minimum is a result of ballistic light getting through the fog and creating inherent similarities between speckle images and is therefore heavily influenced by the fog density. The millisecond-scale temporal decorrelation presents a substantial obstacle to object sensing, as the decorrelation due to object motion must be distinguishable from that due to scatterer motion. One way to overcome this challenge is to use an object that is moving sufficiently fast to cause the intensity correlation curve to reach a minimum faster than it would have with no object. According to theory and previous experiments, such an intensity correlation curve will reach a minimum at the diameter of the object, assuming optimized experimental conditions [116, 16]. Therefore, using object speed to overcome the limitations imposed by the particle motion requires that the object move by its diameter in only a few milliseconds.

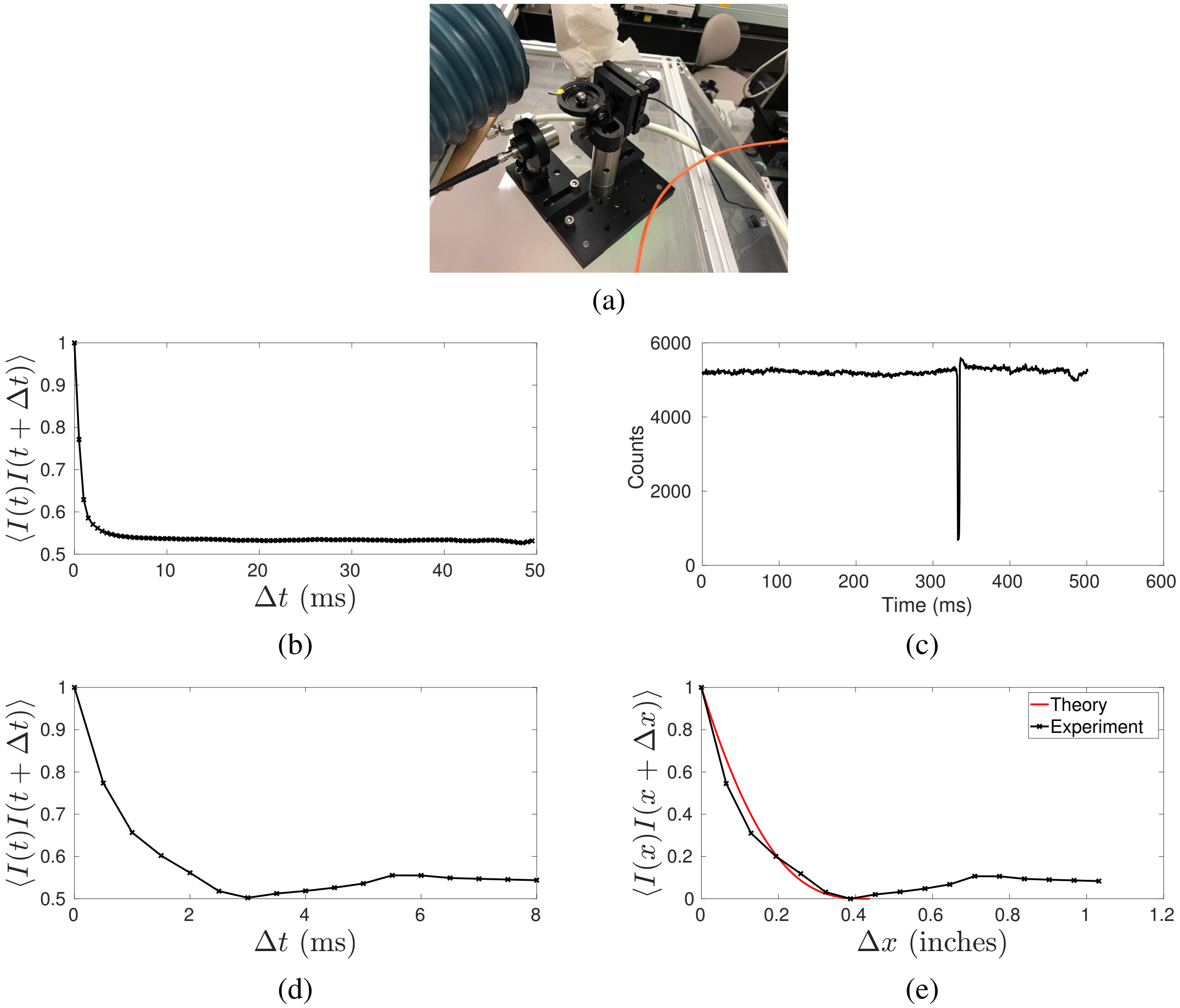

(a)

(b)

(c)

(d)

(e)

Figure 6-3. (a) Spherical ball bearing with dropping mechanism (b) Intensity correlation over time in "default" fog without object. (c) Mean intensity over time measured while a 7/16" ball is dropped in default fog. A clear drop in mean intensity is seen as the ball creates a shadow on the camera. (d) Intensity correlation over time for 8 ms centered on the drop in mean intensity. (e) Temporal intensity correlation during ball drop converted from time to distance using free-fall mechanics. Excellent agreement is shown between the experimentally measured intensity correlation and the theoretical curve for a 7/16" circle.

The objects in the experiments described were a series of spherical steel ball-bearings. A custom-built ball-drop mechanism, shown in Fig. 6-3(a), was placed on top of the fog chamber a few cm away from the plane of focus. This device contained a sensor which triggered the camera after the ball was dropped via a lever through the center. Upon triggering, the camera collected images at a fixed rate of 2 kHz for 0.5 s, enough time for the ball to fall past the imaging spot to the bottom of the fog chamber. These images were normalized to yield a mean intensity of zero and a standard deviation of one, with the normalization given by $\tilde{I} = (I - \langle I \rangle)/\sigma_I$, where $\langle I \rangle$ is the mean intensity formed as an average over a given camera image and σ_I is the standard deviation over the camera image. The experiments yielded a contrast ratio close to unity ($\sigma_I/\langle I \rangle \approx 1$), but we find the aforementioned normalization with σ_I to be better in this work. The spatial correlation at each temporal offset Δt was formed using all pairs of speckle images sharing the same offset [116], resulting in more data samples for the smaller temporal offsets, which are the most important for determining object information.

Figure 6-3 shows the result of the experiment for a 7/16-inch ball bearing dropped two minutes after the fog spray for the "default" advection fog, with the fog still quite dense, demonstrating the effectiveness of this method in the most heavily-scattering fog. Comparing Figs. 6-3 (b) and (d) shows that the presence of the falling object caused the speckle to decorrelate faster, and that the shape of the curve was altered. Fig. 6-3 (e) shows the same result as Fig. 6-3 (d), but rescaled from 0 to 1 and with the x-axis converted from time to distance. This was done based on free-fall mechanics for the moving object, with the speed of the object approximated to be a constant 0.129 inches/ms over the 8 ms of data used in the calculation, based on the object's initial height and the distance from that height to the plane of the imaging spot. The "theory" curve is the square of the autocorrelation function of a simple 7/16-inch circle, an approximation based on a theory developed for moving objects [116]. This is the first time that our speckle imaging theory has been applied to three-dimensional objects, and our understanding is still evolving. However, the experimental data suggests that the object should be modeled as a circle. Agreement between the theoretical and experimental curves is quite good, indicating that the geometry of the moving object can in fact be determined by speckle intensity correlations through heavily-scattering fog. It has also been shown previously that speckle intensity correlations over object position can be used to reconstruct images of the hidden objects through iterative phase retrieval, as long as such correlations are measured along two spatial dimensions [16] or assumptions are made about the symmetry of the object [117]. Therefore, this result implies direct extensions to imaging of hidden moving objects in thick fog.

Figs. 6-4 (a) and (b) show experimentally measured speckle intensity correlation curves for two ball bearings of different sizes dropped in the "default" fog. Figs. 6-4 (c) and (d) show reconstructed images of those ball bearings using the experimental data and a phase retrieval algorithm, as demonstrated in other applications in previous work, and extrapolating the experimental data based on known circular symmetry of the object [117, 16]. The shapes and sizes of the ball bearings can be clearly seen, and with improved experimental data, the reconstruction could be improved further.

6.3. Super-Resolution Sensing

We have conducted experiments that demonstrate the ability to distinguish far-subwavelength geometrical features using object motion in a speckled field [118]. In these experiments, which used the setup shown in Fig. 6-5 (a), the object is translated in a speckled field. The speckle field is created by passing a coherent laser through a stack of ground-glass slides. The resulting field interacts with the object, and then with an analyzer constructed from another stack of

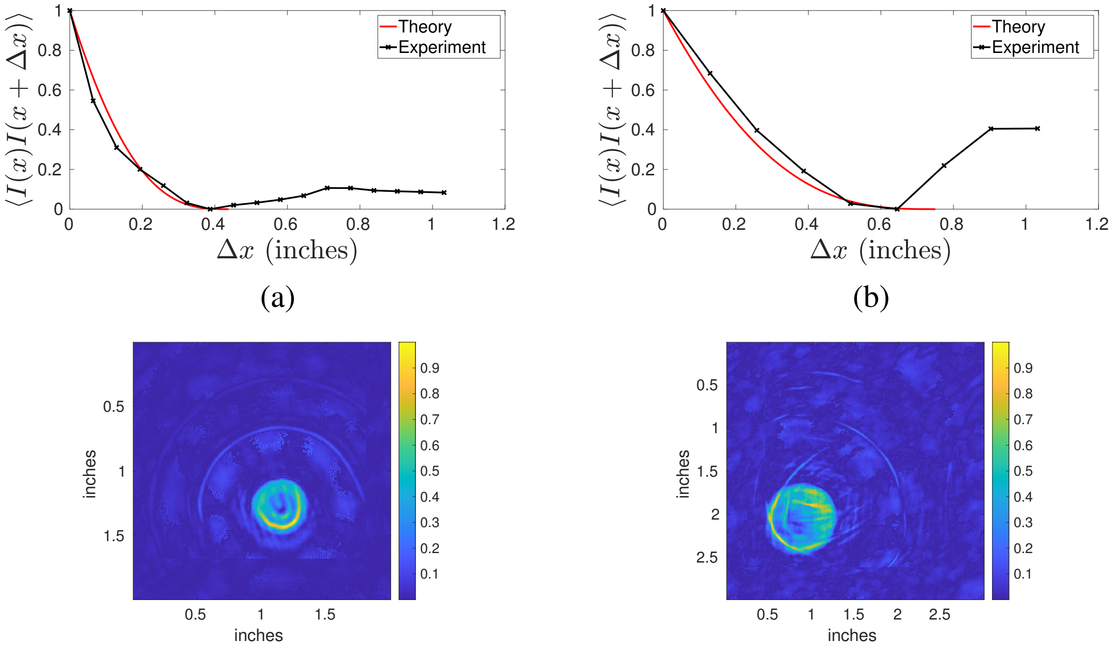

(a)

(b)

(c)

(d)

Figure 6-4. (a) Speckle intensity correlation over object position for 7/16" ball bearing dropped in default fog. (b) Speckle intensity correlation over object position for 3/4" ball bearing dropped in default fog. (c) Reconstructed image of 7/16" ball using experimental data and phase retrieval. (d) Reconstructed image of 3/4" ball using experimental data and phase retrieval.

ground-glass slides. The imaging optics include a $4f$ system to control the speckle size, and a magnifying lens. A linear polarizer is used to ensure negative exponential statistics at the imaging plane. The interaction between the speckle field and the object provide access to sub-wavelength features of the object.

In one experiment, two macroscopically identical acrylic rods embedded with 50 nm TiO_2 scatterers were placed into the experiment one after the other, and were translated by a total distance of approximately two wavelengths through the speckle field. Normalized speckle images were collected as a function of object position. Each measurement was repeated 20 times to form statistical averages. After scanning each rod 20 times, the first rod was placed into the experiment again and scanned an additional 20 times to demonstrate the potential for unique identification of each rod. As shown in Fig. 6-5, intensity correlation curves measured for two nominally identical scattering rods made of the same material were different over a far-subwavelength distance, indicating that we achieved sensitivity to the arrangement of scatterers in each rod and/or to surface roughness.

Temporal decorrelation was measured over the experimental runtime with the object at its center scanning position and was found to be negligible, as indicated in Fig. 6-5(a). Various remote sensing applications are enabled by this discovery, including material and structure of hidden object, material defect detection, unique identification of scattering objects, and assuming adequate optical contrast, unlabeled protein tracking.

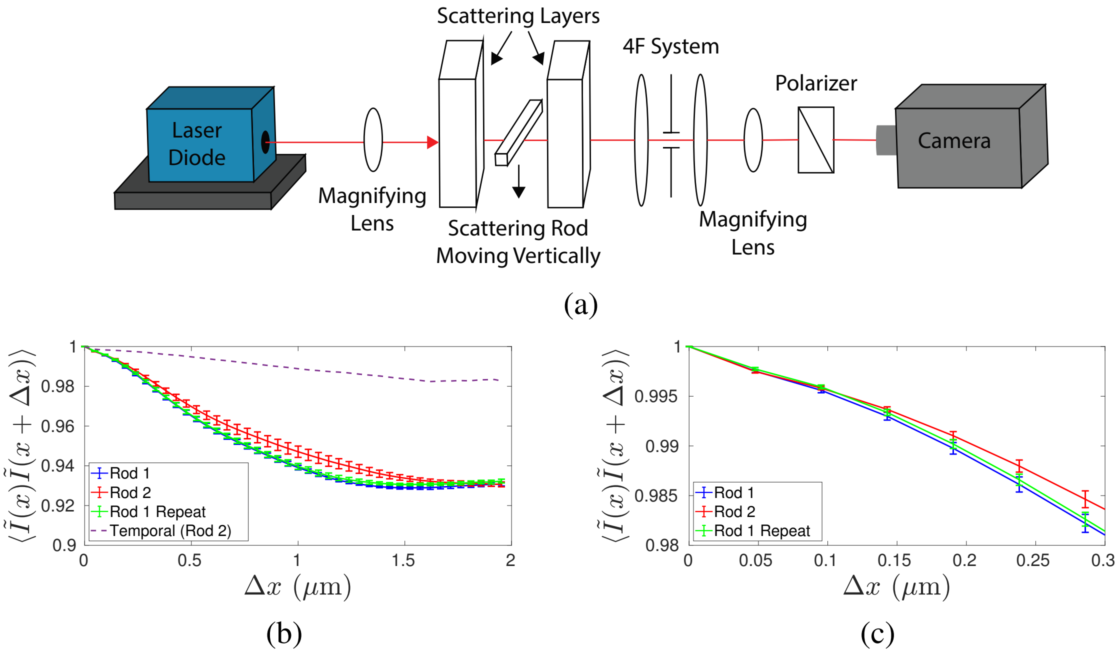

(a)

(b) (c)

Figure 6-5. (a) The experimental arrangement, with an expanded 850 nm laser beam illuminating two scattering slabs with an acrylic scattering rod between them, and being imaged through a 4f system and magnifying optics. (b) Intensity correlation curves for two nominally identical scattering rods. The curves are distinguishable on a length scale far less than the incident wavelength, indicating sensitivity to far sub-wavelength features. (c) A magnified plot of the intensity correlation curves for the rods.

6.4. Imaging and Localization of Arbitrary Objects in Reflection and Transmission

Significant progress has been made in experiments related to imaging and sensing through scatter using speckle intensity correlations in both the transmission and reflection measurement geometries. Our earlier experiments involved both apertures and patch-like objects in a transmission arrangement, and we have shown successful object reconstructions using our theory with phase retrieval. More recently, we have extended this work to a reflection geometry, where the incident laser beam and the camera are on the same side of the scattering medium and the object of interest is made of reflective metal, an arrangement which is representative of imaging satellites through the atmosphere. For example, using an object that consisted of two identical reflective strips of metal, we were able to correctly obtain the size of the strips and the distance between them, indicating that we can sense multiple objects through scatter and determine defining characteristics of those objects. The results are shown in Fig. 6-6. Additionally, have successfully reconstructed an image of a circular mirror through measurement of speckle intensity correlations in reflection through heavily scattering acrylic, the results of which are shown in Fig. 6-7.

Additionally, we have developed an approach to simultaneously image (with coherent speckle information) and localize (using a point-object picture in a diffusion framework with mean intensity data) objects hidden inside or behind scattering materials. Previously, we had localized hidden objects through the use of a diffusion model, and earlier experiments have demonstrated the localization of hidden objects that absorb light or emit light (fluoresce) [119]. However,

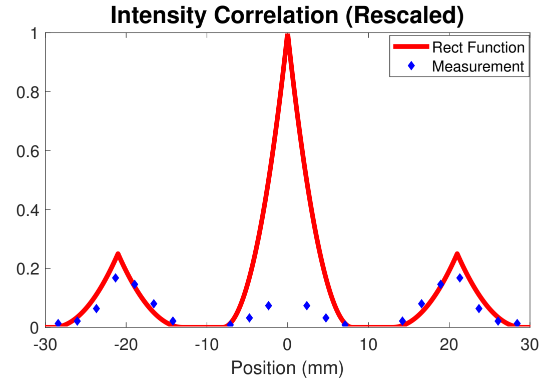

Figure 6-6. Intensity correlation as a function of position for an object consisting of two 8-mm-wide reflective strips of metal. The mirrors were spaced by 21 mm center-to-center. This experiment was carried out in reflection through a ground glass diffuser with a 532-nm laser, and the intensity correlation plot clearly shows the size of the two mirrors and the distance between them. The blue points show the measured intensity correlation, while the red line shows the simulated intensity correlation from a rectangular function with dimensions equal to those of the object.

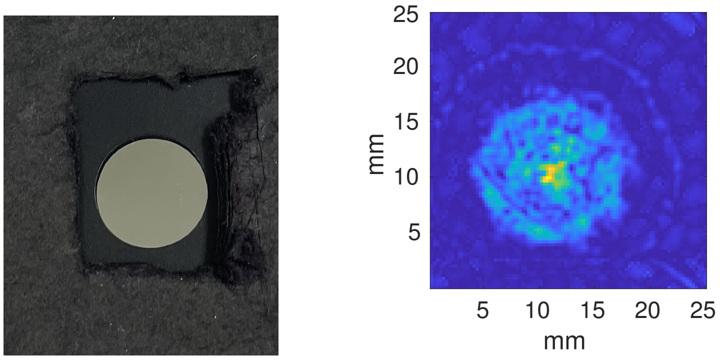

(a) (b)

Figure 6-7. 15-mm reflective circle imaged through heavily scattering acrylic. (a) Photo of the object. (b) Reconstruction showing the correct size of the object. Imaging was achieved by scanning the object in 1 dimension and taking advantage of the object's rotational symmetry, then rescaling the measured speckle intensity correlation curve to account for decorrelation due to surface roughness of the material surrounding the object.

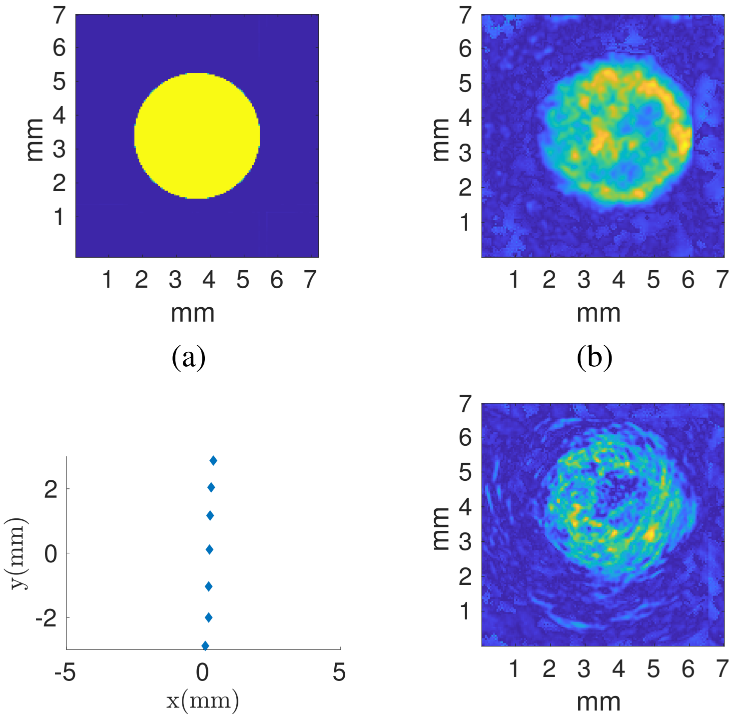

(a) (b) (c) (d)

Figure 6-8. (a) Simulated object function. (b) Reconstructed image of the object using known object positions. (c) Localized object positions. (d) Reconstructed image of the object using localized object positions.

lacking was a method to simultaneously localize and image hidden objects using data from a single camera. Now we have developed a method whereby we can accomplish this using a moving laser source and mean intensity data from speckle images [120]. This concept could be particularly useful for air and space applications, as in theory, our method could be used to find the position of a moving object through the atmosphere, and then that information utilized to form an image of the object from speckle correlation data. We have successfully localized and imaged a circular patch object in transmission, even using scant experimentally determined object positions for the image reconstruction. Using the same arrangement as in Fig. 6-5, an experiment was performed in which a 3.7-mm circular patch was hidden in between two 6-mm layers of scattering acrylic. The object was moved in 1-mm steps and speckle images were collected. A 2×11 array of laser source positions, produced by changing the laser position and repeating the experiment, was used to localize the object using the mean intensity of the speckle images collected. Exploiting the object's circular symmetry, we reconstructed an image of the object using iterative phase retrieval. Figure 6-8(b) shows the reconstruction results using known object positions from our motorized stage and Fig. 6-8(d) shows the reconstruction results obtained from localized object positions. The latter demonstrates that image reconstruction is possible without prior information about the object's position or motion.

6.5. Interferometric Object Sensing and Localization using Laser Speckle

We present experimental results demonstrating an interference effect discovered in speckle intensity correlations over the spatial positions of a moving hidden object which could be used to characterize and localize hidden objects through a thick randomly scattering medium. Previously, speckle intensity correlations over incident field position on the other side of a scattering medium were shown to provide access to characteristic information about the incident field, allowing the field itself to be reconstructed [121]. When using multiple laser sources, information about the difference in incident wave vectors of the sources is also retained [122]. The interferometric effect described here provides a new avenue to access coherent information about an object, regardless of the level of random scatter, thereby offering opportunities for imaging and sensing in and through various forms of environmental scatter. By using two non-overlapping laser sources at different angles with no object, it was previously found that when scanning the beams while keeping the beam separation distance constant, a beat was present in the speckle intensity correlations which was related to the difference in the incident beam angles [122]. By using a single stationary incident laser beam and measuring speckle intensity correlations over object position in reflection, with a mirror behind the object, we now show that a beat exists in the correlations due to an interferometric phenomenon.

The experimental setup is shown in Fig. 6-9. A coherent laser beam (Newport TLB-6917, 850 nm) was incident at an angle on a scattering medium, which was composed of three similar ground-glass slides, and an object was placed behind the scattering medium and in front of a mirror. The mirror was located 5 cm behind the scattering medium and the object was placed approximately 2.5 cm behind the scattering medium. A camera (Photometrics Coolsnap HQ) imaged a small spot (about 1 mm × 1 mm) on the front surface of the scattering medium through a 4f system, used to regulate the speckle size on the camera. Speckle images were collected as the object was moved with a motorized stepper-motor-driven stage (Zaber TLM-150A). The position and angle of the incident laser spot were controlled with a motorized mirror (Zaber T-MM2). These speckle images facilitate averaging.

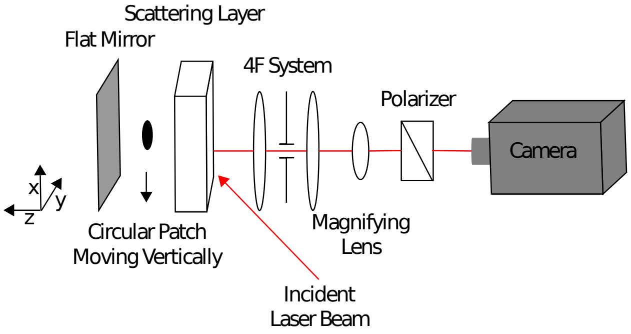

Figure 6-9. Experimental setup, with an absorptive black circular object placed between a scattering medium and a mirror. Speckle images were collected as a function of translated object position.

Example experimental results using the parameters given in Table 6-1 are shown in Fig. 6-10. The interference effect is due to the multiple interactions with the object as the speckle field is transmitted and then reflected back to the detector. The interference creates an oscillation in the speckle intensity correlations which has a beat related to object position and size. Coherent interactions between the object and mirror clearly survive the random scatter, providing a new perspective on earlier random interferometry [123], where relative time delays between two beams became evident in speckle intensity correlations. This interferometric phenomenon could be exploited to both localize and characterize a hidden moving object.

Table 6-1. Experiment parameters for the results in Fig. 6-10.

Fig.	Object Diameter (cm)	Laser Spot Position (cm) (*x*, *y*)	Object Starting Position (cm) (*x*, *y*)
6-10(a)	1	(0, -1.5)	(0, 0)
6-10(b)	0.37	(0, -1.5)	(0, 0)
6-10(c)	1	(0, 1.5)	(0, 0)
6-10(d)	1	(0, -1.5)	(0, 0)
6-10(e)	1	(0, -1.5)	(-1, 0)
6-10(f)	1	(0, -1.5)	(-1, -2)

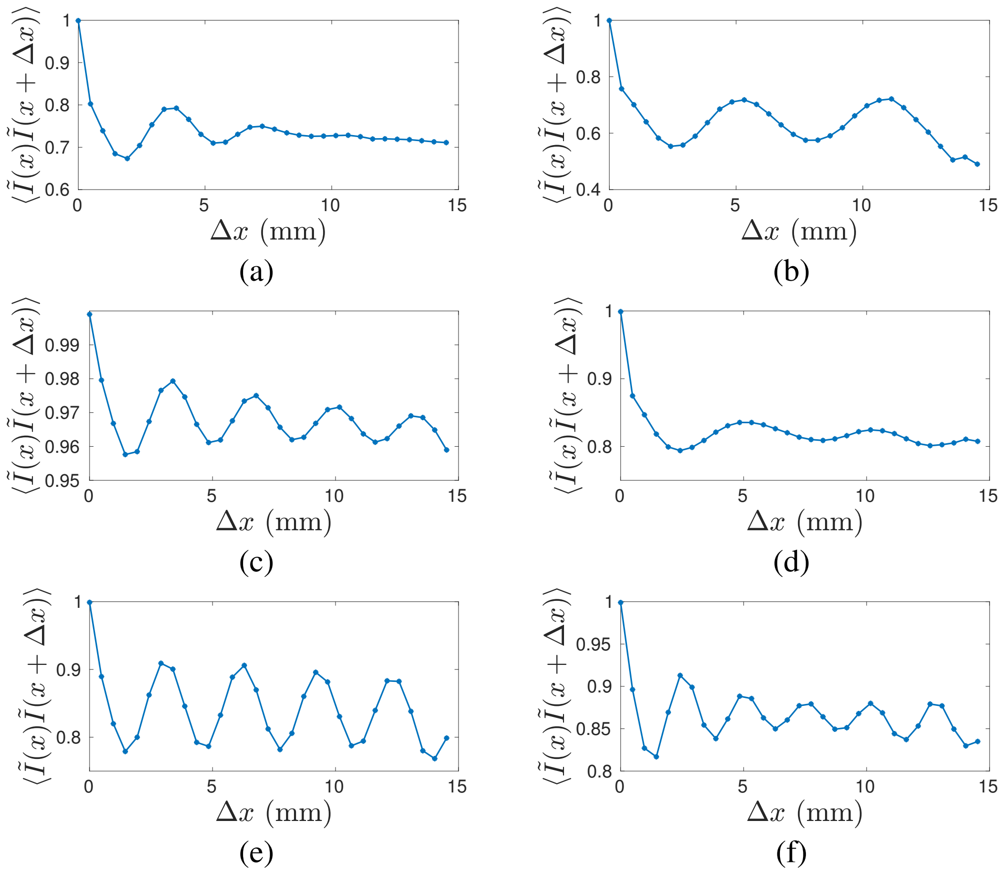

(a) (b) (c) (d) (e) (f)

Figure 6-10. Measured speckle correlations over translated object position using the arrangement in Fig. 6-9 with variations in object size and laser illumination spot. The interference ripples depend on both the object size and the relative positions of the excitation laser spot and the object with respect to the detection region on the scattering medium at (x, y) = (0, 0).

6.6. Conclusion

We have demonstrated several new applications of speckle intensity correlations to sensing in heavily scattering environments. Imaging moving objects in fog has been demonstrated, showing that this method can be implemented in dynamic scattering media. Because this method is not subject to the limits of ballistic light, imaging through even more heavily scattering fog and aerosols should be possible. Sensitivity is also shown to fog composition, implying extensions to fog characterization.

The ability to distinguish nominally identical objects on a far-subwavelength scale is also demonstrated, implying numerous applications ranging from defect detection to security. Additionally, we have shown the capability to simultaneously image and localize hidden objects, which allows this method to be effective without prior object positional information. Finally, the interferometric effect shown illustrates a new approach to analyzing speckle intensity correlations that may lead to more effective ways to localize and image moving objects. All of these results represent significant developments that challenge the limits of the application of speckle imaging and open important application spaces.

7. SUPER-RESOLUTION RADAR

7.1. Introduction

In various optical experiments and situations, we have demonstrated that far sub-wavelength information can be extracted using relative motion in structured illumination [16, 124, 107, 109]. While the (microwave) radar problem is fundamentally similar to the optical one, there is at least one key difference. In optical structured illumination microscopy, both the illumination and the measurement have spatial support on the order of the distance to the target. In the case of monostatic radar, both the illumination and the measurement have very small spatial support ($\approx$3 orders of magnitude smaller) relative to the distance to the target. As a result, the sensitivity of the measurement to changes in the target is considerably lower, making it more challenging to extract enhanced object information. Of course, the result can be enhanced with multiple detector apertures separated by substantial distances.

While sub-wavelength transverse resolution is likely not achievable for stationary radar systems, as it is in the optical case, relative motion in structured illumination may still provide a significant resolution benefit. Making a set of known changes to an illumination pattern and measuring the resulting scattered fields provides additional information relative to using a fixed illumination pattern, because we are able to see how the system responds to a range of inputs, rather than just one. As a result, it is reasonable to expect a commensurate enhancement in resolution if this extra information is properly captured and utilized.

Existing radar technologies, such as monopulse radar, can localize the center of a target very accurately, but are unable to distinguish multiple objects at close transverse separations in the far field. Synthetic aperture radar systems can image a target with very high transverse resolution, but require a large number of measurements at varying positions, and are thus primarily suitable for applications where the target is stationary and the radar system is mobile. Relative motion in structured illumination may allow for both high transverse resolution and a relatively fast measurement using a single stationary antenna.

Angular super-resolution algorithms for scanning radar based on constrained deconvolution of the beam pattern and the measured data have been presented previously in the literature [125, 126], however, more work is needed to address the basis for these results. We also believe that the performance of these approaches can be greatly exceeded using the theoretical framework of relative motion in structured illumination, and that the maximum achievable resolution of a radar system is fundamentally limited only by the achievable SNR. By means of simulations and a rigorous analysis of the problem through the lens of information theory, we seek to develop an understanding of the maximum achievable resolution for scanning radar that factors in noise, beam geometry, and sampling strategy.

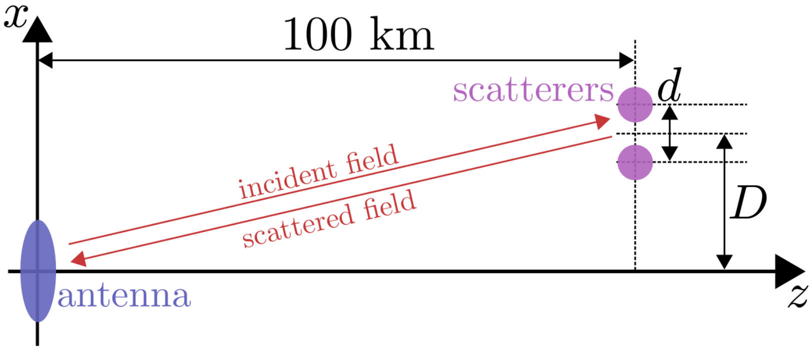

Figure 7-1. The geometry used for the enhanced transverse radar resolution simulation results.

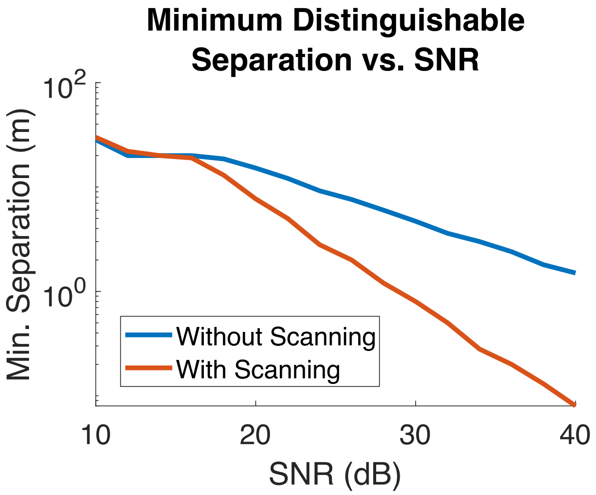

Figure 7-2. Minimum distinguishable scatterer separation from noisy simulation data as a function of SNR for a static measurement repeated multiple times ("without scanning") and multiple measurements with beam scanned over scatterers across its FWHM ("with scanning"). Scatters are positioned 100 km away from the 10 m^2 aperture antenna, at a frequency of 10 GHz, with 40 total samples.

7.2. Simulation Results

Initial work in this domain has focused on simulations considering two idealized scatterers illuminated by a structured radar beam produced by an aperture antenna, as shown in Fig. 7-1. The magnitude and phase of the scattered fields are measured by the antenna, with random Gaussian noise added to the field measurements. A forward propagation model is then inverted to provide an estimate of the scatterer separation from the noisy data.

Initial results suggest that scanning a structured beam over the target can yield significantly enhanced transverse resolution. Figure 7-2 shows simulation outputs for the minimum separation where the two scatterers are distinguishable as a function of SNR. The scatterers are positioned 100 km away from the antenna, which is a 10 m^2 square aperture operated at 10 GHz. The beam produced by this antenna has a FWHM of around 300 m at 100 km. The total number of samples is held equal between the scanning and non-scanning cases (either a single measurement is taken at each of 40 scan angles or 40 measurements are taken at a fixed position).

These results show a significant enhancement in the ability to determine the separation of the scatterers with scanning, especially at high SNRs. Additional simulations are in progress that will analyze a broader range of parameters and allow determination of where motion in structured illumination provides the greatest resolution advantage. Work is also in progress to fully understand the theoretical basis through which this additional resolution is obtained using the framework of information theory.

7.3. Conclusions

A theory was developed and simulations were performed in order to assess the potential transverse resolution benefit of relative motion in structured illumination for radar systems. Simulation results considering a simplified radar system indicate that significant resolution benefits are possible using data from scanning a structured beam over the target along with appropriate signal processing.

While our simulations showed significant enhancements in resolution at high SNRs, our initial results suggest that there is little or no enhancement in resolution with scanning at low SNRs. Our theoretical analysis of the problem suggests that the resolution benefit of scanning should persist regardless of SNR. We believe that this discrepancy is due to the specific cost function and algorithm which is used to invert the noisy simulation data. An enhanced inversion methodology is currently being developed which should yield better results at low SNRs. In addition to investigating this discrepancy further, we plan to perform simulations and analysis to demonstrate the role that beam geometry, constraints, and sampling strategy play in resolution.

This work has a wide range of potential applications which are relevant to national security. Improved transverse radar resolution could help detect aircraft in a cluttered or jammed environment, enhance sensing for autonomous vehicles, and more accurately track satellites in orbit. Since our approach is focused on developing strategies for sampling and signal processing, rather than design of the physical radar sensor, the understanding we are developing could readily be applied to existing radar systems. Additionally, underlying theoretical developments in relative motion in structured illumination are applicable to other coherent sensing topologies (for example, in the optical or acoustic domains).

8. TEAM BIOGRAPHIES

8.1. Sandia National Laboratories

Brian Z. Bentz served as the principal investigator for this project. His research contributions included the development of the approximate light transport model and it's application for computational detection, localization, and imaging of objects in fog, as outlined in Chapter 2. Brian received his B.S. and Ph.D. in 2011 and 2017, respectively, from Purdue University, West Lafayette, Indiana, both in electrical and computer engineering. In 2017, he joined the Applied Science and Technology Maturation Department (7585) at Sandia National Laboratories, Albuquerque, New Mexico. In 2021, he joined the Applied Optical and Plasma Science Department (1865) also at Sandia National Laboratories, Albuquerque, New Mexico, and is a Senior Member of Technical Staff. He can be contacted by email at bzbentz@sandia.gov.

Jeremy B. Wright supported the project as a consultant and provided program direction recommendations. Jeremy received his B.S., M.S., and Ph.D. in 2007, 2010, and 2014, respectively, from the University of New Mexico in electrical engineering. He has supported efforts in degraded visual environment research since 2014 and is a Principal Member of Technical Staff in the Weaponization and Signature R&D Department (6772) at Sandia National Laboratories, Albuquerque, New Mexico.

John D. van der Laan supported the experiments described in Chapters 2 and 3 and contributed the polarization imaging work presented in Chapter 4. He is an Optical Scientist with nearly a decade of experience modeling, building, and testing diverse optical systems/experiments in challenging remote sensing environments. He currently is a principal member of technical staff in the Proliferation Detection Remote Sensing Department (6751) at Sandia National Laboratories in Albuquerque, New Mexico. He has developed and field-tested systems across the optical and infrared spectrums (VIS, NIR, SWIR, MWIR, LWIR). He is also an expert in modeling and experimental analysis of visible and infrared light transport in scattering environments and computational hyperspectral systems. Prior to joining Sandia National Laboratories he obtained his Ph.D. in Optical Sciences from the University of Arizona and a B.S. in Electrical Engineering from Michigan Technological University. He can be contacted by email at johvand@sandia.gov.

Andres L. Sanchez is a Chemical Engineer with expertise in aerosol and atmospheric science. He contributed to this effort as the point of contact for SNL Fog Chamber. Andres received his B.S. and M.S. in Chemical Engineering from the University of New Mexico, Albuquerque, NM, in 2008 and 2012, respectively. In 2005, he joined Sandia National Laboratories and has worked for several atmospheric and aerosol science related organizations. He can be contacted by email at asanch3@sandia.gov.

Christian A. Pattyn is a Ph.D. Candidate at the University of New Mexico who served as experimental and technical support and development for this project. His research contributions included the development, characterization, and deployment of the Tabletop Fog Chamber, as detailed in Chapter 3. Christian received his B.Sc. in Chemical Engineering and M.Sc. Biomedical Engineering, both from the University of New Mexico in Albuquerque, New Mexico. He is currently a member of the Weaponization and Signatures R&D Department (6772) at Sandia National Laboratories. He can be contacted by email at capatty@sandia.gov.

John P. Zenker supported the enhancement of the Sandia National Laboratories Tabletop Fog platform to enable the generation of fog from dry aerosol particles as outline in Chapter 3. He received his B.S in Meteorology from Penn State University in 2013 and his M.S. in Atmospheric Science from Texas A&M University in 2017. In 2021, he joined the WMD Threats and Aerosol Science Department (6633) at Sandia National Laboratories in Albuquerque, NM. He can be contacted at jpzenke@sandia.gov.

Brian J. Redman supported the experiments described in Chapters 2 and 3. He is currently a member of the Counter-Autonomy and Physical Security Systems Research and Development Department (6534) at Sandia National Laboratories, Albuquerque, New Mexico.

Elihu Deneke served as a Machine Learning subject matter expert and led efforts in the development of machine learning models to image in fog as outlined in Chapter 5. He earned his B.S. degree in mechanical engineering and his M.S. degree in engineering, both at Prairie View A&M University, Prairie View, Texas, and completed his Ph.D. in mechanical engineering at Purdue University, West Lafayette, Indiana. After completing his Ph.D. in Dec. 2021, Elihu joined Real-time Computing Research Department (6776) at Sandia National Laboratories, Albuquerque, New Mexico. He can be contacted by email at edeneke@sandia.gov.

Andrew Glen designed the tabletop fog chamber described in Chapter 3. He is currently a member of the Atmospheric Sciences Department (1893) at Sandia National Laboratories, Albuquerque, New Mexico.

Karl Westlake supported the experiments described in Chapters 2 and 3. He is currently a member of the Weaponization Science R&D Department (6772) at Sandia National Laboratories, Albuquerque, New Mexico.

8.2. Purdue University

Kevin J. Webb is a professor in electrical and computer engineering at Purdue, where he has been on the faculty since 1990. Prior to that and after completing his Ph.D. from the University of Illinois in 1984, he was on the faculty of the University of Maryland, College Park. He grew up in Australia and came to the United States for graduate school. He is a fellow of the IEEE, APS, and Optica. He can be contacted by email at webb@purdue.edu.

Ryan L. Hastings worked on all of the experimental results presented in Chapter 6. Ryan received his B.S. in physics from Indiana University in 2017 and is currently pursuing a Ph.D. at

Purdue related to coherent sensing and imaging in scattering media with laser light. He can be contacted by email at hasting1@purdue.edu.

Christopher M. Lacny worked on the super-resolution radar concept utilizing relative motion in structured illumination presented in Chapter 7. Christopher received his B.S. in electrical engineering from Purdue in 2021 and is currently pursuing a Ph.D. at Purdue. He can be contacted by email at clacny@purdue.edu.

David W. Alexander contributed primarily to the laser speckle results and background material for the structured-illumination radar work. David received his B.Eng. in electrical and computer engineering from the University of Queensland, Australia in 2020, and is currently pursuing a Ph.D. at Purdue University, West Lafayette. He can be contacted by email at alexa210@purdue.edu.

REFERENCES

[1] Brian Z. Bentz, Brian J. Redman, Andres L. Sanchez, John D. van der Laan, Karl Westlake, and Jeremy B. Wright. Utilizing highly scattered light for intelligence through aerosols. *Sandia National Laboratories Report*, SAND2019-10870, OSTI ID 1763218, 2019.

[2] Jeremy B. Wright, David Scrymgeour, John D. van der Laan, Shanalyn A. Kemme, Karl Westlake, Jacob W. Segal, Brian J. Redman, and Andres L Sanchez. Polarimetry for extended persistence and range in fog for infrastructure protection. *Sandia National Laboratories Report*, SAND2018-14018, OSTI ID 1488332, 2018.

[3] Akira Ishimaru. *Wave Propagation and Scattering in Random Media*, volume 2. Academic New York, 1978.

[4] Ėleonora Petrovna Zege, Arkadiĭ Petrovich Ivanov, and Iosif Leĭbovich Katsev. *Image Transfer Through a Scattering Medium.* Springer Verlag, 1991.

[5] Christopher Dunsby and Paul M. W. French. Techniques for depth-resolved imaging through turbid media including coherence-gated imaging. *J. Phys. D: Appl. Phys.*, 36(14):R207–R227, 2003.

[6] Tobias Meinert, Olaf Tietz, Klaus J. Palme, and Alexander Rohrbach. Separation of ballistic and diffusive fluorescence photons in confocal light-sheet microscopy of arabidopsis roots. *Sci. Rep.*, 6(1):1–14, 2016.

[7] John D. van der Laan, Jeremy B. Wright, David A. Scrymgeour, Shanalyn A. Kemme, and Eustace L. Dereniak. Evolution of circular and linear polarization in scattering environments. *Opt. Express*, 23(25):31874–31888, 2015.

[8] John D. van der Laan, Jeremy B. Wright, Shanalyn A. Kemme, and David A. Scrymgeour. Superior signal persistence of circularly polarized light in polydisperse, real-world fog environments. *Appl. Opt.*, 57(19):5464–5473, 2018.

[9] David Huang, Eric A. Swanson, Charles P. Lin, Joel S. Schuman, William G. Stinson, Warren Chang, Michael R. Hee, Thomas Flotte, Kenton Gregory, Carmen A. Puliafito, and James G. Fujimoto. Optical coherence tomography. *Science*, 254(5035):1178–1181, 1991.

[10] Rachael Tobin, Abderrahim Halimi, Aongus McCarthy, Martin Laurenzis, Frank Christnacher, and Gerald S. Buller. Three-dimensional single-photon imaging through obscurants. *Opt. Express*, 27(4):4590–4611, 2019.

[11] Pierre Bouguer. *Essai d'optique, sur la gradation de la lumiere*. Claude Jombert, 1729.

[12] Johann Heinrich Lambert. *Photometria sive de mensura et gradibus luminis, colorum et umbrae*. sumptibus vidvae E. Klett, typis CP Detleffsen, 1760.

[13] August Beer. Bestimmung der absorption des rothen lichts in farbigen flussigkeiten. *Ann. Physik*, 162:78–88, 1852.

[14] Allard Mosk, Yaron Silberberg, Kevin Webb, and Changhuei Yang. Imaging, sensing, and communication through highly scattering complex media. Technical report, Defense Technical Information Center, 2015.

[15] Ori Katz, Pierre Heidmann, Mathias Fink, and Sylvain Gigan. Non-invasive single-shot imaging through scattering layers and around corners via speckle correlations. *Nat. Photonics*, 8(10):784–790, 2014.

[16] Qiaoen Luo, Jason A. Newman, and Kevin J. Webb. Motion-based coherent optical imaging in heavily scattering random media. *Opt. Lett.*, 44(11):2716–2719, 2019.

[17] Eitan Edrei and Giuliano Scarcelli. Optical imaging through dynamic turbid media using the fourier-domain shower-curtain effect. *Optica*, 3(1):71–74, 2016.

[18] Simon R. Arridge. Optical tomography in medical imaging. *Inverse Prob.*, 15:R41–R93, 1999.

[19] Jong Chul Ye, Kevin J. Webb, Charles A. Bouman, and Rick P. Millane. Optical diffusion tomography by iterative-coordinate-descent optimization in a Bayesian framework. *J. Opt. Soc. Am. A*, 16(10):2400–2412, 1999.

[20] Brian Z. Bentz, Dergan Lin, Justin A. Patel, and Kevin J. Webb. Multiresolution localization with temporal scanning for super-resolution diffuse optical imaging of fluorescence. *IEEE Trans. Image Process.*, 29:830–842, 2019.

[21] Brian Z. Bentz, Dergan Lin, and Kevin J. Webb. Superresolution diffuse optical imaging by localization of fluorescence. *Phys. Rev. Appl.*, 10(3):034021, 2018.

[22] Esther H. R. Tsai, Brian Z. Bentz, Venkatesh Chelvam, Vaibhav Gaind, Kevin J. Webb, and Philip S. Low. *In vivo* mouse fluorescence imaging for folate-targeted delivery and release kinetics. *Biomed. Opt. Express*, 5(8):2662–2678, 2014.

[23] Brian Z. Bentz, Anmol V. Chavan, Dergan Lin, Esther H. R. Tsai, and Kevin J. Webb. Fabrication and application of heterogeneous printed mouse phantoms for whole animal optical imaging. *Appl. Opt.*, 55(2):280–287, 2016.

[24] Ashley Lyons, Francesco Tonolini, Alessandro Boccolini, Audrey Repetti, Robert Henderson, Yves Wiaux, and Daniele Faccio. Computational time-of-flight diffuse optical tomography. *Nat. Photonics*, 13(8):575–579, 2019.

[25] Piero Bruscaglioni, Paolo Donelli, Andrea Ismaelli, and Giovanni Zaccanti. Monte Carlo calculations of the modulation transfer function of an optical system operating in a turbid medium. *Appl. Opt.*, 32(15):2813–2824, 1993.

[26] Joakim Jönsson and Edouard Berrocal. Multi-Scattering software: part I: online accelerated Monte Carlo simulation of light transport through scattering media. *Opt. Express*, 28(25):37612–37638, 2020.

[27] Luc R. Bissonnette. Imaging through fog and rain. *Opt. Eng.*, 31(5):1045–1053, 1992.

[28] Evgenii E. Gorodnichev and D. B. Rogozkin. Small-angle multiple scattering of light in a random medium. *Zh. Eksp. Teor. Fiz*, 107:209–235, 1995.

[29] Eleonora P. Zege and Ludmila I. Chaikovskaya. Approximate theory of linearly polarized light propagation through a scattering medium. *J. Quant. Spectrosc. Radiat. Transf.*, 66(5):413–435, 2000.

[30] Vladimir P. Budak and A. V. Kozelskii. Accuracy and applicability domain of the small angle approximation. *Atmos. Oceanic Opt.*, 18:32–37, 2005.

[31] Luc R. Bissonnette. Multiple scattering of narrow light beams in aerosols. *Appl. Phys. B*, 60(4):315–323, 1995.

[32] Thorsten Spott and Lars O. Svaasand. Collimated light sources in the diffusion approximation. *Appl. Opt.*, 39(34):6453–6465, 2000.

[33] Brian Z. Bentz, Brian J. Redman, John D. van der Laan, Karl Westlake, Andrew Glen, Andres L. Sanchez, and Jeremy B. Wright. Light transport with weak angular dependence in fog. *Opt. Express*, 29(9):13231–13245, 2021.

[34] Brian J. Redman, John D. van der Laan, Karl Westlake, Jacob W. Segal, Charles F. LaCasse, Andres L. Sanchez, and Jeremy B. Wright. Measuring resolution degradation of long-wavelength infrared imagery in fog. *Opt. Eng.*, 58(5):051806, 2019.

[35] James J. Duderstadt and Louis J. Hamilton. *Nuclear Reactor Analysis*. Wiley-Interscience, 1976.

[36] Richard C. Haskell, Lars O. Svaasand, Tsong-Tseh Tsay, Ti-Chen Feng, Matthew S. McAdams, and Bruce J. Tromberg. Boundary conditions for the diffusion equation in radiative transfer. *J. Opt. Soc. Am. A*, 11(10):2727–2741, 1994.

[37] Michael S. Patterson, Britton Chance, and Brian C. Wilson. Time resolved reflectance and transmittance for the noninvasive measurement of tissue optical properties. *Appl. Opt.*, 28(12):2331–2336, 1989.

[38] Brian Z. Bentz, Brian J. Redman, John D. van der Laan, Karl Westlake, Andrew Glen, Andres L. Sanchez, and Jeremy B. Wright. Towards computational imaging for intelligence in highly scattering aerosols. In *Situation Awareness in Degraded Environments 2020*, volume 11424 of *Proc. SPIE*, page 1142405, 2020.

[39] George I. Bell and Samuel Glasstone. Nuclear reactor theory. Technical report, US Atomic Energy Commission, Washington, DC (United States), 1970.

[40] Brian Z. Bentz, Christian A. Pattyn, John D. van der Laan, Brian J. Redman, Andrew Glen, Andres L. Sanchez, Karl Westlake, and Jeremy B. Wright. Incorporating the effects of objects in an approximate model of light transport in scattering media. *Opt. Lett.*, 47(8):2000–2003, 2022.

[41] Adam B. Milstein, Michael D. Kennedy, Philip S. Low, Charles A. Bouman, and Kevin J. Webb. Statistical approach for detection and localization of a fluorescing mouse tumor in intralipid. *Appl. Opt.*, 44(12):2300–2310, 2005.

[42] Guangzhi Cao, Vaibhav Gaind, Charles A. Bouman, and Kevin J. Webb. Localization of an absorbing inhomogeneity in a scattering medium in a statistical framework. *Opt. Lett.*, 32(20):3026–3028, 2007.

[43] Brian Z. Bentz, Alfonso Costas, Vaibhav Gaind, Jose M Garcia, and Kevin J. Webb. 3D printed optical phantoms and deep tissue imaging for in vivo applications including oral surgery. In *Design and Quality for Biomedical Technologies X*, volume 10056 of *Proc. SPIE*, page 1005607, 2017.

[44] Brian Z. Bentz, Timothy C. Wu, Vaibhav Gaind, and Kevin J. Webb. Diffuse optical localization of blood vessels and 3D printing for guiding oral surgery. *Appl. Opt.*, 56(23):6649–6654, 2017.

[45] Brian Z. Bentz, Sakkarapalayam M. Mahalingam, Daniel Ysselstein, Paola C. Montenegro, Jason R. Cannon, Jean-Christophe Rochet, Philip S. Low, and Kevin J. Webb. Localization of fluorescent targets in deep tissue with expanded beam illumination for studies of cancer and the brain. *IEEE Trans. Med. Imag.*, 39(7):2472–2481, 2020.

[46] Jing Yu, Chuangbai Xiao, and Dapeng Li. Physics-based fast single image fog removal. In *IEEE 10th International Conference on Signal Processing Proceedings*, pages 1048–1052. IEEE, 2010.

[47] Boyi Li, Wenqi Ren, Dengpan Fu, Dacheng Tao, Dan Feng, Wenjun Zeng, and Zhangyang Wang. Benchmarking single-image dehazing and beyond. *IEEE Trans. Image Process.*, 28(1):492–505, 2018.

[48] Brian Z. Bentz, John D. van der Laan, Andrew Glen, Christian A. Pattyn, Brian J. Redman, Andres L. Sanchez, Karl Westlake, Ryan L. Hastings, Kevin J. Webb, and Jeremy B. Wright. Detection and localization of objects hidden in fog. *Proc. SPIE*, 11759:1175906, 2021.

[49] David B. Lindell and Gordon Wetzstein. Three-dimensional imaging through scattering media based on confocal diffuse tomography. *Nat. Commun.*, 11(1):1–8, 2020.

[50] Daiki Kijima, Takahiro Kushida, Hiromu Kitajima, Kenichiro Tanaka, Hiroyuki Kubo, Takuya Funatomi, and Yasuhiro Mukaigawa. Time-of-flight imaging in fog using multiple time-gated exposures. *Opt. Express*, 29(5):6453–6467, 2021.

[51] Adam B. Milstein, Seungseok Oh, Kevin J. Webb, Charles A. Bouman, Quan Zhang, David A. Boas, and R. P. Millane. Fluorescence optical diffusion tomography. *Appl. Opt.*, 42(16):3081–3094, 2003.

[52] Quanyu Zhou, Zhenyue Chen, Justine Robin, Xosé-Luís Deán-Ben, and Daniel Razansky. Diffuse optical localization imaging for noninvasive deep brain microangiography in the NIR-II window. *Optica*, 8(6):796–803, 2021.

[53] Soren D. Konecky, Amaan Mazhar, David Cuccia, Anthony J. Durkin, John C. Schotland, and Bruce J. Tromberg. Quantitative optical tomography of sub-surface heterogeneities using spatially modulated structured light. *Opt. Express*, 17(17):14780–14790, 2009.

[54] Edouard Berrocal, Sven-Göran Pettersson, and Elias Kristensson. High-contrast imaging through scattering media using structured illumination and Fourier filtering. *Opt. Lett.*, 41(23):5612–5615, 2016.

[55] Martin Schweiger and Simon R. Arridge. The Toast++ software suite for forward and inverse modeling in optical tomography. *J. Biomed. Opt.*, 19(4):040801, 2014.

[56] Roland Stull. *Practical Meteorology*. University of British Columbia, 2020.

[57] J. A. Garland. Some fog droplet size distributions obtained by an impaction method. *Quart. J. R. Met. Soc.*, 97(414):483–494, 1971.

[58] Paul A. Pisano, Lynette C. Goodwin, and Michael A. Rossetti. US highway crashes in adverse road weather conditions. In *24th Conference on International Interactive Information and Processing Systems for Meteorology, Oceanography and Hydrology, New Orleans, LA*, 2008.

[59] Ismail Gultepe, Garry Pearson, J. A. Milbrandt, B. Hansen, S. Platnick, P. Taylor, M. Gordon, J. P. Oakley, and S. G. Cober. The fog remote sensing and modeling field project. *Bull. Am. Meteorol. Soc.*, 90(3):341–360, 2009.

[60] Jeremy B. Wright, John D. van der Laan, Andres L. Sanchez, Shanalyn A. Kemme, and David A. Scrymgeour. Optical characterization of the Sandia fog facility. In John (Jack) N. Sanders-Reed and Jarvis (Trey) J. Arthur III, editors, *Degraded Environments: Sensing, Processing, and Display 2017*, volume 10197, page 1019704. International Society for Optics and Photonics, SPIE, 2017.

[61] Jeremy B. Wright, John D. van der Laan, Karl Westlake, Brian Z. Bentz, Andres L. Sanchez, Andrew Glen, and Brian J. Redman. Characterizing fog at the sandia fog facility. In John N. Sanders-Reed and Jarvis J. Arthur, editors, *SPIE Defense and Commercial Sensing*, volume 11424 of *Proc. SPIE*. SPIE.

[62] Christian A. Pattyn, Jake Zenker, Elihu Deneke, Lekha Patel, Brian J. Redman, John D. van der Laan, Ryan L. Hastings, David W. Alexander, Kevin J. Webb, Andrew Glen, Andres L. Sanchez, Karl Westlake, Brian Z. Bentz, and Jeremy B. Wright. Development and characterization of a tabletop fog chamber at Sandia National Laboratories. In Mark S. Dennison Jr., David M. Krum, John N. Sanders-Reed, and Jarvis J. Arthur III, editors, *SPIE Defense and Commercial Sensing*, volume 12125 of *Proc. SPIE*, page 121250A. International Society for Optics and Photonics, SPIE, 2022.

[63] United States Environmental Protection Agency. Criteria air pollutants, 2022.

[64] Gabriel C. Birch, Bryana L. Woo, Andres L. Sanchez, and Haley Knapp. Image quality, meteorological optical range, and fog particulate number evaluation using the sandia national laboratories fog chamber. *Opt. Eng.*, 56(08), 2017.

[65] National Oceanic Administration and Atmospheric. Sea water, 2022.

[66] Flight Operations Support & Line Assistance, Group, and AWO Interdirectorate. Flight operations support & line assistance. Report, 2001.

[67] Nidhi Kalra and Susan M. Paddock. Driving to safety: How many miles of driving would it take to demonstrate autonomous vehicle reliability? *Transp. Res. Part A Policy and Pract.*, 94:182–193, 2016.

[68] Ismail Gultepe, G. Pearson, J. A. Milbrandt, B. Hansen, S. Platnick, P. Taylor, M. Gordon, J. P. Oakley, and S. G. Cober. The fog remote sensing and modeling field project. *Bull. Am. Meteorol. Soc.*, 90(3):341–360, 2009.

[69] Gary D. Gilbert. The effects of particle size on contrast improvement by polarization discrimination for underwater targets. *Appl. Opt.*, 9:421–8, 1970.

[70] Gary D. Gilbert and John C. Pernicka. Improvement of underwater visibility by reduction of backscatter with a circular polarization technique. *Appl. Opt.*, 6(4):741–746, 1967.

[71] Gary D. Gilbert and John C. Pernicka. Improvement Of Underwater Visibility By Reduction Of Backscatter With A Circular Polarization Technique. In *Underwater Photo Optics I*, volume 0007, pages 15 – 25. International Society for Optics and Photonics, SPIE, 1966.

[72] M. P Rowe, E. N Pugh, J. Scott Tyo, and N. Engheta. Polarization-difference imaging: a biologically inspired technique for observation through scattering media. *Opt. Lett.*, 20(6):608–610, 1995.

[73] J. Scott Tyo, M. P. Rowe, E. N. Pugh, and N. Engheta. Target detection in optically scattering media by polarization-difference imaging. *Appl. Opt.*, 35(11):1855–1870, 1996.

[74] David B. Chenault and J. Larry Pezzaniti. Polarization imaging through scattering media. *Proc. SPIE*, 4133:124–133, 2000.

[75] John G. Walker, Peter C. Y. Chang, and Keith I. Hopcraft. Visibility depth improvement in active polarization imaging in scattering media. *Appl. Opt.*, 39(27):4933–4941, 2000.

[76] Jiefei Han, Kecheng Yang, Min Xia, Liying Sun, Zao Cheng, Hao Liu, and Junwei Ye. Resolution enhancement in active underwater polarization imaging with modulation transfer function analysis. *Appl. Opt.*, 54(11):3294–3302, 2015.

[77] Yi Wei, Pingli Han, Fei Liu, and Xiaopeng Shao. Enhancement of underwater vision by fully exploiting the polarization information from the stokes vector. *Opt. Express*, 29(14):22275–22287, 2021.

[78] William C. Mickols, Carlos Bustamante, Marcos F. Maestre, Ignacio Tinoco Jr., and Stephen H. Embury. Differential polarization microscopy: A new imaging technique. *Nat. Biotechnol.*, 3:711, 1985.

[79] Mark P. Silverman and Wayne Strange. Object delineation within turbid media by backscattering of phase-modulated light. *Opt. Commun.*, 144:7–11, 1997.

[80] Stavros Demos, Harry Radousky, and Robert Alfano. Deep subsurface imaging in tissues using spectral and polarization filtering. *Opt. Express*, 7:23, 2000.

[81] Steven L Jacques, Jessica C Ramella-Roman, and Ken Lee. Imaging skin pathology with polarized light. *J. Biomed. Opt.*, 7:329–40, 2002.

[82] Steven L. Jacques, Ravikant Samatham, Scott Isenhath, and Ken Lee. Polarized light camera to guide surgical excision of skin cancers. *Proc. SPIE*, 6842:68420I, 2008.

[83] Jessica C. Ramella-Roman, Ken Lee, Scott A. Prahl, and Steven L. Jacques. Design, testing, and clinical studies of a handheld polarized light camera. *J. Biomed. Opt.*, 9:1305–10, 2004.

[84] Hanrong Shao, Yonghong He, Wei Li, and Hui Ma. Polarization-degree imaging contrast in turbid media: a quantitative study. *Appl. Opt*, 45:4491–6, 2006.

[85] Zeng Nan, Jiang Xiaoyu, Gao Qiang, He Yonghong, and Ma Hui. Linear polarization difference imaging and its potential applications. *Appl. Opt.*, 48:6734–9, 2009.

[86] Nirmalya Ghosh and I Alex Vitkin. Tissue polarimetry: concepts, challenges, applications, and outlook. *J Biomed Opt.*, 16:110801, 2011.

[87] Lu Liu, Binkang Li, Shaohua Yang, Mingan Guo, Ming Yan, Tongding Luo, Gang Li, and Shuai Gao. Polarization-difference imaging of objects in smoke environment. In Lin Li, Kevin P. Thompson, and Ligong Zheng, editors, *AOPC 2015: Optical Design and Manufacturing Technologies*, volume 9676, page 96760J. International Society for Optics and Photonics, SPIE, 2015.

[88] Julien Fade, Swapnesh Panigrahi, Anthony Carré, Ludovic Frein, Cyril Hamel, Fabien Bretenaker, Hema Ramachandran, and Mehdi Alouini. Long-range polarimetric imaging through fog. *Appl. Opt.*, 53:3854–65, 2014.

[89] Maria Ballesta-Garcia, Sara Peña-Gutiérrez, Aina Val-Martí, and Santiago Royo. Polarimetric imaging vs. conventional imaging: Evaluation of image contrast in fog. *Atmosphere*, 12(7):813, 2021.

[90] Sara Peña-Gutiérrez, Maria Ballesta-Garcia, Pablo García-Gómez, and Santiago Royo. Quantitative demonstration of the superiority of circularly polarized light in fog environments. *Opt. Lett.*, 47(2):242–245, 2022.

[91] Li Zhang, Zhongjun Yin, Kaichun Zhao, and Han Tian. Lane detection in dense fog using a polarimetric dehazing method. *Appl. Opt.*, 59(19):5702–5707, 2020.

[92] John D. van der Laan, David A. Scrymgeour, Shanlyn A. Kemme, and Eustace L. Dereniak. Detection range enhancement using circularly polarized light in scattering environments for infrared wavelengths. *Appl. Opt.*, 54(9):2266–2274, 2015.

[93] John D. van der Laan, Jeremy B. Wright, David A. Scrymgeour, Shanalyn A. Kemme, and Eustace L. Dereniak. Evolution of circular and linear polarization in scattering environments. *Opt. Express*, 23:31874–31888, 2015.

[94] John D. van der Laan, Jeremy B. Wright, David A. Scrymgeour, Shanalyn A. Kemme, and Eustace L. Dereniak. Effects of collection geometry variations on linear and circular polarization persistence in both isotropic-scattering and forward-scattering environments. *Appl. Opt.*, 55(32):9042–9048, 2016.

[95] John D. van der Laan, Jeremy B. Wright, Shanalyn A. Kemme, and David A. Scrymgeour. Superior signal persistence of circularly polarized light in polydisperse, real-world fog environments. *Appl. Opt.*, 57(19):5464–5473, 2018.

[96] E. J. Nunes-Pereira, H. Peixoto, J. Teixeira, and J. Santos. Polarization-coded material classification in automotive lidar aiming at safer autonomous driving implementations. *Appl. Opt.*, 59(8):2530–2540, 2020.

[97] Dennis H. Goldstein. *Polarized Light, Third Edition*. CRC Press, 2010.

[98] Brian Z. Bentz, Brian J. Redman, John D. van der Laan, Karl Westlake, Andrew Glen, Andres L. Sanchez, and Jeremy B. Wright. Light transport with weak angular dependence in fog. *Opt. Express*, 29(9):13231–13245, 2021.

[99] Brian J. Redman, John D. van der Laan, Karl Westlake, Jacob W. Segal, Charles F. LaCasse, Andres L. Sanchez, and Jeremy B. Wright. Measuring resolution degradation of long-wavelength infrared imagery in fog. *Opt. Eng.*, 58(5):051806, 2019.

[100] Ardeshir Goshtasby. Image registration by local approximation methods. *Image Vis. Comput.*, 6(4):255–261, 1988.

[101] Albert A. Michelson. *Studies in Optics*. University of Chicago Press, Chicago, Illinois, 1927.

[102] Glenn D. Boreman and Sidney Yang. Modulation transfer function measurement using three- and four-bar targets. *Appl. Opt.*, 34(34):8050–8052, 1995.

[103] Zhongping Lee and Shaoling Shang. Visibility: How applicable is the century-old koschmieder model? *J. Atmos. Sci.*, 73(11):4573–4581, 2016.

[104] Kurt Beier and Hans Gemperlein. Simulation of infrared detection range at fog conditions for enhanced vision systems in civil aviation. *Aerospace Sci. Technol.*, 8(1):63–71, 2004.

[105] World Meteorological Organization (WMO). *Guide to Meteorological Instruments and Methods of Observation*. Publications Board WMO, Geneva, Switzerland, 2008.

[106] Craig F. Bohren and Donald R. Huffman. *Absorption and Scattering of Light by Small Particles*. John Wiley & Sons, Inc., New York, New York, USA, 1983.

[107] Kevin J. Webb and Qiaoen Luo. Theory of speckle intensity correlations over object position in a heavily scattering random medium. *Phys. Rev. A.*, 101(6):063827, 2020.

[108] Qiaoen Luo and Kevin J. Webb. Parametrization of speckle intensity correlations over object position for coherent sensing and imaging in heavily scattering random media. *Phys. Rev. Res.*, 2(3):033148, 2020.

[109] Jason A. Newman, Qiaoen Luo, and Kevin J. Webb. Imaging hidden objects with spatial speckle intensity correlations over object position. *Phys. Rev. Lett.*, 116(7):73902, feb 2016.

[110] Joseph W. Goodman. *Speckle Phenomena in Optics: Theory and Applications*. Roberts and Company Publishers, 2007.

[111] J. D. McKinney, M. A. Webster, Kevin J. Webb, and A. M. Weiner. Characterization and imaging in optically scattering media by use of laser speckle and a variable-coherence source. *Opt. Lett.*, 25(1):4–6, January 2000.

[112] M. A. Webster, T. D. Gerke, K. J. Webb, and A. M. Weiner. Spectral and temporal speckle field measurements of a random medium. *Opt. Lett.*, 29(13):1491–1493, July 2004.

[113] Isaac Freund, Michael Rosenbluh, and Shechao Feng. Memory effects in propagation of optical waves through disordered media. *Phys. Rev. Lett.*, 61(20):2328–2331, 1988.

[114] J. A. Newman and K. J. Webb. Fourier magnitude of the field incident on a random scattering medium from spatial speckle intensity correlations. *Opt. Lett.*, 37(7):1136–1138, Apr 2012.

[115] Qiaoen Luo, Justin A. Patel, and Kevin J. Webb. Super-resolution sensing with a randomly scattering analyzer. *Phys. Rev. Res.*, 3(4):L042045, 2021.

[116] Kevin J. Webb and Qiaoen Luo. Theory of speckle intensity correlations over object position in a heavily scattering random medium. *Phys. Rev. A*, 101(6):063827, 2020.

[117] Jason A. Newman, Qiaoen Luo, and Kevin J. Webb. Imaging hidden objects with spatial speckle intensity correlations over object position. *Phys. Rev. Lett.*, 116(7):073902, 2016.

[118] Ryan L. Hastings, David W. Alexander, and Kevin J. Webb. Far-subwavelength spatial resolution using speckle correlations. 2022. Submitted.

[119] Brian Z. Bentz, Dergan Lin, Justin A. Patel, and Kevin J. Webb. Multiresolution localization with temporal scanning for super-resolution diffuse optical imaging of fluorescence. *IEEE Trans. Image Process.*, 29:830–842, 2019.

[120] Ryan L. Hastings, Brian Z. Bentz, Dergan Lin, and Kevin J. Webb. Simultaneous imaging and localization in a heavily scattering random medium with speckle data from a moving object. In *Conference on Lasers and Electro-Optics*, page STu2F.2. Optica Publishing Group, 2021.

[121] Jason A. Newman and Kevin J. Webb. Imaging optical fields through heavily scattering media. *Phys. Rev. Lett.*, 113:263903, Dec 2014.

[122] Zhenyu Wang, Kevin J. Webb, and Andrew M. Weiner. Coherent incident field information through thick random scattering media from speckle correlations over source position. *Appl. Opt.*, 49(30):5899–5905, Oct. 2010.

[123] Zhenyu Wang, Andrew M. Weiner, and Kevin J. Webb. Interferometry from a scattering medium. *Opt. Lett.*, 32(14):2013–2015, Jul 2007.

[124] Kevin J. Webb, Yulu Chen, and Trevor A. Smith. Object motion with structured optical illumination as a basis for far-subwavelength resolution. *Phys. Rev. Appl.*, 6(2):024020, 2016.

[125] Mark A. Richards. Iterative noncoherent angular superresolution (radar). In *Proceedings of the 1988 IEEE National Radar Conference*, pages 100–105, Ann Arbor, MI, USA, 1988. IEEE.

[126] Jinchen Guan, Yulin Huang, Jianyu Yang, Wenchao Li, and Junjie Wu. Improving angular resolution based on maximum a posteriori criterion for scanning radar. In *2012 IEEE Radar Conference*, pages 0451–0454, May 2012. ISSN: 2375-5318.

DISTRIBUTION

Hardcopy—Internal

Number of Copies	Name	Org.	Mailstop
1	L. Martin, LDRD Office	1910	0359
1	Legal Intellectual Property	11500	0161

Email—Internal (encrypt for OUO)

Name	Org.	Sandia Email Address
Technical Library	1911	sanddocs@sandia.gov

Sandia
National
Laboratories